



The
University
Of
Sheffield.

MOCVD Growth of Novel GaN Materials on Silicon Substrates

By:
Xiang Yu

Supervisor: Professor Tao Wang

A thesis submitted for the degree of
Doctor of Philosophy (Ph.D.)

The University of Sheffield
Faculty of Engineering
Department of Electronic and Electrical Engineering

Submission Date

JANUARY, 2017

Abstract

This work studies growth of two major kinds of semi-polar GaN including (11-22) and (20-21) GaN on novel designed silicon (Si) substrates and growth of GaN nanowires (NWs) on planar Si substrates both by means of metal organic chemical vapour deposition (MOCVD).

In principle, semi-polar GaN cannot be achieved by MOCVD growth on any planar Si substrates. In order to obtain semi-polar GaN on Si, patterned Si substrates are required. Two different kinds of simple but cost-effective patterning approaches have been developed to fabricate (113) Si substrates with either inverted-pyramid or stripe patterns, where a combination of a standard photolithography technique, dry etching and anisotropic wet etching has been employed. As a result of these cost-effective approaches, patterned Si substrates with both good uniformity and high reproducibility have been achieved.

By the growth on the (113) Si substrates with inverted-pyramid patterns, semi-polar (11-22) GaN with high quality has been achieved. Taking the major advantages of such a specially designed patterning, both melt-back etching and surface cracks, which are the two major issues for the growth of GaN-on-silicon, have been successfully eliminated. The (11-22) orientated GaN has been confirmed and characterised by detailed X-ray diffraction (XRD) measurements, and detailed microstructural investigation has been performed by transmission electron microscopy (TEM) measurements. The TEM measurements show a significant reduction in crystal defects like dislocations and basal plane stacking fault (BSFs). As a result, good optical properties have been obtained for the (11-22) GaN, confirmed by photoluminescence (PL) measurements.

Stripe-patterned Si substrates have been fabricated in order to allow to achieve semi-polar (20-21) GaN films through the growth on either both sidewalls or single sidewalls of the Si stripes. In the case of the growth on the single sidewall of the Si stripes, a single crystal (20-21) GaN has been obtained. In the case of the growth on both sidewalls of the Si stripes, the growth of (20-21) GaN coalescences and then leads to a surface with an 'M' shape. The melt-back etching has been resolved by introducing a number of extra gaps to truncate the Si stripe patterns, allowing the NH_3 as a precursor for group V to cover all the exposed silicon surface so

that melt-back etching can be effectively suppressed. The ‘M’ shaped GaN self-forms a good cavity which could be further used for the growth of a laser structure, one of the greatest challenges for the fabrication of semi-polar III-nitride based laser diodes as a result of extreme difficulties in cleaving semi-polar GaN. The microstructural investigation and optical properties of the (20-21) GaN have been carried out by detailed XRD, TEM and PL measurements. Finally, growth of InGaN multiple quantum well (MQWs) structures has been attempted on the (20-21) semi-polar GaN in order to validate the excellent crystal quality of the (20-21) semi-polar GaN. Temperature-dependent and excitation-power dependent PL measurements on the InGaN MQWs have been performed, demonstrating high internal quantum efficiency and effectively suppressed quantum confine stark effect, compared to their c-plane counterparts.

It is well-known that the MOCVD growth of GaN NWs on planar Si substrates without any patterning feature or without any pre-deposited metal catalyst is a great challenge, which is completely different from MBE growth, where Ga metal instead of Ga precursor (metal organic source) is used and the growth is performed under high vacuum. In order to address this challenge, a new approach for the growth of GaN NWs on planar (111) Si substrates has been developed, where the key point is to employ Trimethylaluminum (TMA) pre-flowing. It has been found that the formation of Al-Si alloyed nanodots by the TMA pre-flowing is critical to the initialisation of GaN NW growth. The influence of the growth conditions used on the NW morphology has been systematically investigated. By optimizing the growth conditions, straight and cylindrical GaN NWs have been obtained. Based on XRD and TEM measurements, the NWs demonstrate high crystal quality with a low density of defects, leading to superior optical properties confirmed by PL measurements.

Acknowledgements

It has been a great journey for me to study in the UK's top research group for III-Nitrides technologies through the past five years. During this period of time, I gained loads of great support and help from so many people, who I would like to express my sincere gratitude to here.

First and foremost, I would like to thank my supervisor Prof. Tao Wang, who was also my undergraduate personal tutor during the second and third year. He offered me massive help during my undergraduate study and guided me to the academic research world by offering me this PhD opportunity. During my PhD study, he provided me with a favourable research environment, as well as great support, trust and encouragement. More importantly, he spent a lot of time on helping me to build a better view of science and learn critical thinking for problem identification and solving. With the longstanding contact, I have been profoundly influenced by his enthusiasm and hard work on research. In addition, I have established the personalities of hard work, carefulness and never giving up, which not only benefit my PhD study but also will significantly impact my whole life.

Also, I would like specially thank Dr. Yipin Gong and Dr. Kun Xing. They trained me how to utilise the most experimental facilities and kindly share their valuable PhD study experience and scientific knowledge with me. Dr. Yipin Gong trained me the MOCVD operation and a number of measurement equipment. I usually discussed with him about different research problems and got many very good advices. He also did a lot of maintenance work for MOCVD and PL system, keeping equipment with good state. Dr. Kun King is an expert in device fabrication field. He introduced me many fabrication knowledge and skills. He also helped me to fabricate lots of Si substrates with very high quality. Dr. Yipin Gong and Dr. Kun Xing are also my good friends privately. We had really good time together for the past five years and they were always on my side to help me finishing my PhD study.

I would like to acknowledge Dr. Jie Bai for the professional TEM measurement and Si substrate fabrication. In addition, she is a highly knowledgeable scientist, who taught me to analyse TEM and PL measurement results. Dr. Jie Bai also helped me to do the HF treatment

and offer me a lot of help on writing skills.

I would like to thank Dr. Yaonan Hou for the Si substrate fabrication and HF treatment. I discussed with him frequently, I gained loads of support at fabrication and PL characterisation field with his wide range of knowledge. He also helped me to improve writing skills.

Many thanks go to Mr. Shuoheng Shen, who work with me closely on the project since last year. He fabricated many excellent Si substrates and did a lot of operation and measurement work, saving me a large amount of time. We also discussed quite often to share opinions and new ideas.

I would like to thank all my colleagues, we worked together and supported with each other as a team. Dr. Rick Smith established many optical measurement systems. He patiently and systematically trained other colleagues to use them. Dr. Rick Smith and Dr. Modestos Athanasious did a lot of maintenance work on many optical measurement systems, and they also share their rich experience and knowledge with me, especially for optical characterisation filed. Mr. Benbo trained me to do the confocal and micro-PL measurements, we worked interactively for one year, and he did a lot of operation, maintenance and measurement work. Mr. Yun Zhang trained me to do the TEM preparation and helped me to do the TEM and time-resolved PL measurements. Mr. Qingping Zeng and Mr. Ling Jiu helped me to fabricate a number of Si substrates. Mr. Zhi Li and Mr. Xuanming Zhao did a lot of operation, measurement and maintenance work, saving me a lot of time. Dr. Bing Liu and Dr. Liancheng Wang helped me to understand many theories and gave me many good advises. Dr. Liancheng Wang also helped me to improve my writing skills. I want to thank Mr. Zohaib Ahmed Syed, Mr. Nicolas Poyiatzis and Mr. Suneal Ghataora, who broadened me horizons with their specialized knowledge in different research area. I also would like to thank Prof. Robert Martin and Dr. Jochen Bruckbauer from the University of Strathclyde Glasgow, who helped me to perform a lot of CL measurement.

I am greatly indebted to all technicians in the EPSRC cleanroom for their hard work. Mr. Paul Haines always helped us to maintain and fix the MOCVD system, he take care of almost all equipment in the EPSRC cleanroom, as well as our optical measurement systems. I would like to thank Mr. Dave Morris, Mr. Jon Milner, Mr. Richard Frith, Mr. Ken Kennedy and Mr. Rob Airey, for maintaining the EPSRC cleanroom within excellent status. I would like to thank

Mr. Gordon Askwith for great maintaining the cleanroom clean and tidy.

I would like to thank Prof. John David. He was my first year undergraduate personal tutor, who helped me to start my abroad study favourably. And as our head of department at that time, he offered me kindly support to start my PhD study. I would also like to thank Ms. Hilary Levesley for solving all my administrative issues during my PhD study.

Finally, I would like to give my deepest thanks to my family, not only for supporting my abroad study for 8 years, but also for everything they have done in my life. Without their support and encouragement, I would not get to this point through all the tough difficulties.

This is a long journey, and finally I am reaching the final line, I valued everyone and everything happened to me until now, this journey will be one of the most precious jewellery in my whole life memory.

List of Publications

Journal Publications

1. Y. N. Hou, Z.A. Syed, R.M. Smith, M. Athanasiou, Y. Gong, **X. Yu**, J. Bai, and T. Wang, *Enhanced water splitting with silver decorated GaN photoelectrode*, J. Phys. D: Appl. Phys. **49**, 265601 (2016).
2. Y. Zhang, J. Bai, Y.N. Hou, R.M. Smith, **X. Yu**, Y. Gong, and T. Wang, *Defect reduction in overgrown semi-polar (11-22) GaN on a regularly arrayed micro-rod array template*, AIP Advances **6**, 025201 (2016).
3. **X. Yu**, Y.N. Hou, S.H. Shen, J. Bai, Y. Gong, Y. Zhang, and T. Wang, *Semi-polar (11-22) GaN grown on patterned (113) Si substrate*, Phys. Status Solidi C **13**, 190 (2016).
4. J. Bai, **X. Yu**, Y. Gong, Y.N. Hou, Y. Zhang, and T. Wang, *Growth and characterization of semi-polar (11-22) GaN on patterned (113) Si substrates*, Semicond. Sci. Technol. **30**, 065012 (2015).
5. B. Xu, **X. Yu**, Y. Gong, K. Xing, J. Bai, and T. Wang, *Study of high-quality (11-22) semi-polar GaN grown on nanorod templates*, Phys. Status Solidi B **252**, 1079 (2015).
6. Y. Gong, K. Xing, B. Xu, **X. Yu**, Z. Li, J. Bai, and T. Wang, *High efficiency green-yellow emission from InGaN/GaN quantum well structures grown on overgrown semi-polar (11-22) GaN on regularly arrayed micro-rod templates*, ECS Trans. **66**, 151 (2015).
7. B. Liu, R. Smith, M. Athanasiou, **X. Yu**, J. Bai, and T. Wang, *Temporally and spatially resolved photoluminescence investigation of (112-2) semi-polar InGaN/GaN multiple quantum wells grown on nanorod templates*, Appl. Phys. Lett. **105**, 261103 (2014).
8. K. Xing, Y. Gong, **X. Yu**, J. Bai, and T. Wang, *Improved crystal quality of (11-22) semi-polar GaN grown on a nano-rod template*, Jpn. J. Appl. Phys. **52**, 08JC03 (2013).
9. J. Bai, Y. Gong, K. Xing, **X. Yu**, and T. Wang, *Efficient reduction of defects in (11-20) non-polar and (11-22) semi-polar GaN grown on nano-rod template*, Appl. Phys. Lett. **102**, 101906 (2013).

Conference Publications

1. **X. Yu**, S.H. Shen, Y.N. Hou, Y. Gong, A. Hazari, P. Bhattacharya, and T. Wang, *Catalyst-free GaN nanowires grown on (111) Si substrate by MOVPE*, Semiconductor and Integrated Optoelectronics (SIOE) Conference, Cardiff, UK (2016).
2. **X. Yu**, S.H. Shen, Y.N. Hou, Y. Gong, A. Hazari, P. Bhattacharya, and T. Wang, *GaN nanowires grown on (111) Si substrate by MOVPE*, UK Nitrides Consortium (UKNC) Winter Conference, University of Cambridge, UK (2016).
3. **X. Yu**, J. Bai, S.H. Shen, Y. Gong, Y.N. Hou, Y. Zhang, and T. Wang, *Semi-polar (11-22) GaN grown on patterned (113) Si substrates*, International Conference on Nitride Semiconductors (ICNS), Beijing, China (2015).
4. **X. Yu**, J. Bai, Y. Gong, Y.N. Hou, Y. Zhang, and T. Wang, *Semi-polar (11-22) GaN grown on patterned (311) Si substrates*, UK Nitrides Consortium (UKNC) Winter Conference, University of Nottingham, UK (2015).
5. Y. Gong, K. Xing, B. Xu, **X. Yu**, Q. Zeng, R.M. Smith, J. Bai, and T. Wang, *High efficiency long-wavelength emission from InGaN/GaN MQWs on semi-polar (11-22) GaN overgrown on micro-rod templates*, UK Nitrides Consortium (UKNC) Winter Conference, University of Nottingham, UK (2015).
6. B. Xu, **X. Yu**, Y. Gong, K. Xing, B. Liu, J. Bai, and T. Wang, *Study of high-quality (11-22) semi-polar GaN grown on nanorod templates*, International Workshop on Nitride Semiconductors (IWN), Wroclaw, Poland (2014).
7. **X. Yu**, B. Xu, Y. Gong, K. Xing, and T. Wang, *Study of GaN layer grown on GaN nano-rod templates on (111) Si substrates*, UK Semiconductors, Sheffield Hallam University, UK (2013).
8. K. Xing, Y. Gong, **X. Yu**, J. Bai, and T. Wang, *Improved crystal quality of (11-22) semi-polar GaN grown on nano-rod templates*, International Workshop on Nitride Semiconductors (IWN), Sapporo, Japan (2012).
9. K. Xing, Y. Gong, **X. Yu**, J. Bai, and T. Wang, *Study of overgrowth of non-polar GaN grown on a-plane GaN nano-rod template*, UK Nitrides Consortium (UKNC) Winter Conference, University of Bath, UK (2012).

Contents

Abstract	I
Acknowledgements	III
List of Publications	VI
Chapter 1 Introduction	1
1.1 History of III-nitrides Research	1
1.2 Current Challenges.....	3
1.3 Motivation and Aim	8
1.4 Thesis Organization	9
References.....	10
Chapter 2 Background	12
2.1 Semiconductors.....	12
2.1.1 Introduction.....	12
2.1.2 Direct and Indirect Band Gaps.....	13
2.1.3 Doping.....	13
2.1.4 Crystal Defects.....	14
2.2 III-nitride semiconductors.....	16
2.2.1 Material Properties.....	16
2.2.2 Crystal Structure	17
2.2.3 Non-polar and Semi-polar.....	19
2.2.4 GaN Nanowires.....	21
2.3 Epitaxial Growth of GaN on Si.....	21
2.3.1 Introduction.....	21
2.3.2 Issues of GaN Growth on Si	23
2.3.3 Development of GaN Growth on Si.....	24
References.....	30
Chapter 3 Equipment	34
3.1 Metal-Organic Chemical Vapour Deposition.....	34
3.1.1 Main Configuration.....	34

3.1.2 Gas Purifiers.....	35
3.1.3 MO Source Bubbler	36
3.1.4 Gas Delivery System.....	38
3.1.5 Reactor System	38
3.1.6 Exhaust System.....	40
3.2 Nomarski Optical Microscope	40
3.3 Scanning Electron Microscope	42
3.4 Transmission Electron Microscope.....	43
3.5 High Resolution X-ray Diffraction	43
3.6 Photoluminescence	45
References.....	47
Chapter 4 Fabrication of Patterned Si Substrates	48
4.1 Introduction.....	48
4.2 Selection of Si Substrate Orientation.....	49
4.3 (113) Si Substrates with Inverted-pyramid patterns	50
4.3.1 Methodology.....	50
4.3.2 Formation of Inverted-pyramid Patterns.....	51
4.3.3 Selective Deposition of SiO ₂ Mask.....	54
4.4 (113) Si Substrates with Stripe Patterns.....	56
4.4.1 Methodology	56
4.4.2 Formation of Stripe Patterns	57
4.5 Summary.....	60
References.....	61
Chapter 5 Semi-polar (11-22) GaN Grown on Inverted-pyramid Patterned (113) Si.....	62
5.1 Growth of GaN on Inverted-pyramid Patterned Si.....	62
5.2 Structural and Optical Characterizations	66
5.3 Mechanism of Defect Reduction in GaN.....	72
5.4 Conclusion	76
References.....	78
Chapter 6 Semi-polar (20-21) GaN Grown on Stripe Patterned (113) Si.....	80
6.1 Growth of GaN on Stripe Patterned Si	80

6.2 Structural and Optical Characterization.....	85
6.3 InGaN MQWs grown on (20-21) GaN	92
6.4 Conclusion	97
References.....	99
Chapter 7 Self-induced GaN Nanowires Grown on (111) Si Substrates	101
7.1 Nanowire Growth with TMA Pre-flowing.....	101
7.2 Effects of GaN Growth Condition	103
7.3 Structural and Optical Characterization.....	107
7.4 Conclusion	111
References.....	113
Chapter 8 Summary and Future Work	114
8.1 Summary.....	114
8.2 Future Work	115
Abbreviations	116

Chapter 1

Introduction

III-nitride semiconductors (AlN, GaN, InN and their alloys) all exhibit direct band structures and their bandgaps across their entire alloy composition cover a wide spectral range from deep ultraviolet to infrared. III-nitrides also have excellent chemical stability. As a result, III-nitride semiconductors nowadays have drawn extensive research interests and have become the favourite semiconductors for the optoelectronics industry, especially for the fabrication of visible and short wavelength emitters. III-nitride based light-emitting diodes (LEDs) and laser diodes (LDs) have been successfully fabricated for display backlighting, traffic lights, projectors, general illumination and etc. Compared with incandescent and fluorescent bulbs, the III-nitride based solid state lighting exhibits higher efficiency, longer life-time, smaller size, improved physical robustness and faster switching. The last two decades have seen impressive advancements in optoelectronic devices, leading to the award of the Noble Prize in Physics in 2014. However, there are still a number of obstacles to further improve the performance of III-nitride based optoelectronics, such as efficiency droop, green and yellow gap, crystal quality and high cost due to expensive techniques required.

1.1 History of III-nitrides Research

Since the first report of high-brightness blue LED based on III-nitrides demonstrated in 1993 [1], there have been significant progress on developing III-nitride based LEDs and LDs in the visible spectral region, although there still exists a long-term outstanding issue in developing longer wavelength such as green and yellow emitters. Today, III-nitride based blue LEDs, the key component for the fabrication of solid state lighting sources, have been commercialised. They have been generally used in residential and decorative lighting, backlighting, etc. However, there still exist a number of challenges, such as low efficiency in the green/yellow spectral region which is the so-called ‘green/yellow gap’, efficiency droop, high cost compared with incandescent lamps, etc. Therefore, it is necessary to further devote major effort to developing new growth approaches in order to address these challenges.

The research on III-nitride semiconductors started in 1932 when GaN was first synthesized by means of reacting gallium metal with ammonia (NH_3) at $900 \sim 1000 \text{ }^\circ\text{C}$ [2]. By this method, only needle shape GaN with a few micrometers thickness was obtained. In 1969 a hydride vapour phase epitaxy (HVPE) technology was utilised for the deposition of GaN on sapphire substrates [3], where ammonia was used as a precursor for group V and GaCl was used to supply a gallium source by flowing HCl over hot liquid gallium metal. Two years later, metal organic chemical vapour deposition (MOCVD) was employed for GaN and AlN growth [4]. Trimethylgallium (TMG) and trimethylaluminium (TMA) are used as the precursors for group III in order to supply gallium and aluminium sources, respectively. Although single crystalline and transparent GaN has been achieved on sapphire, both the crystal quality and surface morphology were rather poor due to the lack of either native substrates or technology breakthroughs for large lattice-mismatched growth. Consequently, the research on GaN did not draw much attention at that time.

Isamu Akasaki, Hiroshi Amano et al. performed a large amount of pioneering work in the early 1980's, and invented a so-called two step growth approach in 1986 [5], one of the most important growth breakthroughs in the field of GaN. As a result, optically flat GaN with significantly improved crystal quality has been achieved by MOCVD growth, namely, a thin low temperature (LT) AlN buffer layer is initially deposited on sapphire before any high temperature GaN growth. Later on in 1991, Shuji Nakamura further employed a thin LT GaN buffer instead of the AlN buffer [6], achieving GaN with equally good crystal quality. The great invention based on the thin LT GaN or AlN buffer has become a standard method for the growth of GaN on sapphire, which has been widely employed by industry.

Another major obstacle to achieve GaN-based optoelectronic devices was p-type GaN. Magnesium (Mg) was used as the p-type dopant [7]. However, any as-grown Mg-doped GaN exhibits either highly resistive or n-typed. Until in 1989, the first p-type GaN was realised by treating as-grown Mg-doped GaN under a low energy electron beam irradiation [8]. In 1992 Shuji Nakamura invented another simple method to realize p-type GaN by thermally annealing Mg-doped GaN under nitrogen ambient [9]. The mechanisms for the p-type activation process is to break the Mg-H complex formed during the MOCVD growth of Mg-doped GaN under H_2 or NH_3 ambient and then free holes can be obtained [10, 11].

Based on these achievements, the first high brightness blue InGaN double heterostructure (DH) LED was demonstrated in 1993 [1, 12]. In 1995, the first white LED by integrating InGaN blue LED with yellow phosphor was reported [13].

1.2 Current Challenges

The last two decades have seen tremendous progress in developing III-nitride semiconductors and devices, leading to the award of the Noble Prize in Physics in 2014. However, it is worth highlighting that the major achievements are still limited to blue emitters, in particular blue LEDs on c-plane sapphire grown along the polar direction. There still exist a number of challenges in both science and technologies, in particular fabricating longer wavelength (green and yellow) emitters.

Quantum Confined Stark Effect

For the fabrication of visible or near UV emitters, InGaN/GaN based MQW structures are used as an active region, where the MQWs are under biaxial strain as a result of the lattice mismatch between InGaN as a quantum well and GaN as a barrier. As a consequence, strong piezoelectric polarization induced electrical fields are generated along the c-direction (i.e., the growth direction) [14, 15]. Simultaneously, spontaneous polarisation induced electrical fields will be also produced along the c-direction [15, 16]. As a result of the built-in electrical fields, the wave functions of electrons and holes are spatially separated by the electric fields as shown in Figure 1.1, leading to a reduction in the overlap of electron and hole wave-functions and thus lowering quantum efficiency. It will also generate a red shift in emission wavelength [17]. This phenomenon is so-called quantum confined stark effect (QCSE).

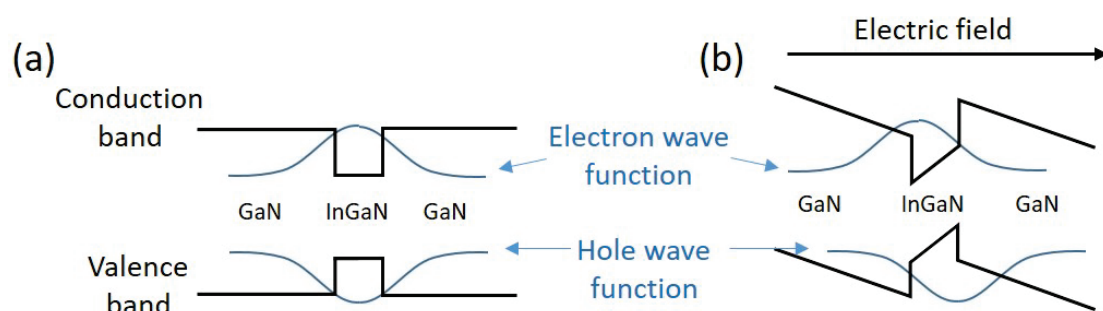


Figure 1.1: Band structure of QW (a) without and (b) with built-in electric fields.

Efficiency Droop

Generally speaking, the internal quantum efficiency (IQE) of III-nitride based LEDs have a peak value at low current densities ($< 10 \text{ A/cm}^2$), namely, the IQE initially increases with increasing injection current density to a peak value, and then decreases gradually with further increasing injection current density. This phenomenon is called ‘efficiency droop’. This issue has commonly been observed in III-nitride based LEDs with a wide spectral region from UV to visible as shown in Figure 1.2, indicating that it become more severe with increasing wavelength. So far, the fundamental mechanisms for efficiency droop remain under debate. A number of models have been proposed, such as electron leakage [19], density-activated defect recombination [20], and Auger recombination [21]. The electron leakage means that injected electrons overflow across InGaN/GaN MQWs as an active region to p-type GaN without producing any radiative recombination. By increasing current injection density, more energetic electrons leak from the MQWs, leading to a reduced optical efficiency. The density-activated defect recombination is due to the delocalisation of carriers. At low injection current densities, the carrier density is low, and thus electrons and holes are confined in a local in-plane potential minimum due to the fluctuation of indium composition. The localised carriers are supposed to be kept from dislocations as non-recombination centres, leading to high radiative efficiency. However, with increasing injection current density, the local in-plane potential minima are gradually filled and the carriers start to escape to defect areas which serve as non-radiative recombination centres causing non-radiative recombination and thus reduced efficiency. The Auger recombination is a kind of non-radiative recombination process, where the energy released by an electron-hole recombination is absorbed by another electron in the conduction band, rather than emitting a photon. The second electron is excited to a higher energy level, then drops back to the conduction band and loses the absorbed energy as thermal energy. As a result, Auger recombination consumes the electron-hole pairs without generating any photons and thus reduces the efficiency of LEDs.

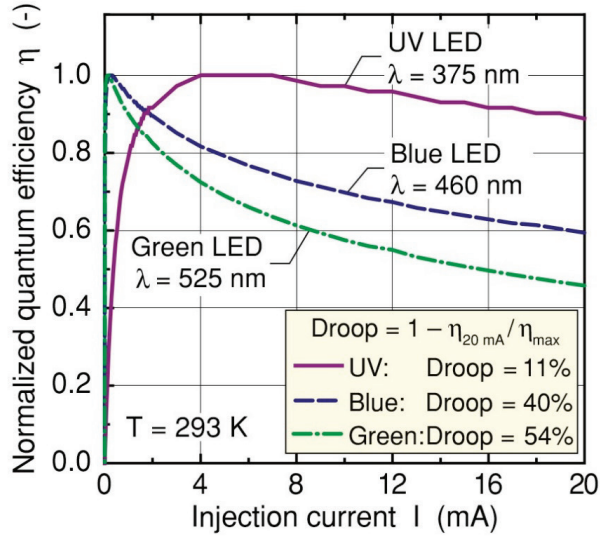


Figure 1.2: Quantum efficiency of UV/blue/green LEDs as a function of injection current [18].

Green and Yellow Gap

GaN and its ternary alloys AlGaIn/InGaIn exhibit direct band structures with wide bandgaps, covering a wide spectra region from UV to infrared. As mentioned above, great success has been achieved on developing InGaIn/GaN based blue LEDs. However, the optical efficiency of InGaIn/GaN LEDs decreases significantly with increasing emission wavelength, while the optical efficiency from other III-V semiconductors such as AlInGaP decreases with reducing emission wavelength, as illustrated in Figure 1.3, demonstrating the lowest quantum efficiency in the green and yellow spectral region. This has been referred to as the ‘green/yellow gap’. For III-nitride semiconductors, in order to achieve longer emission wavelength (> 500 nm), high In content is required. But high In content can only be achieved at the expense of employing low growth temperatures which generally cause a reduction in crystal quality. Moreover, high In content generates enhanced strain in InGaIn/GaN MQWs, leading to even stronger QCSE. As a result, the quantum efficiency of InGaIn/GaN based LEDs is quite low when the emission wavelength is longer than the blue spectral region.

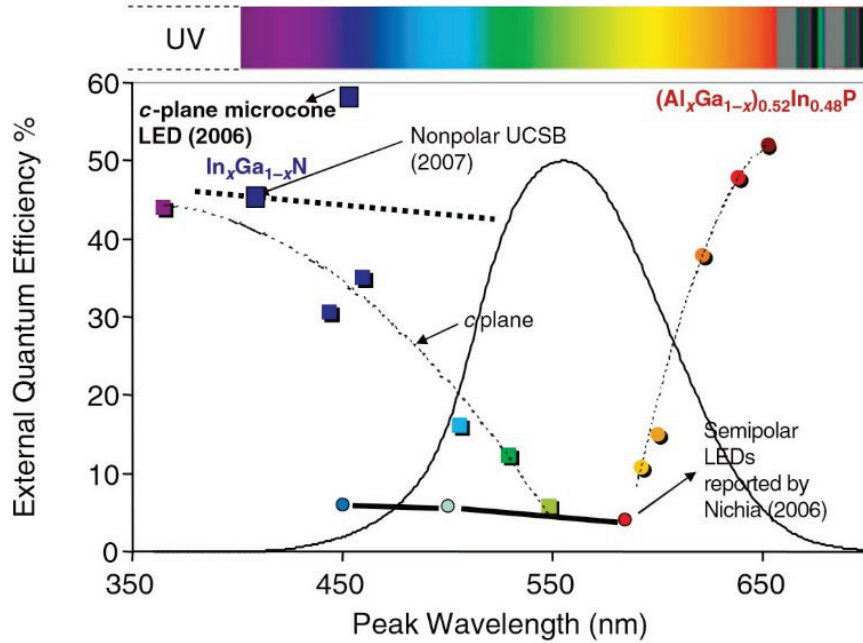


Figure 1.3: External quantum efficiency of LEDs as a function of the emission wavelength in recent years [22].

Epitaxial Substrate

The growth of bulk GaN crystal from a solution is unrealistic due to its thermodynamic instability and low N solubility in liquid Ga [23]. Therefore, chemical reaction deposition methods (MOVPE and HVPE) are utilised for GaN growth on foreign substrates. Generally, silicon carbide (SiC), sapphire and silicon (Si) are used as substrates for GaN epitaxial growth. Compared with sapphire and Si, the lattice mismatch between SiC and GaN is the smallest (3.5%) and SiC further exhibits the highest thermal conductivity (4.9 W/cmK) [24]. However, the high price of SiC substrate makes it less competitive for mass production. Sapphire substrates are much cheaper than SiC, and larger size sapphire (>2 inch) is available, making sapphire very popular for GaN growth. But the large lattice mismatch (16%) and the very low thermal conductivity (0.41 W/cmK) also make a great challenge for GaN growth on sapphire [24]. For Si as a substrate, although it has the largest lattice mismatch (17%) and the largest thermal expansion coefficient mismatch (115%) [24], due to a low cost and a large substrate size available, it has received increasing attention very recently, in particular for growth of III-nitride based electronics devices. Due to the extremely mature Si technology, the

unification of III-nitrides with Si would be an ideal solution for the integration of semiconductor-based electronics and photonics.

On the other hand, although bulk GaN crystal growth from solution is impossible, free-standing GaN substrate is still available. Typically, a very thick GaN layer of more than 300- μm is first grown on a foreign substrate, typically on sapphire by HVPE, and is subsequently removed by a so-called laser-off technique. Therefore, current free-standing GaN substrates are very expensive. It is worth highlighting that non-polar or semi-polar free standing GaN substrates are even more expensive than their c-plane (i.e., polar GaN) counterpart. It is well-known that the crystal quality of either semi-polar GaN or non-polar GaN directly grown on sapphire by any current growth techniques is far lower compared with their c-plane counterpart. Consequently, free-standing semi-polar GaN or non-polar GaN substrates are achieved currently only by growth of a very thick c-plane GaN layer with a thickness of around one centimetre and then cleaving along semi-polar/non-polar orientations. Therefore, the typical size of either semi-polar or non-polar free-standing GaN substrates is limited to $1\times 1\text{ cm}^2$, and their prices are extremely expensive. These make semi-polar or non-polar free-standing GaN substrates less attractive for commercial mass production. Figure 1.4 shows photos of a typical c-plane GaN wafer with a diameter of 2 inch grown on sapphire and a typical free-standing non-polar GaN substrate with a size of $1\times 1\text{ cm}^2$. Please note that the free-standing non-polar GaN substrate is not transparent, thus implying a high density of point defects which generate deep levels within the bandgap of GaN.

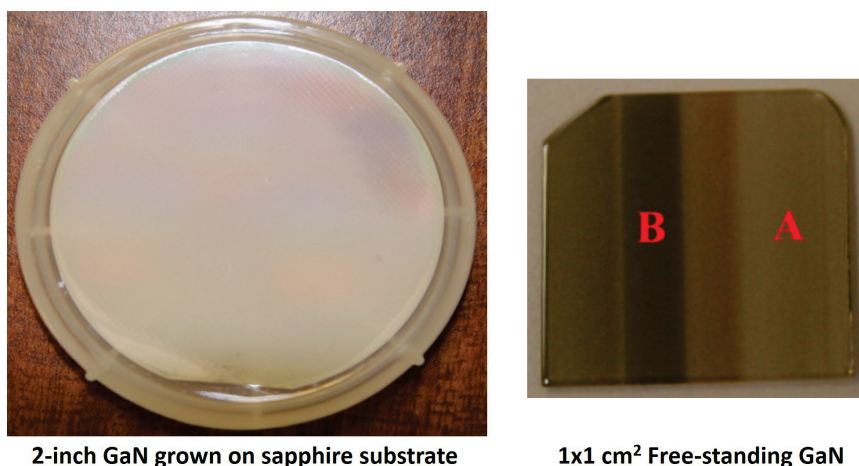


Figure 1.4: Photos of 2-inch non-polar GaN on sapphire substrate and 1x1 cm² free-standing non-polar GaN.

1.3 Motivation and Aim

Due to a number of great issues discussed in section 1.2, the optical performance of III-nitride based optoelectronics, in particular longer wavelength emitters, still remains challenging.

The maturity of Si technology allows us to have more choices to further develop III-nitride optoelectronics with better performance, in particular, Si substrates provide a great potential for the integration of semiconductor-based electronics and photonics [25, 26].

On the other hand, in order to improve optoelectronic performance, the QCSE and efficiency droop has to be suppressed. One of the most promising ways, which can address the great challenges, is to grow InGaN-based emitters along a non/semi-polar orientation, where the QCSE can be eliminated or significantly reduced, and as a result the optical efficiency can be improved [27, 28]. Comparing with any non-polar GaN or c-plane GaN, semi-polar GaN with specific orientations (i.e., semi-polar GaN with a large inclination angle with respect to the c-plane) demonstrates a number of other advantages, such as greatly enhanced In incorporation in InGaN growth or high indium content InGaN with enhanced indium homogeneity, which is good for LDs [29-31].

Another way is to grow GaN nanowire (NW) structures, where InGaN MQWs can be grown on the sidewall of NWs in order to form a core-shell structure, or can be grown on the top of NWs to form a disk-in-wire structure. For the former, as the sidewall of GaN NW is either non-polar or semipolar orientated, the QCSE is absent or significantly reduced [32]. For the latter, the strain in MQW can be fully or partially relaxed, leading to a significant reduction in QCSE [33, 34]. Moreover, a very high crystal quality of bottom-up grown GaN NWs can be achieved by an elastic strain relaxation [35]. However, both semi-polar GaN and GaN NWs grown on Si substrates are currently far from satisfactory. There are still many problems such as: crystal quality, surface morphology, uniformity, etc (shown in Chapter 2.3.3). Therefore, the aim of the research in this thesis is to grow semi-polar GaN and GaN NWs on Si substrates with good crystal quality and uniformity.

1.4 Thesis Organization

The thesis consists of 8 chapters:

Chapter 1 gives a brief introduction and a history of III-nitride semiconductor development. The current challenges of III-nitrides and motivation of this project are also discussed.

Chapter 2 presents a general background of semiconductors, in particular III-nitride semiconductors. The epitaxial growth of GaN on Si substrates is introduced in detail.

Chapter 3 introduces all equipment used in this study. Firstly, the growth mechanism and the main configuration of a MOCVD is introduced. Then a number of characterization techniques are described, including Nomarski optical microscope, scanning electron microscopy (SEM), transmission electron microscope (TEM), high resolution X-ray diffraction (XRD) and photoluminescence (PL) systems.

Chapter 4 studies two kinds of Si substrate patterning techniques developed, which will be used for the growth of semi-polar GaN. The technique details including Si substrate orientation selection, photolithography, dry etching and wet etching are presented.

Chapter 5 studies the semi-polar (11-22) GaN growth on the patterned Si substrates obtained in Chapter 4. The mechanism of a defect reduction is investigated by TEM.

Chapter 6 investigates the semi-polar (20-21) GaN growth on the patterned Si substrates obtained in Chapter 4. Two kinds of GaN growth processes have been developed. InGaN MQW structures have been grown on the top of the semi-polar (20-21) GaN in order to validate the high quality of the achieved (20-21) semi-polar GaN.

Chapter 7 studies the self-induced growth of GaN NWs on (111) Si substrates. The structure and optical characterization of GaN NWs are discussed.

Chapter 8 provides a summary and outlook.

References

1. S. Nakamura, M. Senoh, and T. Mukai, *Jpn. J. Appl. Phys.* **32**, L8 (1993)
2. W. C. Johnson, J. B. Parsons, and M. C. Crew, *J. Phys. Chem.* **36**, 2561 (1932)
3. H. P. Maruska, and J. J. Tietjen, *Appl. Phys. Lett.* **15**, 327 (1969)
4. H. M. Manasevit, F. M. Erdmann, and W. I. Simpson, *J. Electrochem. Soc.* **118**, 1864 (1971)
5. H. Amano, N. Sawaki, I. Akasaki, and Y. Toyoda, *Appl. Phys. Lett.* **48**, 353 (1986)
6. S. Nakamura, *Jpn. J. Appl. Phys.* **30**, L1705 (1991)
7. H. P. Maruska, D. A. Stevenson, and J. I. Pankove, *Appl. Phys. Lett.* **22**, 303 (1973)
8. H. Amano, M. Kito, K. Hiramatsu, and I. Akasaki, *Jpn. J. Appl. Phys.* **28**, L2112 (1989)
9. S. Nakamura, N. Iwasa, M. Senoh, and T. Mukai, *Jpn. J. Appl. Phys.* **31**, 1258 (1992)
10. J. A. Vanvechten, J. D. Zook, R. D. Horning, and B. Goldenberg, *Jpn. J. Appl. Phys.* **31**, 3662 (1992)
11. J. Neugebauer, and C. G. Van De Walle, *Phys. Rev. Lett.* **75**, 4452 (1995)
12. S. Nakamura, T. Mukai, and M. Senoh, *Appl. Phys. Lett.* **64**, 1687 (1994)
13. K. Bando, Y. Noguchi, K. Sakano, and Y. Shimizu, *Tech. Digest. Phosphor Res. Soc.*, 264th Meeting (1996)
14. T. Takeuchi, S. Sota, M. Katsuragawa, M. Komori, H. Takeuchi, H. Amano, and I. Akasaki, *Jpn. J. Appl. Phys.* **36**, L382 (1997)
15. F. Bernardini, V. Fiorentini, and D. Vanderbilt, *Phys. Rev. B* **56**, R10024 (1997)
16. V. Fiorentini, F. Bernardini, F. Della Sala, A. Di Carlo, and P. Lugli, *Phys. Rev. B* **60**, 8849 (1999)
17. D. A. B. Miller, D. S. Chemla, T. C. Damen, A. C. Gossard, W. Wiegmann, T. H. Wood, C. A. Burrus, *Phys. Rev. Lett.* **53**, 2173 (1984)
18. J. Cho, E. F. Schubert, and J. K. Kim, *Laser Photonics Rev.* **7**, 408 (2013)
19. K. J. Vampola, M. Iza, S. Keller, S. P. DenBaars, and S. Nakamura, *Appl. Phys. Lett.* **94**, 061116 (2009)
20. J. Hader, J. V. Moloney, and S. W. Koch, *Appl. Phys. Lett.* **96**, 221106 (2010)
21. J. Iveland, L. Martinelli, J. Peretti, J. S. Speck, and C. Weisbuch, *Phys. Rev. Lett.* **110**, 177406 (2013)

22. S. Nakamura, *Mrs Bulletin* **34**, 101 (2009)
23. H. Amano, *Rev. Mod. Phys.* **87**, 1133 (2015)
24. D. Zhu, D. J. Wallis, C. J. Humphreys, *Rep. Prog. Phys.* **76**, 106501 (2013)
25. T. K. Li, M. Mastro, and A. Dadgar, III-V Compound Semiconductors: Integration with Silicon-Based Microelectronics (CRC Press, Parkway, NW, 2010)
26. S. L. Selvaraj, A. Watanabe, and T. Egawa, *Appl. Phys. Lett.* **98**, 252105 (2011)
27. P. Waltereit, O. Brandt, A. Trampert, H. T. Grahn, J. Menniger, M. Ramsteiner, M. Reiche, and K. H. Ploog, *Nature* **406**, 865 (2000)
28. T. Takeuchi, H. Amano, and I. Akasaki, *Jpn. J. Appl. Phys.* **39**, 413 (2000)
29. P. De Mierry, T. Guehne, M. Nemoz, S. Chenot, E. Beraudo, and G. Nataf, *Jpn. J. Appl. Phys.* **48**, 031002 (2009).
30. S. Yamamoto, Y. Zhao, C. C. Pan, R. B. Chung, K. Fujito, J. Sonoda, S. P. Denbaars, and S. Nakamura, *Appl. Phys. Express* **3**, 122102 (2010)
31. T. Wang, *Semicond. Sci. Technol.* **31**, 093003 (2016)
32. R. Koester, J. S. Hwang, D. Salomon, X. Chen, C. Bougerol, J. P. Barnes, D. L. S. Dang, L. Rigutti, A. de Luna Bugallo, G. Jacopin, and M. Tchernycheva, *Nano lett.* **11**, 4839 (2011)
33. W. Guo, M. Zhang, A. Banerjee, and P. Bhattacharya, *Nano lett.* **10**, 3355 (2010)
34. H. W. Lin, Y. J. Lu, H. Y. Chen, H. M. Lee, and S. Gwo, *Appl. Phys. Lett.* **97**, 073101 (2010)
35. J. Ristić, E. Calleja, M. A. Sánchez-García, J. M. Ulloa, J. Sánchez-Páramo, J. M. Calleja, U. Jahn, A. Trampert, and K. H. Ploog, *Phys. Rev. B* **68**, 125305 (2003)

Chapter 2

Background

2.1 Semiconductors

2.1.1 Introduction

In an isolated atom, electrons occupy a set of discrete energy levels. When atoms form solid, these discrete electron energy levels overlap and spread out to form bands. Basically, a single crystal consists of a valence band and a conduction band. The valence band is the highest electron occupied energy band at absolute zero temperature, while the conduction band is the lowest unoccupied energy band [1]. Between them forms a forbidden gap which is the so-called 'bandgap'. The bandgap is defined as an energy split between the maximal potential in a valence band and the minimal potential in a conduction band.

For insulators, the band gap is so large that the thermal energy at room temperature or an external electrical field cannot energize and excite electrons from a valence band to a conduction band. Thus electrons are tightly bound in the state of a valence band and cannot freely move, leading to a negligible electrical conductivity. For conductors, the valence band and conduction band overlap, leading a fraction of electrons to freely move. Therefore, conductors have a high electrical conductivity. Semiconductors are defined as that their electrical conductivity is between conductors and insulators. In other words, the band gap of a semiconductor is between insulators and conductors. Consequently, at room temperature, a number of electrons can be thermally excited from its valence band to its conduction band, leaving the same number of empty states behind in the valence band, which are called holes. The holes generated behave like free positive charged carriers. The number of free electrons and holes thermally generated depends on the bandgap of the semiconductor, namely, the smaller the bandgap, the higher the number. As a result, the free electrons and holes form electrical conductivity which is higher than insulators but lower than conductors. Of course, doping which will be discussed later can also effectively tune the number of free electrons and

holes, thus significantly changing the electrical conductivity of a semiconductor.

2.1.2 Direct and Indirect Band Gaps

A semiconductor can be classified as either a direct or an indirect band gap semiconductor in terms of its band diagram [1]. As shown in Figure 2.1, for a semiconductor with a direct band structure, the conduction band minimum and the valence band maximum have the same momentum. In contrast, for an indirect band gap semiconductor, the conduction band minimum has a different momentum from the valence band maximum. For a direct band gap semiconductor, the electrons in the conduction band as a result of optical or electrical pumping return to the valence band and then recombine with the holes, releasing photons. This recombination process does not involve any third party, and thus the recombination lifetime is generally fast. However, for an indirect band gap semiconductor, the recombination of the electron-hole pairs generated due to optical or electrical pumping needs an extra momentum in order to conserve momentum, leading to a long recombination lifetime and thus a low optical efficiency. Therefore, direct band gap semiconductors are commonly utilised for the fabrication of emitters such as LEDs and LDs.

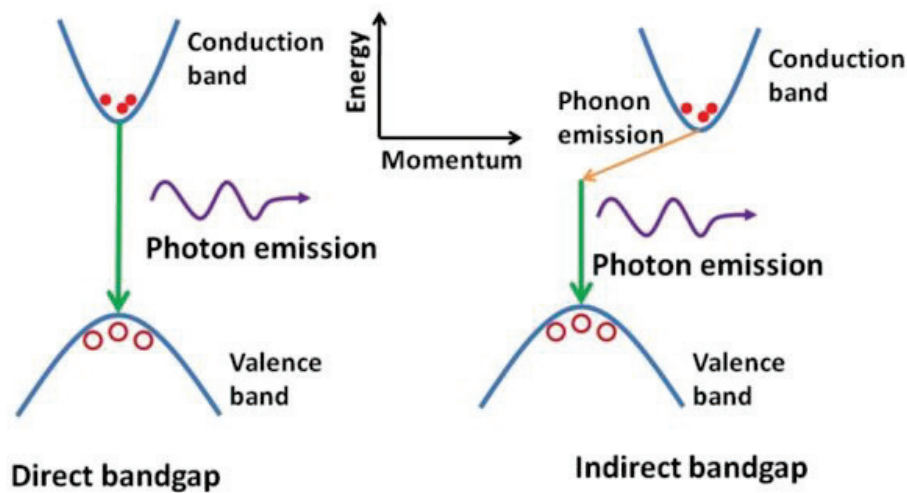


Figure 2.1: Band structures of direct and indirect band gap semiconductors [2].

2.1.3 Doping

In an intrinsic semiconductor, the number of thermally excited free electrons and holes is

limited and the electrical conductivity is thus low, of course depending on its band gap. By deliberately introducing a small amount of impurities during semiconductor growth, the electric conductivity can be increased remarkably. This kind of semiconductor is referred to a doped semiconductor. Two types of dopant elements are used in order to form either n-type or p-type semiconductors. A n-type semiconductor is formed by doping foreign atoms that replace one of the elements forming the semiconductor, generating additional valence electrons which are weakly bound and thus can be thermally excited to the conduction band at room temperature. Therefore, an n-type semiconductor is rich with free electrons at room temperature. On the other hand, the p-type semiconductor is dominated by free holes. For III-nitrides, Si and Mg are the typical dopants for the formation of n-type and p-type III-nitrides, respectively.

2.1.4 Crystal Defects

III-nitride semiconductors have a periodic crystal structure and the positions of atoms are determined by their unit cell lattice parameters. However, when GaN is grown on lattice-mismatched substrates such as sapphire and Si, crystal defects are generated, defined as the imperfection of a crystalline solid with irregular atomic arrangement in three main categories, zero-dimensional defects (point defects), one-dimensional defects (dislocations) and two-dimensional defects (stacking faults).

A point defect happens where an atom is missing or resides on a non-lattice site, or a foreign atom substitutes a bulk atom. Depending on whether it is due to an impurity, the point defect can be classified as either an intrinsic or an extrinsic point defect, as shown in Figure 2.2. A vacancy is an empty lattice site where an atom is missing. A self-interstitial atom is a bulk atom crowded into the void of a lattice site. A substitutional foreign atom is an impurity atom substituting the bulk atom. Finally, the interstitial foreign atom has the same situation as a self-interstitial atom.

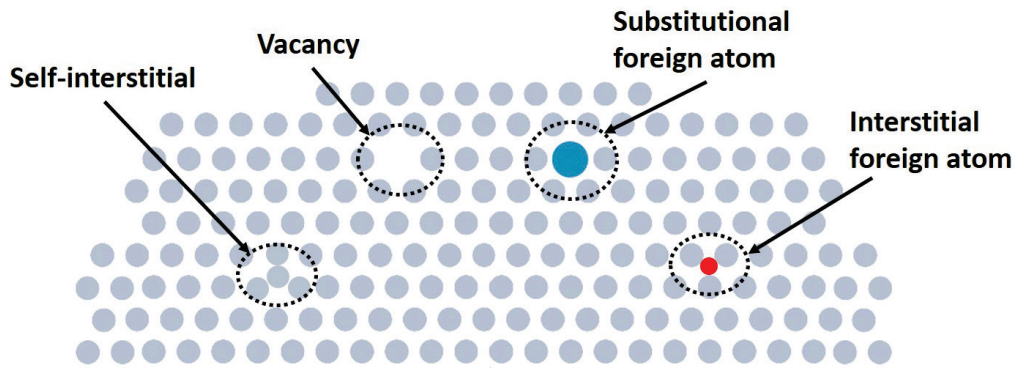


Figure 2.2: Schematic illustration of four types of point defects [3].

A dislocation is a line defect, where a line of atoms is misaligned. Basically, there are two main types of dislocations: edge and screw dislocations. However, many dislocations have mixed characters of the two types, named as a mixed dislocation. As shown in Figures 2.3 (a) and (c), without any crystal defects, rectangles can be drawn along a crystal lattice, which are highlighted in green colour. When an edge dislocation is introduced (Figure 2.3(b)), which is caused by an extra plane of atoms inserted into the crystal lattice, the rectangular unit cell is deformed. This additional vector (red colour) from the rectangular unit cell is described by Burgers vector, which is parallel to the rectangle plane. The Burgers vector can be used to represent the magnitude and direction of a dislocation. On the other hand, a screw dislocation is caused by a slipping between two planes of atoms (Figure 2.3(d)), and the Burgers vector is perpendicular to the rectangle plane (highlighted in red colour).

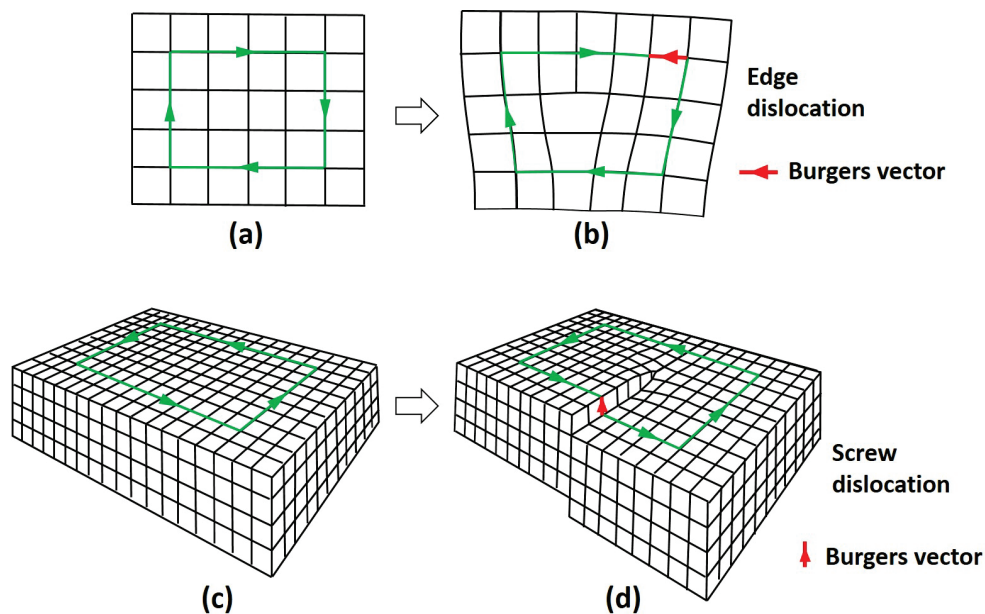


Figure 2.3: Schematic diagram of edge and screw dislocations [4].

A stacking fault (SF) is formed as a result of a mistake of a planar stacking sequence. For c-plane GaN growth on sapphire, SFs are limited to be close to the interface between GaN and the sapphire substrate along the [0001] direction, which are also described as basal plane stacking faults (BSFs). For semi-polar and the non-polar GaN growth on sapphire, as the growth direction is not along the [0001] direction, BSFs can extend to a surface and thus degrade the optical property of optoelectronic devices. For either semi-polar or non-polar GaN grown on sapphire substrates, the density of BSFs is normally $\sim 10^5 \text{cm}^{-1}$ if there is not any extra growth technique used [5].

2.2 III-nitride semiconductors

2.2.1 Material Properties

Comparing with other III-V semiconductors, the major advantage of III-nitrides used for the fabrication of optoelectronics is due to their wide bandgaps in addition to their direct band structures. As shown in Figure 2.4, the bandgaps of III-nitrides can cover a wide range of spectrum from deep UV, through the whole visible, to infrared. Therefore, III-nitrides are very suitable for the fabrication of visible and short wavelength emitters, such as solid state lighting for general illumination and UV emitters.

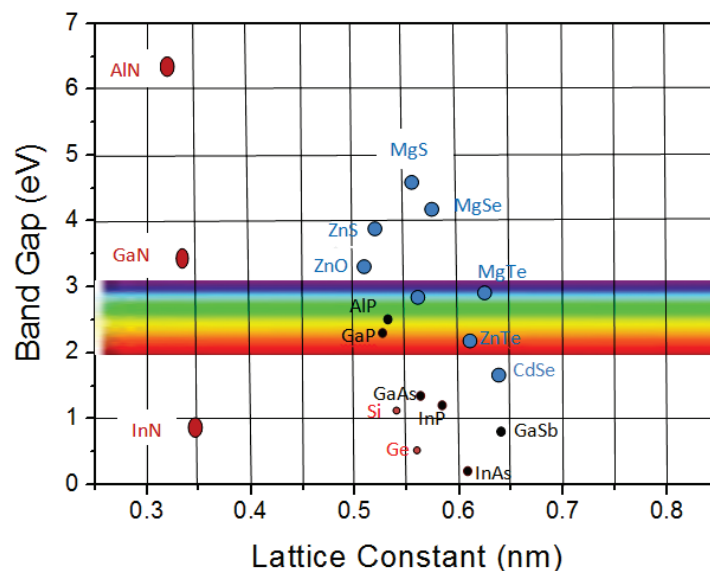


Figure 2.4: Band gap and emission wavelength of semiconductors against their lattice constant [6].

The basic electrical and chemical properties of GaN are illustrated in Table 2.1. The electron mobility characterises how easily electrons move through a crystal lattice, when an electric field is applied. It is limited by electron scattering, which can be caused by impurities, crystal defects, phonons and etc. Since GaN epilayers grown by different growth techniques have different crystal qualities, the electron mobilities in different GaN epilayers are also different. The highest reported room temperature electron mobility of bulk GaN is $1245 \text{ cm}^2\text{V}^{-1}\text{s}^{-1}$ [8], where a free-standing GaN is grown by HVPE. For GaN grown by MOCVD, the highest reported room temperature electron mobility is $1005 \text{ cm}^2\text{V}^{-1}\text{s}^{-1}$ [9]. In comparison with other III-V semiconductors, GaN shows a larger band gap, a higher breakdown voltage and a higher thermal conductivity. Moreover, GaN has excellent thermal and chemical stabilities, in particular high inert properties in either an alkaline or an acidic solution. A KOH solution can only etch GaN through attacking crystal defects.

Semiconductor	Band gap [eV]	Electron mobility [$\text{cm}^2/(\text{V}\cdot\text{s})$]	Breakdown Field [KV/cm]	Thermal conductivity [W/($\text{cm}\cdot^\circ\text{C}$)]	Melting point [$^\circ\text{C}$]
GaN	3.39	1245	≥ 5000	1.3	2500
GaAs	1.42	8500	400	0.46	1238
InP	1.34	4000	500	0.68	1062

Table 2.1: Material properties of group III-V semiconductors at room temperature [7-8].

2.2.2 Crystal Structure

III-nitride semiconductors have three different crystal structures, namely, wurtzite, zinblende [10] and rocksalt [11]. The wurtzite III-nitride semiconductors are thermodynamically stable, and are the most common crystal structure. As shown in Figure 2.5, in a wurtzite crystal structure, each nitrogen atom is connected to four group III atoms, forming a hexagonal close packed configuration. This hexagonal unit cell is characterized by an in-plane lattice parameter labelled as a and an out-of-plane lattice parameter denoted as c . The lattice parameters of wurtzite GaN, AlN and InN are illustrated in Table 2.2.

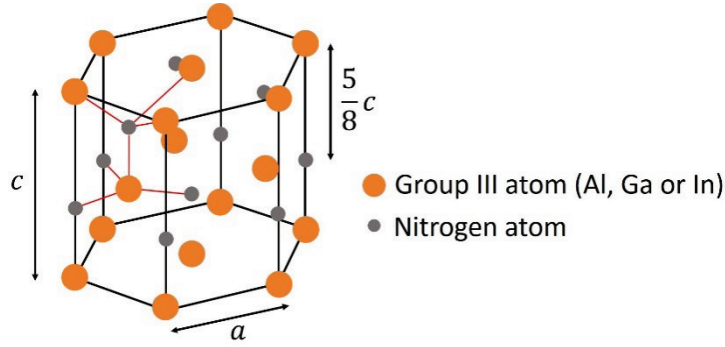


Figure 2.5: Schematics of an III-nitride wurtzite crystal structure

III-nitride semiconductors	in-plane lattice parameter a (Å)	out-of-plane lattice parameter c (Å)
GaN	3.190	5.189
AlN	3.110	4.980
InN	3.540	5.706

Table 2.2: The lattice parameters of wurtzite GaN, AlN and InN [12].

The crystal planes and directions of wurtzite III-nitride semiconductors can be described by Bravais miller indices. As shown in Figure 2.6, (a_1, a_2, a_3, c) and $[a_1, a_2, a_3, c]$ are used to describe a crystal plane and a crystal direction, respectively. The first three digits are the reciprocals of fractional intercepts between the crystal plane and the three in-plane axes, while the last digit is the reciprocal of fractional intercept between the crystal plane and out-of-plane axis. Since $a_3 = -(a_1 + a_2)$, miller indices can also be abbreviated to (a_1, a_2, c) .

As a wurtzite crystal structure is non-centrosymmetric, namely, lacks inversion symmetry, there exist two polar orientations defined as $[0001]$ and $[000-1]$ direction respectively. The $[0001]$ direction is denoted as a Ga-face plane, where the surface is terminated with Ga atoms, whereas the $[000-1]$ direction crystal plane is terminated with N atoms. Most of the c-plane GaN grown on sapphire substrates is Ga-terminated (i.e, Ga-face), since an N-face GaN epilayer usually has a rough surface with a large number of hexagonal hillocks. On the other hand, due to the lack of inversion symmetry of wurtzite crystal structure, III-nitride materials inherently exhibit spontaneous polarization. In addition, when InGaN/GaN MQWs are grown, piezoelectric polarization fields are also induced as a result of a biaxial strain, which is caused by the lattice mismatch between InGaN and GaN. As a result of the spontaneous and

piezoelectric polarizations, build-in electric fields are induced across the MQW structure, which generate the QCSE.

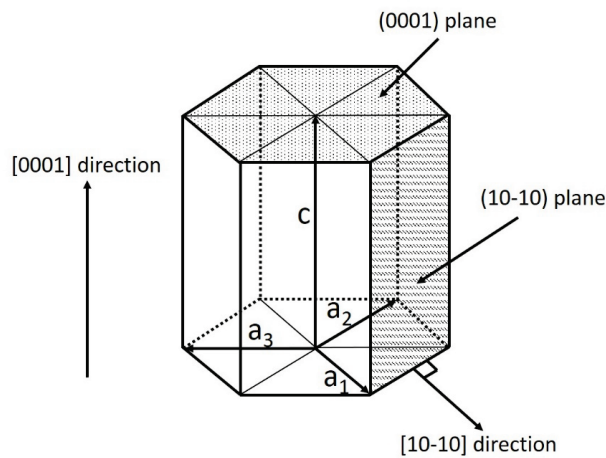


Figure 2.6: Bravais miller indices of wurtzite crystal structure.

2.2.3 Non-polar and Semi-polar

Recently, non-polar or semi-polar GaN has attracted much attention since they can eliminate or effectively reduce the QCSE, leading to an improved internal quantum efficiency (IQE) of InGaN MQWs. Some common growth planes of non-polar and semi-polar GaN are listed in Figure 2.7, and their corresponding crystal orientations are illustrated in Table 2.3 [13, 14].

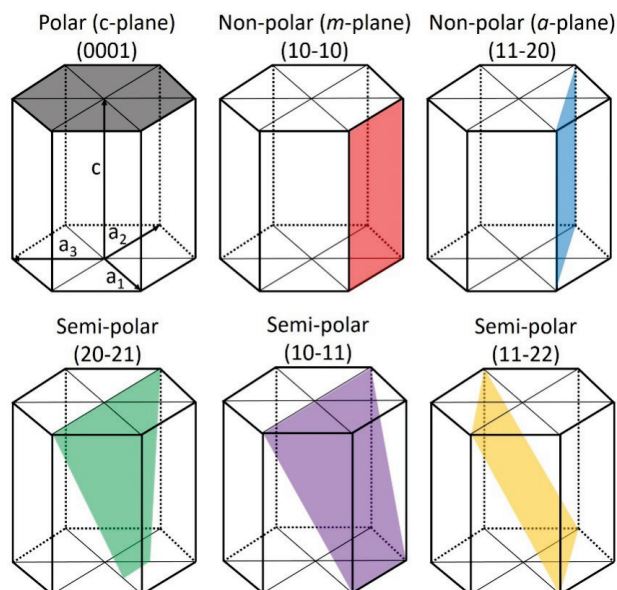


Figure 2.7: Some common growth planes of non-polar and semi-polar GaN.

GaN plane	Inclined angle to c-plane (°)
(0001)	0
(10-10)	90
(11-20)	90
(20-21)	75.09
(10-11)	61.96
(11-22)	58.41

Table 2.3: List of polar, non-polar, and selected semi-polar planes with inclined angles to the c-plane.

The mechanism of the reduced QCSE as a result of the growth along non/semi-polar orientations is due to a reduction in the built-in electrical fields as a result of their inclined angle to the c-plane. For an $\text{In}_x\text{Ga}_{1-x}\text{N}$ layer grown on GaN, the polarization generated across an InGaN/GaN quantum well structure as a function of the inclined angle θ to the c-plane is presented in Figure 2.8, where the polarizations for an $\text{In}_x\text{Ga}_{1-x}\text{N}/\text{GaN}$ quantum well structure with four different In components ($x = 0.05, 0.1, 0.15$ and 0.2) have been provided.

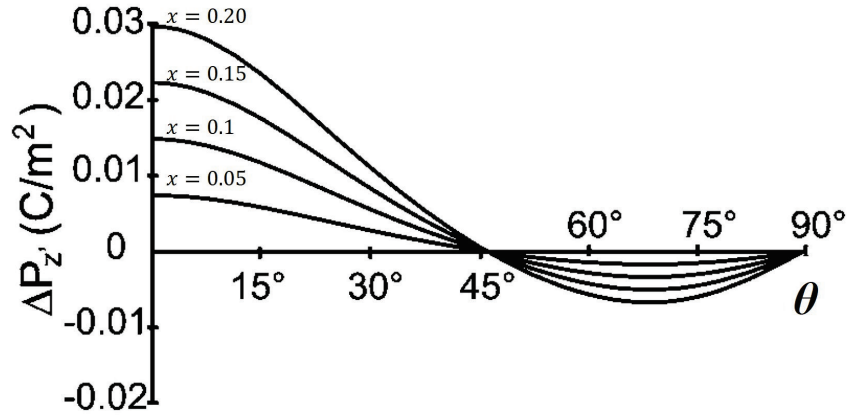


Figure 2.8: Total polarization as a function of an inclined angle to the c-plane [13].

Comparing with non-polar orientations, semi-polar orientations show some other advantages. The semi-polar (10-11) and (11-22) orientations can significantly enhance In incorporation into GaN, which enables to achieve longer wavelength (green and yellow) emitters [15]. Our group has successfully demonstrated InGaN emitters on (11-22) overgrown

GaN on sapphire substrates by a micro-rod overgrowth method [16, 17]. The emission of the LEDs cover from the green to amber spectral region, with significantly reduced efficiency droop compared to commercial c-plane LEDs. Another popular semi-polar plane is (20-21), which has been reported to facilitate the growth of InGaN quantum well structures with an improved indium homogeneity. A green LD has been demonstrated on a (20-21) free-standing GaN substrate [18]. A reduced efficiency droop has been reported for InGaN based (20-21) semi-polar LEDs [19].

2.2.4 GaN Nanowires

Apart from conventional planar GaN films, the growth of GaN NWs has also attracted extensive attention, as GaN NWs exhibit a great potential to fabricate novel optoelectronics which conventional planar III-nitride devices could not achieve. Firstly, GaN NWs with high crystal quality can be grown on lattice mismatched substrates as a result of elastic strain relaxation during growth [20]. After the growth of GaN NWs, InGaN MQWs can be grown on the sidewall of NWs to form a core-shell structure. As the GaN NWs are grown along the c-direction and the sidewalls of the NWs are non-polar orientation, QCSE can be eliminated [21]. In addition, the area of the MQWs as an active region is also increased due to the large surface to volume ratio. Alternatively, InGaN MQWs can be grown on the top of the GaN NWs, forming a disk-in-wire structure. The interface strain can be significantly relaxed laterally, effectively suppressing the QCSE [22, 23]. Furthermore, such a nanorod or nanowire structure can also be achieved by a post-growth top down fabrication technique. Our group has already demonstrated InGaN/GaN nanorod arrayed LEDs by a combination of self-organized nickel nano-masks and a subsequent dry etching process. The IQE has been significantly increased as a result of the strain relaxation [24-26].

2.3 Epitaxial Growth of GaN on Si

2.3.1 Introduction

The hexagonal six-fold surface symmetry of GaN does not match the four-fold surface

symmetry of (001) Si. Furthermore, the growth of GaN on (001) Si intrinsically forms two different in-plane orientations, leading to a rough surface morphology. Therefore, (001) silicon is not an ideal substrate for the growth of GaN. Fortunately, (111) Si has a three-fold surface symmetry which can match the hexagonal six-fold surface symmetry of GaN, leaving only one GaN in-plane orientation, as shown in Figure 2.9. Therefore, most of the GaN growth on Si uses (111) Si as substrates. The c-plane GaN grown on the (111) silicon substrate has an in-plane orientation of GaN [1-100] \parallel Si [-1-12] and GaN [11-20] \parallel Si [-110]. Under this stacking model, GaN sustains a tensile stress due to an approximately -17% lattice mismatch between GaN and Si, calculated by

$$\frac{a_{\text{GaN}} - \frac{\sqrt{2}a_{\text{Si}}}{2}}{\frac{\sqrt{2}a_{\text{Si}}}{2}} = -17\% \quad (2.1)$$

Where $a_{\text{GaN}} = 3.190\text{\AA}$ and $a_{\text{Si}} = 5.431\text{\AA}$ are the in-plane lattice constant of wurtzite GaN and cubic Si, respectively.

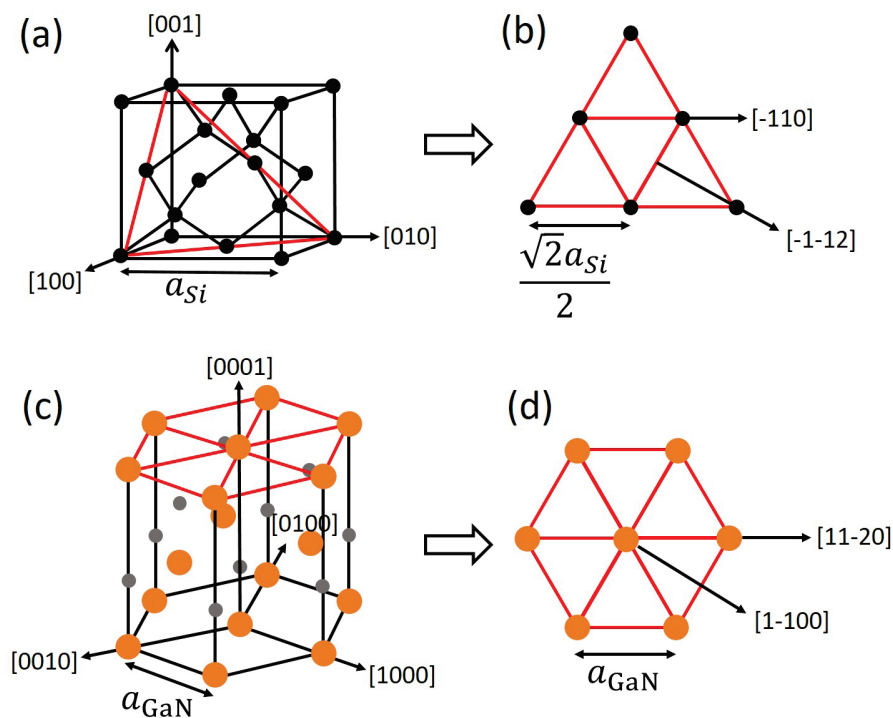


Figure 2.9: (a) cubic crystal structure of Si [1]; (b) arrangement of the Si atoms on (111) Si plane; (c) wurtzite crystal structure of GaN and (d) arrangement of the gallium atoms on (0001) GaN plane.

2.3.2 Issues of GaN Growth on Si

Melt-back Etching

When GaN is directly grown on Si substrates by MOCVD at a normal growth temperature ($>1000\text{ }^{\circ}\text{C}$), Ga reacts with Si, forming a eutectic alloy [27-29]. This reaction causes Si to out-diffuse from the substrate into GaN to deteriorate the GaN growth, roughening the surface as shown in Figure 2.10. This reaction is called ‘melt-back etching’. In order to avoid melt-back etching, an AlN buffer layer needs to be introduced to separate GaN from the Si substrate. However, if the AlN is not thick enough or there exist a number of small holes in the AlN buffer layer, the melt-back etching can start and finally creates a large number of pits on the surface [30]. Another way to avoid melt-back etching is to reduce growth temperature down to below $870\text{ }^{\circ}\text{C}$ [31], but this is not good for GaN growth as the typical growth temperature is above $1000\text{ }^{\circ}\text{C}$.

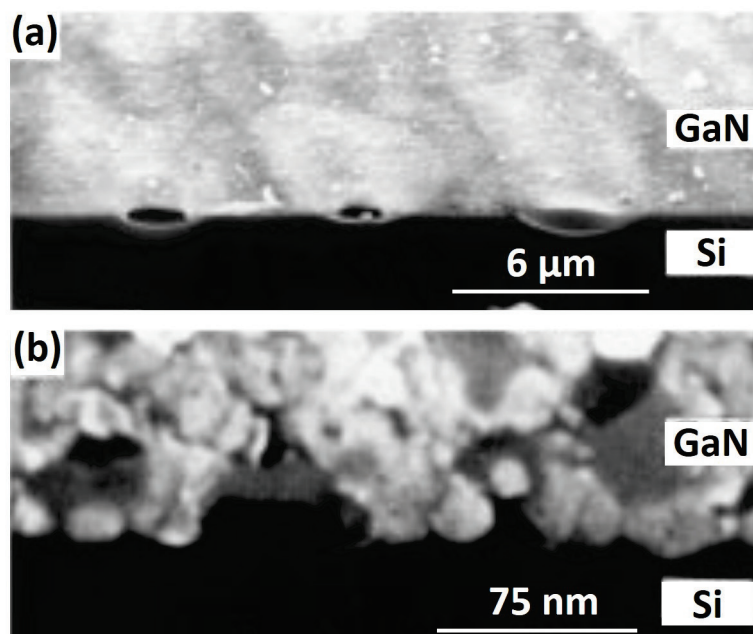


Figure 2.10: Cross sectional SEM images of melt-back etching between GaN and Si with (a) low and (b) high magnification [27].

Thermal Expansion Coefficient Mismatch

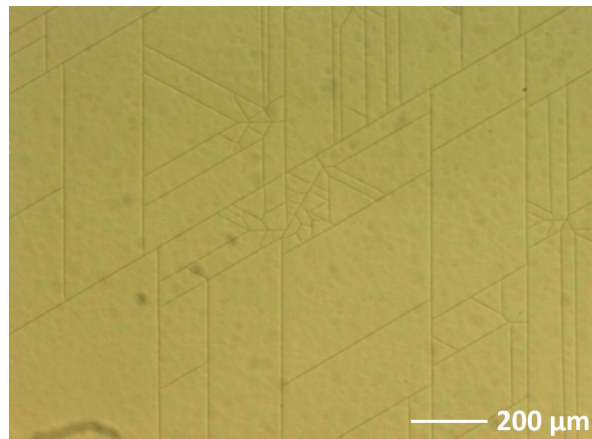


Figure 2.11: Optical microscopy image of 1.2 μm GaN grown on (111) Si with an AlN buffer.

Si has a significantly smaller thermal expansion coefficient than GaN, leading to a very large thermal expansion coefficient mismatch (115%) between GaN and Si. This large thermal mismatch introduces a tensile stress during a cooling process after the GaN growth on silicon at a high temperature. The tensile stress is increased with increasing GaN layer thickness. Generally, when GaN is thicker than 1 μm , wafer bowing and then surface cracks easily happen due to the huge tensile strain, as shown in Figure 2.11. Both the wafer bowing and the surface cracks make it difficult to fabricate LEDs [32].

Lattice Mismatch

As shown in equation (2.1), GaN grown on Si has a large lattice mismatch (-17%), which causes a high defect density, especially dislocations, in GaN films. The dislocations in InGaN/GaN MQW structures, acted as non-radiative recombination centres, reduce the IQE of the LEDs grown using such MQWs as an active region [33-35].

2.3.3 Development of GaN Growth on Si

Polar GaN

A GaN-based LED grown on a Si substrate by MOCVD was first demonstrated in 1999 [36]. A thin AlN buffer layer was first grown on (111) Si substrates before any further growth of GaN structures in order to eliminate the melt-back etching issue. However, both surface cracking and GaN crystal quality were worse than that of GaN grown on sapphire substrates. In order to eliminate surface cracking, a number of ex-situ or in-situ processes have been

performed. For the ex-situ processes, a selective area growth method was applied to the GaN growth on Si, where a Si substrate is covered by a patterned mask (usually with SiO₂ or SiN) or is etched into grooves prior to any MOCVD growth. Subsequently, a non-continuous GaN film can be directly grown on these Si substrates, as shown in Figure 2.12 [37-40]. This selective growth method can also be achieved by regrowing GaN on a thin GaN film on Si substrate with a patterned mask [41]. In this strategy, most stress can be relaxed as a result of the non-continuous GaN areas. However, the drawbacks of these ex-situ processes are also obvious. The non-continuous surface causes a severe inhomogeneity in GaN thickness, making subsequent device fabrication difficult. Moreover, melt-back etching is also a potential risk which may occur in the etched area. Therefore, an in-situ process has been introduced. By inserting different Al(Ga)N interlayers, a compressive stress is introduced to compensate the tensile stress produced during the cooling process to eliminate surface cracking. Generally, an AlGaN/AlN intermediate layer [42], AlN/GaN superlattice [43] or LT AlN interlayers [44-46] have been utilised. Comparing with the ex-situ mask approach mentioned above, the in-situ process does not require any external fabrication steps, providing a cost-effective method to eliminate surface cracking. The wafer bow due to tensile stress can also be suppressed.

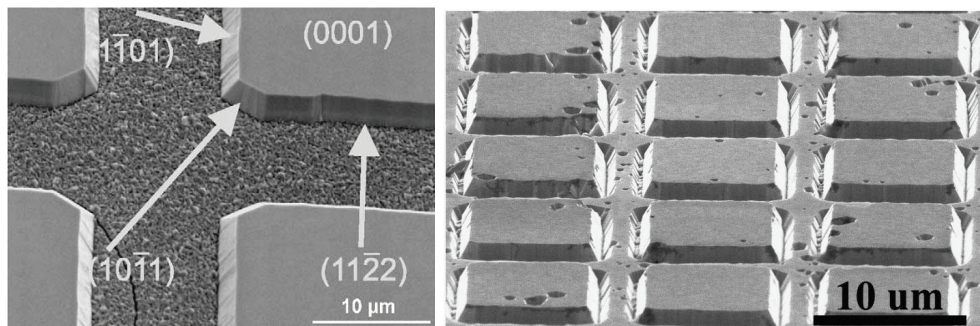


Figure 2.12: SEM images of GaN grown on masked (left) and etched (right) Si substrates [37, 40].

A number of growth approaches have been proposed and attempted in order to improve GaN crystal quality caused due to the large lattice mismatch between silicon and GaN. Generally, they can be classified as either ex-situ or in-situ methods. For the ex-situ method, Si substrate or GaN on Si is covered by patterned masks [47] or is etched into grooves [48, 49] and an epitaxial lateral overgrowth (ELOG) technique is then performed, where dislocations can bend laterally and then annihilate each other. For the in-situ method, a thin SiN interlayer is

inserted during the growth of GaN films. The SiN interlayer contains many small holes leading to the subsequent 3D growth of GaN. Similar to the ELOG, the 3D GaN growth causes dislocations to bend laterally [50, 51].

Non-polar and Semi-polar GaN

It is extremely difficult to grow non-/semi-polar GaN on any planar Si substrates. Until now, there are very few reports demonstrating semi-polar GaN grown on any planar Si substrates without any patterned features. In order to grow semi-polar GaN on any planar Si substrates, high index (11h) Si substrates have to be used [30, 52]. Semi-polar GaN with a large inclination angle to the c-axis can be grown on the Si substrate with a high index only. The highest inclination angle to the c-axis obtained for GaN on silicon is $\sim 34^\circ$, which is obtained by the growth of GaN on a (116) Si substrate. But, for even higher index Si substrates, the grown GaN will not be a single crystal any more. The challenges of GaN growth on (11h) Si are due to extreme difficulties in achieving both a smooth surface and good crystal quality.

On the other hand, for the GaN grown on patterned Si substrates, non-/semi-polar with various orientations can be realised [32, 53-58]. In order to expose $\{111\}$ Si facets for GaN selective growth so that the growth along a vertical crystal orientation can form either non-polar or semi-polar GaN, a selective and anisotropic etching technique needs to be performed on Si substrates, as illustrated in Figure 2.13. For instance, a selective and anisotropic etching process is performed on (113) silicon covered with pre-deposited stripe dielectric masks along the Si $[-2-11]$, parallel grooves with (1-11) and (-11-1) sidewalls and (011) facets between the grooves can be formed using a KOH solution, where the exposed part can be etched away until the $\{111\}$ facets are formed, as it is extremely difficult to etch the $\{111\}$ facets of silicon.

Subsequent GaN growth can take place only on the $\{1-11\}$ facets, eventually forming (11-22) GaN. For growths of any other non-/semi-polar GaN-on-Si, a SiO_2 mask is selectively deposited to cover other Si facets, only leaving one $\{111\}$ Si facet to be exposed. So far, all the reports on growth of non-/semi-polar GaN-on-Si are based on the utilization of a groove patterned Si substrate. However, for the (11-22) and (11-20) GaN-on-Si growth, such groove patterned Si substrates have a 'closed' configuration, where the Si (-11-1) facet cannot be protected from Ga flux, which increases the risk of 'Ga melting back'. Although the reaction

can be controlled under a relatively low temperature of $<870\text{ }^{\circ}\text{C}$ [31, 56], it is not suitable for GaN growth by MOCVD, which generally requires a growth temperature of above $1000\text{ }^{\circ}\text{C}$. Moreover, the stripe patterning requires a very accurate mask alignment. Any slight misalignment leads to rough $\{111\}$ Si facets and then a rough GaN surface [58].

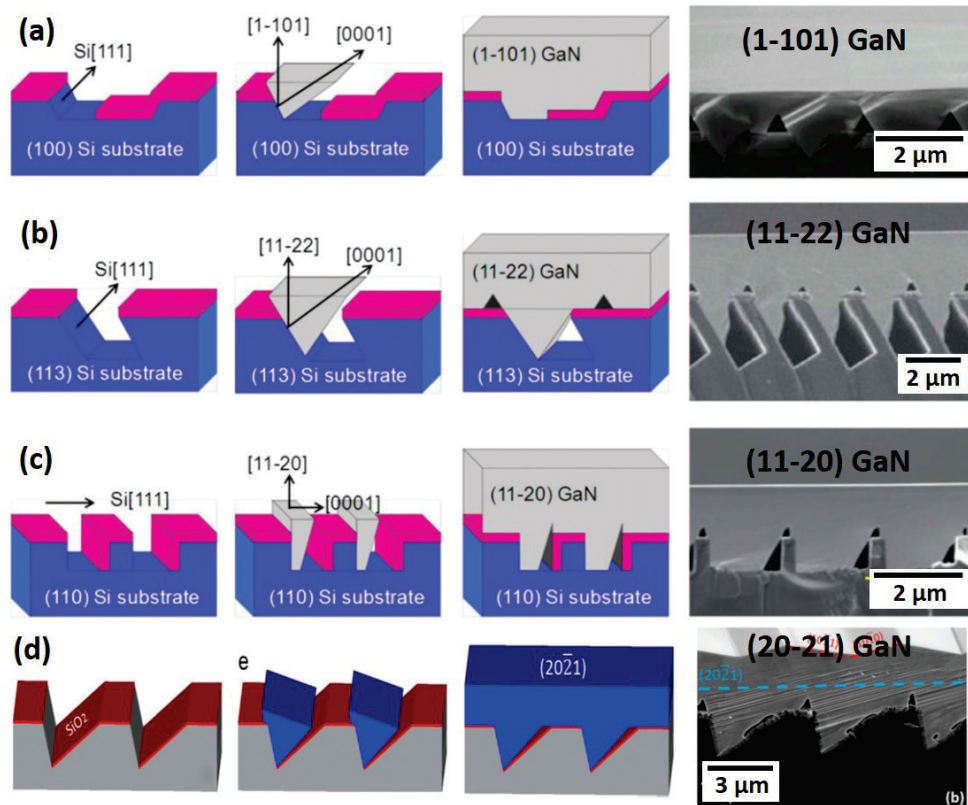


Figure 2.13: Schematics of a GaN-on-Si growth process and cross sectional SEM images of (a) (1-101) GaN on (100) Si, (b) (11-22) GaN on (113) Si, (c) (11-20) GaN on (110) Si and (d) (20-21) GaN on miscut (114) Si [32, 55].

Nanowire GaN

Basically, there are two main kinds of approaches to achieving GaN NWs or nanorods, one based on a post-growth top-down fabrication method, and another based on a direct bottom-up growth approach. For the former, our group has demonstrated nanorod arrayed LEDs with significantly improved performance, as shown in Figure 2.14 [23-25]. Firstly, a standard planar c-plane LED structure is grown on a sapphire substrate, and the sample is then dry-etched by inductively coupled plasma (ICP) into a nanorod arrayed structure using a self-assembled nickel nanomask. The technology can be directly transferred on the Si substrate as well. However, the disadvantages of the approach are due to the difficulty in further reducing the

diameter of the nanorods down to below 100 nm and the damage induced during the dry etching process.

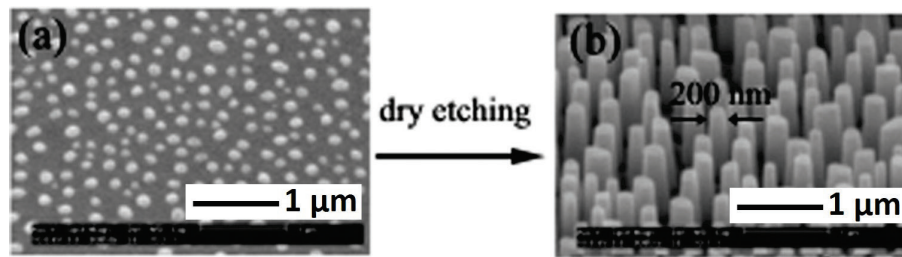


Figure 2.14: SEM images of (a) Ni masks and (b) GaN nanorod arrays [25].

For the latter approach, there are generally three methods to grow GaN NWs, namely, catalyst VLS (vapor-liquid-solid) growth, selective area growth and self-assembled growth. Unlike any planar growth of GaN on Si by MOCVD, it is difficult to grow GaN NWs on Si by MOCVD. So far, there are a limited number of reports demonstrating GaN NWs grown on Si by MOCVD for which Figure 2.15 provides a few examples [59-62], while a few groups have demonstrated some impressive results using molecular beam epitaxy (MBE) to grow NWs by means of the self-assembled method (Figure 2.15(e)) [22], although the growth mechanisms still need to be further investigated.

Generally speaking, for the growth of self-organised NWs, the growth rate along a vertical direction needs to be enhanced. In this case, compared with any standard planar GaN growth, a lower temperature would be favourable for the formation of nanowires, giving a main advantage in using MBE to grow GaN NWs. Furthermore, MBE typically uses nitrogen as a precursor for group V, where the decomposition efficiency of nitrogen molecular depends on a plasma power used instead of a growth temperature, while MOCVD uses NH_3 to supply group V element and thus a high temperature is used to crack NH_3 .

For the VLS growth, a number of different metals have been suggested as a catalyst such as gold, nickel, iron, indium and etc. [59]. But these metals can cause contamination, degrading the intrinsic electrical and optical properties of GaN NWs. Moreover, GaN NWs with inclination angles have been commonly observed. For the selective area growth method, SiO_2 or SiN is used as patterned masks [60], which can achieve straight GaN NWs with good uniformity. But this template patterning approach needs an ex-situ fabrication process. Moreover, it is difficult to reduce the diameter of the GaN NWs obtained through this method

down to below 100 nm. For the self-induced growth method, currently, only two groups demonstrate some preliminary results by MOCVD as shown in Figures 2.15 (c)&(d), where either an in-situ SiN mask or TMG pre-flowing are used, respectively [61, 62]. For the in-situ SiN mask method, a thin layer of SiN is first grown on Si by MOCVD prior to any GaN NW growth. As the SiN layer is very thin and thus does not form a continuous film, it acts as an in-situ mask for further NW growth. However, the uniformity of the GaN NWs formed is not very good and some NWs are inclined. For the TMG pre-flowing method, TMG is firstly flowed into a MOCVD reactor to form gallium droplets on which GaN NWs are grown. As shown in Figure 2.15(d), the density of GaN NWs is still low and the diameters of NWs are very large.

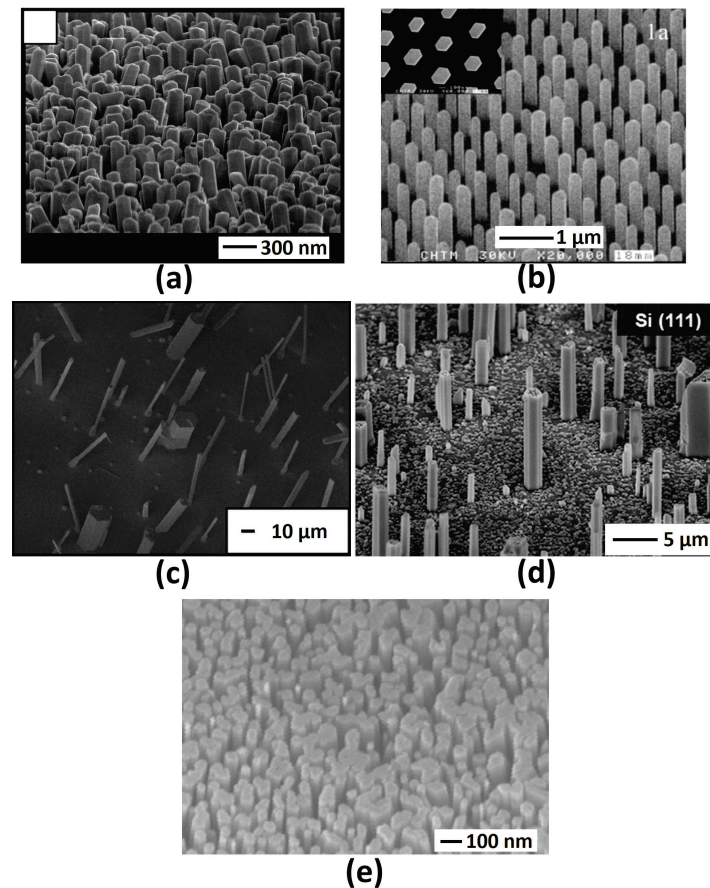


Figure 2.15: SEM images of MOCVD GaN NWs grown on Si substrates using (a) catalyst VLS growth [59], (b) patterned mask selective growth [60], (c) in-situ SiN masks [61], (d) TMG pre-flowing method [62]; and (e) SEM image of self-assembled GaN NW growth on Si by MBE [23].

References

1. J. R. Hook, and H. E. Hall, Solid State Physics (second edition) (John Wiley & Sons, West Sussex, 2010)
2. N. Costa, A. Cartaxo, and G. Sun, Advances in Lasers and Electro Optics-Chapter 13 (InTech, 2010)
3. B. A. Averill, General Chemistry: Principles, Patterns, and Applications (Flat World Knowledge, ca. 2011)
4. V. Parente, G. Campagnano, D. Giuliano, A. Tagliacozzo, and F. Guinea, *Materials* **7**, 1652 (2014)
5. Y. A. R. Dasilva, M. P. Chauvat, P. Ruterana, L. Lahourcade, E. Monroy, and G. Nataf, *J. Phys. Condens. Matter* **22**, 355802 (2010)
6. N. Das, S.H. Mousavi, S.A. Jafari Mohammadi, H. Haratizadeh, and P.W. de Oliveira, Advances in Optical Communication (InTech, 2014)
7. I. J. Bahl, Control Components Using Si, GaAs, and GaN Technologies (Artech House, London, 2014)
8. D. C. Look, and J. R. Sizelove, *Appl. Phys. Lett.* **79**, 1133 (2001)
9. D. G. Zhao, H. Yang, J. J. Zhu, D. S. Jiang, Z. S. Liu, S. M. Zhang, Y. T. Wang, and J. W. Liang, *Appl. Phys. Lett.* **89**, 112106 (2006)
10. H. Okumura, K. Ohta, G. Feuillet, K. Balakrishnan, S. Chichibu, H. Hamaguchi, P. Hacke, and S. Yoshida, *J. Cryst. Growth* **178**, 113 (1997)
11. M. Lada, A. G. Cullis, P. J. Parbrook, and M. Hopkinson, *Appl. Phys. Lett.* **83**, 2808 (2003)
12. P. Rinke, M. Winkelkemper, A. Qteish, D. Bimberg, J. Neugebauer, and M. Scheffler, *Phys. Rev. B* **77**, 075202 (2008)
13. A. E. Romanov, T. J. Baker, S. Nakamura, and J. S. Speck, *J. Appl. Phys.* **100**, 023522 (2006)
14. B. Leung, D. Wang, Y. S. Kuo, K. Xiong, J. Song, D. Chen, S. H. Park, S. Y. Hong, J. W. Choi, and J. Han, *Appl. Phys. Lett.* **104**, 262105 (2003)
15. Y. Kangawa, T. Ito, A. Koukitu, and K. Kakimoto, *Jpn. J. Appl. Phys.* **53**, 100202 (2014)
16. Y. Gong, K. Xing, B. Xu, X. Yu, Z. Li, J. Bai, and T. Wang, *ECS Trans.* **66**, 151 (2015)

17. J. Bai, B. Xu, F. G. Guzman, K. Xing, Y. Gong, Y. Hou and T. Wang, *Appl. Phys. Lett.* **107**, 261103 (2015)
18. Y. Enya, Y. Yoshizumi, T. Kyono, K. Akita, M. Ueno, M. Adachi, T. Sumitomo, S. Tokuyama, T. Ikegami, K. Katayama, and T. Nakamura, *Appl. Phys. Express* **2**, 082101 (2009)
19. Y. Zhao, S. Tanaka, C. C. Pan, K. Fujito, D. Feezell, J. S. Speck, S. P. DenBaars, and S. Nakamura, *Appl. Phys. Express* **4**, 082104 (2011)
20. J. Ristić, E. Calleja, M. A. Sánchez-García, J. M. Ulloa, J. Sánchez-Páramo, J. M. Calleja, U. Jahn, A. Trampert, and K. H. Ploog, *Phys. Rev. B* **68**, 125305 (2003)
21. R. Koester, J. S. Hwang, D. Salomon, X. Chen, C. Bougerol, J. P. Barnes, D. L. S. Dang, L. Rigutti, A. de Luna Bugallo, G. Jacopin, and M. Tchernycheva, *Nano lett.* **11**, 4839 (2011)
22. H. W. Lin, Y. J. Lu, H. Y. Chen, H. M. Lee, and S. Gwo, *Appl. Phys. Lett.* **97** 073101 (2010)
23. W. Guo, M. Zhang, A. Banerjee, and P. Bhattacharya, *Nano lett.* **10**, 3355 (2010)
24. Q. Wang, J. Bai, Y. P. Gong, and T. Wang, *J. Phys. D: Appl. Phys.* **44**, 395102 (2011)
25. J. Bai, Q. Wang, and T. Wang, *Phys. Status Solidi A* **209**, 477 (2012)
26. J. Bai, Q. Wang, and T. Wang, *J. Appl. Phys.* **111**, 113103 (2012)
27. H. Ishikawa, K. Yamamoto, T. Egawa, T. Soga, T. Jimbo, and M. Umeno, *J. Cryst. Growth* **189/190**, 178 (1998)
28. M. K. Sunkara, S. Sharma, and R. Miranda, *Appl. Phys. Lett.* **79**, 1546 (2001)
29. T. F. Ciszek, T. H. Wang, R. W. Burrows, and X. Wu, *J. Cryst. Growth* **128**, 314 (1993)
30. R. Ravash, A. Dadgar, F. Bertram, A. Dempewolf, S. Metzner, T. Hempel, J. Christen, and A. Krost, *J. Cryst. Growth* **370**, 288 (2013)
31. N. Suzuki, T. Uchida, T. Tanikawa, T. Hikosaka, Y. Honda, M. Yamaguchi, and N. Sawaki, *J. Cryst. Growth* **311**, 2875 (2009)
32. D. Zhu, D. J. Wallis, and C. J. Humphreys, *Rep. Prog. Phys.* **76**, 106501 (2013)
33. T. Hino, S. Tomiya, T. Miyajima, K. Yanashima, S. Hashimoto, and M. Ikeda, *Appl. Phys. Lett.* **76**, 3421 (2000)
34. N. G. Weimann, L. F. Eastman, D. Doppalapudi, H. M. Ng, and T. D. Moustakas, *J. Appl. Phys.* **83**, 3656 (1998)
35. D. C. Look, and J. R. Sizelove, *Phys. Rev. Lett.* **82**, 1237 (1999)

36. C. A. Tran, A. Osinski, R. F. Karlicek, and I. Berishev, *Appl. Phys. Lett.* **75**, 1494 (1999)
37. S. Zamir, B. Meyler, and J. Salzman, *Appl. Phys. Lett.* **78**, 288 (2001)
38. S. Zamir, B. Meyler, J. Salzman, F. Wu, and Y. Golan, *J. Appl. Phys.* **91**, 1191 (2002)
39. Y. Honda, Y. Kuroiwa, M. Yamaguchi, and N. Sawaki, *Appl. Phys. Lett.* **80**, 222 (2002)
40. A. Krost, and A. Dadgar, *Materials Science and Engineering B* **93**, 77(2002)
41. J. W. Yang, A. Lunev, G. Simin, A. Chitnis, M. Shatalov, M. A. Khan, J. E. Van Nostrand, and R. Gaska, *Appl. Phys. Lett.* **76**, 273 (2000)
42. H. Ishikawa, G. Y. Zhao, N. Nakada, T. Egawa, T. Jimbo, and M. Umeno, *Jpn. J. Appl. Phys.* **38**, L492 (1999)
43. E. Feltin, S. Dalmasso, P. de Mierry, B. Beaumont, H. Lahreche, A. Bouille, H. Haas, M. Leroux, and P. Gibart, *Jpn. J. Appl. Phys.* **40**, L738 (2001)
44. H. Amano, M. Iwaya, T. Kashima, M. Katsuragawa, I. Akasaki, J. Han, S. Hearne, J. A. Floro, E. Chason, and J. Figiel, *Jpn. J. Appl. Phys.* **37**, L1540 (1998)
45. A. Dadgar, J. Blasing, A. Diez, A. Alam, M. Heuken, and A. Krost, *Jpn. J. Appl. Phys.* **39**, L1183 (2000)
46. A. Krost, A. Dadgar, G. Strassburger, and R. Clos, *Phys. Stat. Sol. (a)* **200**, 26 (2003)
47. W. Ju, D. A. Gulino, and R. Higgins, *J. Cryst. Growth* **263**, 30 (2004)
48. A. Strittmatter, S. Rodt, L. Reissmann, D. Bimberg, H. Schroder, E. Obermeier, T. Riemann, J. Christen, and A. Krost, *Appl. Phys. Lett.* **78**, 727 (2001)
49. H. Naoi, M. Narukawa, H. Miyake, and K. Hiramatsu, *J. Cryst. Growth* **248**, 573 (2003)
50. A. E. Romanov, and J. S. Speck, *Appl. Phys. Lett.* **83**, 2569 (2003)
51. D. M. Follstaedt, S. R. Lee, P. P. Provencio, A. A. Allerman, J. A. Floro, and M. H. Crawford, *Appl. Phys. Lett.* **87**, 121112 (2005)
52. R. Ravash, J. Blaesing, A. Dadgar, and A. Krost, *Appl. Phys. Lett.* **97**, 142102 (2010)
53. T. Tanikawa, T. Hikosaka, Y. Honda, M. Yamaguchi, and N. Sawaki, *Phys. Stat. Sol. (c)* **5**, 2966 (2008)
54. M. Yang, H. S. Ahn, T. Tanikawa, Y. Honda, M. Yamaguchi, and N. Sawaki, *J. Cryst. Growth* **311**, 2914 (2009)
55. M. Khoury, M. Leroux, M. Nemoz, G. Feuillet, J. Zuniga-Perez and P. Vennegues, *J. Cryst. Growth* **419**, 88 (2015)

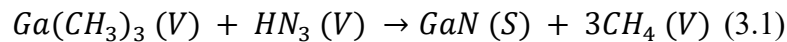
56. T. Tanikawa, N. Suzuki, Y. Honda, M. Yamaguchi and N. Sawaki, *Phys. Stat. Sol. (c)* **7**, 1760 (2010)
57. T. Hikosaka, T. Tanikawa, Y. Honda, M. Yamaguchi and N. Sawaki, *Phys. Stat. Sol. (c)* **5**, 2234 (2008)
58. M. Pristovsek, Y. Han, T. Zhu, M. Frentrup, M. J. Kappers, C. J. Humphreys, G. Kozlowski, P. Maaskant, and B. Corbett, *Phys. Stat. Sol. (b)* **252**, 1104 (2015)
59. Y. H. Ra, R. Navamathavan, and C. R. Lee, *CrystEngComm* **14**, 8208 (2012)
60. S. D. Hersee, X. Sun, and X. Wang, *Nano lett.* **6**, 1808 (2006)
61. B. Foltynski, C. Giesen, and M. Heuken, *Phys. Stat. Sol. (b)* **252**, 1132 (2015)
62. S. M. Ko, J. H. Kim, Y. H. Ko, Y. H. Chang, Y. H. Kim, J. Yoon, J. Y. Lee, and Y.H. Cho, *Cryst. Growth Des.* **12**, 3838 (2012)

Chapter 3

Equipment

3.1 Metal-Organic Chemical Vapour Deposition

A MOCVD system or named as a Metalorganic Vapour Phase Epitaxy (MOVPE) system has been widely used in growth of semiconductor epiwafers. MOCVD utilises a number of chemical reaction processes to deposit a high purity and quality epitaxial layer. The basic principle of MOCVD growth is: gaseous reagents, which consist of group V precursors and group III precursors, are fed into a reactor chamber and chemically react with each other on a substrate whose temperature can be accurately controlled. By controlling reagent types and flow rates, substrate temperatures and reactor chamber pressure, both the composition and thickness of epitaxial layers can be controlled very accurately. For III-nitride MOCVD growth, six reagents are typically used. NH_3 is used as a precursor for group V, while Trimethylgallium (TMG), Trimethylaluminium (TMA), Trimethylindium (TMI) are employed as the precursors of group III. Disilene (Si_2H_6) and Bis(cyclopentadienyl)magnesium (CP_2Mg) are used for a n-type dopant and a p-type dopant, respectively. In addition, there are two types of carrier gas: H_2 and N_2 . Since H_2 is the smallest molecule, it can be purified very well and is generally used as a carrier gas for MOCVD growth. N_2 is typically used as a carrier gas for InGaN/GaN growth, as the rate of indium incorporating into GaN is very low under H_2 ambient. The chemical reaction for GaN epitaxial vapour phase growth is illustrated below [1]:



where (V) denotes a vapour state and (S) signifies a solid state.

3.1.1 Main Configuration

There are two main types of MOCVD reactor configurations, a horizontal reactor and a vertical reactor. Except a difference in reactor structure, both the control units and the pipe configurations of the two kinds of MOCVD are very similar. Our MOCVD has a vertical

reactor. Figure 3.1 shows the main body of our MOCVD. It contains the gas delivery cabinet, reactor cabinet, load lock, in-situ monitoring system and a control panel. Apart from the main body, there are carrier gas purifiers, an ammonia scrubber and an exhaust pump. According to different functions, the MOCVD system can be divided into five parts: gas purifiers, MO source bubblers, gas delivery systems, reactor systems and exhaust systems.



Figure 3.1: The main body of our MOCVD.

3.1.2 Gas Purifiers

For III-nitride MOCVD growth, both H_2 and N_2 need to be purified before flowing into the MOCVD gas delivery system.

H_2 purifier: A palladium diffusion cell is used for H_2 purification. By heating up a palladium membrane to ~ 300 °C, only H_2 which has the smallest diameter can pass through the palladium crystal lattice, leaving any impurities to go through a bleed gas line, as shown in Figure 3.2.

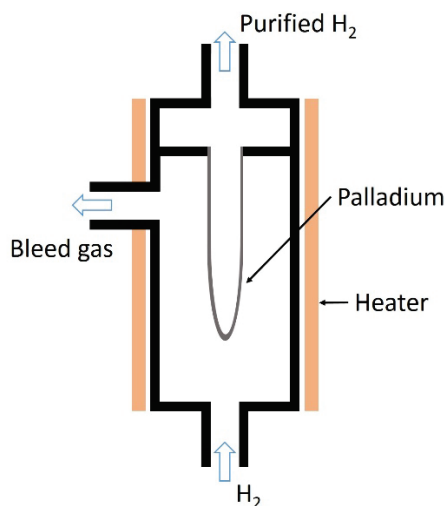


Figure 3.2: Schematic drawing of H₂ purifier.

N₂ purifier: A nanochem purification cell is used for N₂ purification. This Nanochem cell can generally remove H₂O, O₂ and CO₂ [2]. Comparing with any standard H₂ purifier which can only allow H₂ to pass through, a N₂ purifier is still less efficient. Therefore, H₂ is used as a carrier gas for MOCVD growth.

NH₃: The NH₃ used by our group is white NH₃ [3]. It has a very high purity grade (99.99999%). Therefore, the NH₃ can be directly used without any further purifying.

3.1.3 MO Source Bubbler

Each MO source is contained in a stainless steel bubbler in a liquid state except TMI and Cp₂Mg which are in a solid state. Each bubbler is stored in a water bath whose temperature can be accurately controlled. The pressure inside each bubbler is also controlled by a pressure controller. Each MO source is extracted from its bubbler by using a carrier gas, either H₂ or N₂. The basic configuration of a bubbler is shown in Figure 3.3. MFS stands for a mass flow controller, which controls a gas flow rate. PC represents a pressure controller which controls the pressure of the bubbler. A carrier input is located near the bottom of a bubbler, and a carrier output is located near the top of the bubbler. When a MO source is required for epitaxial growth, a carrier gas is flowed into the bubbler through the input pipe to push the MO source (i.e., precursor) out of the bubbler. A thermal tape is wound around the output line to warm up the output, eliminating condensation. For a solid-state source such as TMI, the input and out lines are connected with the bubbler in a reversed direction [4].

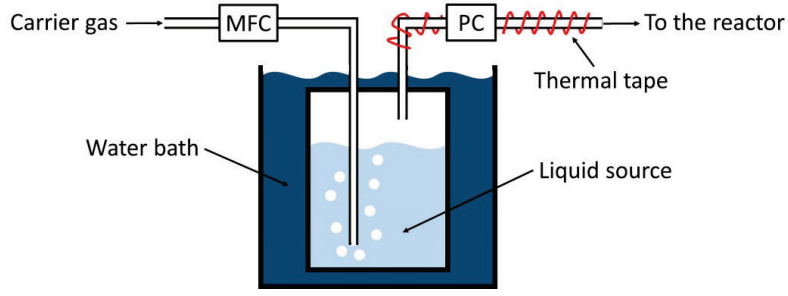


Figure 3.3: Schematic diagram of a MOCVD bubbler.

The vapour partial pressure of a MO source is determined by the temperature of the MO source temperature, which is controlled by the bubbler water bath. The relationship between the MO source vapour partial pressure and the MO temperature can be expressed:

$$\text{Log}(p_{\text{partial}}) = B - \frac{A}{T} \quad (3.2)$$

where p_{partial} is the vapour partial pressure of a MO source in torr, A and B are constants [5-7] and T is the temperature in Kelvin. For a Cp_2Mg source, the vapour partial pressure is slightly different as below [8]:

$$\text{Log}(p_{\text{partial}}) = B - \frac{A}{T} - 2.18 \ln T \quad (3.3)$$

The vapour partial pressures for our MOCVD sources have been given in Table 3.1

Bubbler source	Bubbler temperature (K)	A	B	p_{partial} (torr)	p_{bubbler} (torr)
TMG _{1,2}	273	1703	8.07	67.91	1300
TMA ₁	291	2134	8.22	7.70	1500
TMA ₂	294	2134	8.22	9.15	1500
TMIn _{1,2}	303	3204	11.00	2.67	1000
Cp ₂ Mg	303	4198	25.14	0.07	900

Table 3.1 Vapour partial pressure of our MOCVD sources [5-8].

Based on an idea gas law, the mole flow rate of a MO source can be calculated below:

$$f_{\text{MO}}(\text{mole}/\text{min}) = \frac{f_{\text{carrier gas}}(\text{sccm})}{22400(\text{scc}/\text{mole})} \cdot \frac{P_{\text{partial}}(T)}{P_{\text{bubbler}} - P_{\text{partial}}(T)} \quad (3.4)$$

where f_{MO} is the mole flow rate of the MO source used, $f_{carrier\ gas}$ is the flow rate of the carrier gas used, $p_{partial}$ is the vapour partial pressure of the MO source used and $p_{bubbler}$ is the bubbler pressure.

3.1.4 Gas Delivery System

A basic gas delivery system is schematically illustrated in Figure 3.4. In order to prevent a pre-reaction, ammonia and MO sources are supplied to a reactor chamber through two separate pipes, and then mix just above a susceptor on a heater. The manifold is used to switch MO sources between a vent line and a reactor line.

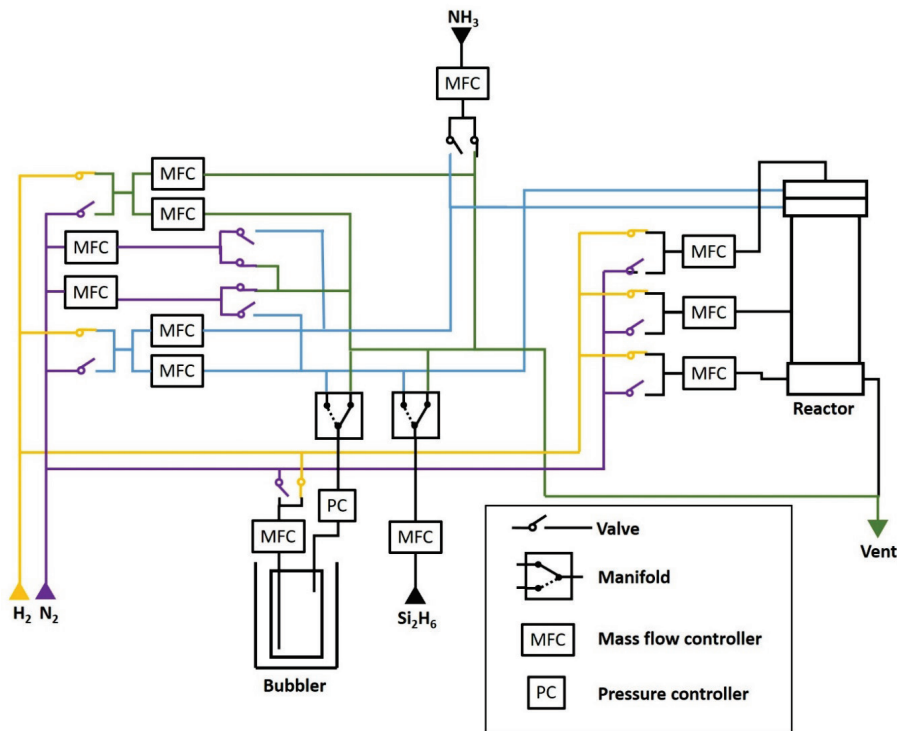


Figure 3.4: Schematic diagram of a MOCVD gas delivery system.

3.1.5 Reactor System

A Thomas Swan 3×2” vertical reactor system with a close-coupled showerhead is used for the project. The basic configuration of our reactor is schematically illustrated in Figure 3.5. The reactor is made of stainless steel, providing a completely sealed chamber where pressure, temperature and gas input/output can be controlled accurately. The stainless steel chamber closure is at the base with a sealing flange. The sealing flange has double ‘O’ rings. When the

chamber is closed, the volume between the two 'O' rings is evacuated and the pressure is checked by a pressure sensor. The ammonia and MO sources are introduced into the showerhead in the chamber through separate pipe lines (which are called injectors) in order to suppress pre-reaction issues. Both the showerhead and the stainless steel chamber are water cooled. The injectors on the showerhead are positioned less than 2cm above a heated susceptor, which gives a good convection and laminar flow with minimal turbulence. On the showerhead, there are four optical access ports to allow us to install in-situ monitoring systems. During the growth, an in-situ laser can pass through the ports to monitor the whole growth process. In addition, these optical ports are also used for the temperature calibration by inserting optical probes to measure the surface temperature of wafers.

Three wafers each with a diameter of two inches are placed in three-recessed pockets on the susceptor. The susceptor is made of graphite coated with SiC. The graphite susceptor has a good thermal conductivity and the SiC coat can prevent a reaction between ammonia and graphite at high temperature. The susceptor stands on a quartz-made glass wall and is rotated at 100rpm by a rotator to achieve good uniformity of a wafer during growth. The susceptor is heated by a heater coil with three radial zones. By adjusting the electrical power in each zone, high temperature uniformity can be achieved. At the centre of the heater, a thermocouple is mounted below the susceptor to monitor growth temperatures. With a computer proportional–integral–derivative feedback system, the growth temperature given by thermocouple is stably controlled. Between the susceptor and the stainless steel chamber wall, a second glass wall is placed to avoid any deposition on the chamber wall.

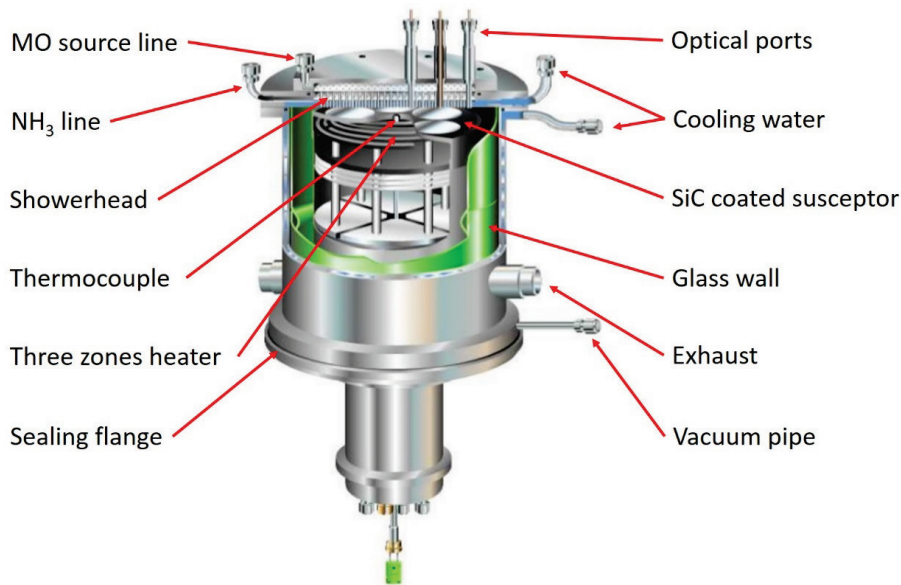


Figure 3.5: MOCVD reactor configuration [9].

In order to eliminate any dead volumes in the chamber, several purge lines are connected to the optical ports and the space between the second glass wall and the steel chamber in order to supply either H_2 or N_2 , depending on growth conditions. In order to keep the heater clean and protect it at high temperatures, H_2 is used to purge the heater through a purge line during growth.

3.1.6 Exhaust System

A reactor exhaust system is firstly connected to a pre-filter which contains 10mm diameter steel balls for trapping large particles. Then, it passes through a pyrolysis furnace to crack the residual MO-sources. The pyrolysis furnace works at a temperature of 350 °C. Next, a pall filter is used to trap small particles. The pall filter has a pore size on a μm scale. Subsequently, an Ebara dry vacuum pump is connected to draw all gases through a gas delivery system, which are through a stainless steel pipe to connect a NH_3 scrubber. Since NH_3 is toxic and harmful to the environment, NH_3 is decomposed into H_2 and N_2 in the scrubber by a heated catalyst and finally released to air.

3.2 Nomarski Optical Microscope

Unlike standard optical microscope, a Nomarski optical microscope utilises the principle

of optical interferometry, which can produce a magnified three-dimensional image of a sample surface. The basic structure of a Nomarski optical microscope is shown in Figure 3.6.

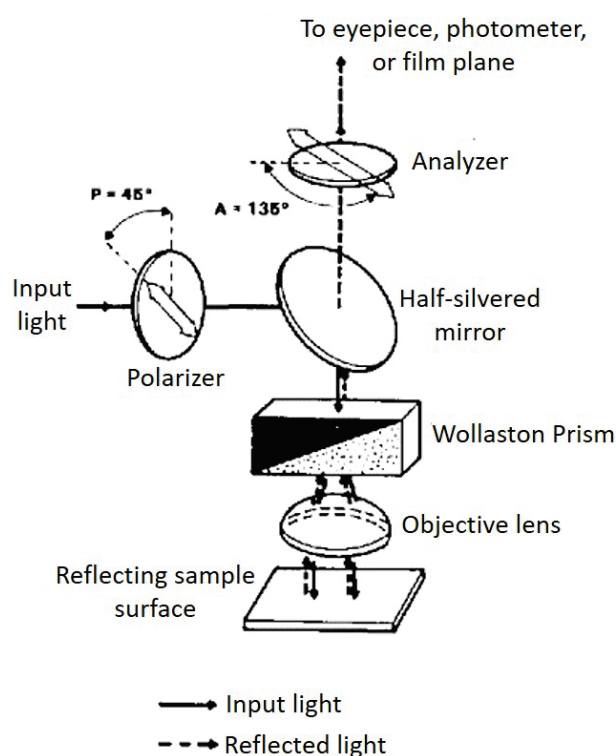


Figure 3.6 Schematic diagram of a Nomarski Optical microscope [10].

The light from an incandescent source is firstly polarized by a polarizer, and is then split into two orthogonally polarized beams by a Wollaston Prism. Next, the two beams are focused by an objective lens and are incident on any two adjacent points of a sample surface. Due to the variation in either the refractive indices or the thickness of the two adjacent points of the sample surface, the two reflected beams have different optical path lengths. Subsequently, the two beams are focused by an objective lens and then mix on the Wollaston Prism. Finally, the mixed beams pass through an analyser and then produce an optical interference on an eyepiece plane. Since the optical interference is sensitive to the optical path difference, any variation in the refractive index or the thickness of the sample surface can be converted into a brightness variation, providing a three-dimensional appearance of the sample surface. Therefore, compared with the conventional optical microscope, the Nomarski optical microscope can observe sample surface with a better resolution and emphasised lines and edges on the sample surface. Moreover, on my experiment samples, there are many materials are transparent for visible light such as AlN, GaN, SiO₂ and some surface contaminations. The Nomarski optical

microscope can observe them much clearly than the conventional optical microscopy.

3.3 Scanning Electron Microscope

The scanning electron microscope (SEM) is a powerful tool to characterise a semiconductor surface with a high magnification. Figure 3.7 (b) shows a schematic configuration of the SEM. An electron beam is generated from a field emission gun with a high voltage of 1-30 kV. The electron beam is collimated and focused by magnetic lenses. An objective aperture can also be installed to narrow the electron beam. The well-focused electron beam is incident on a sample surface, producing secondary electrons. These secondary electrons are collected and detected by a detector which can convert them into electrical signals. By sweeping the focused electron beam on a sample surface one point at a time in a rectangular scanning area, an image of sample surface is generated by processing all the electrical signals from the detector.

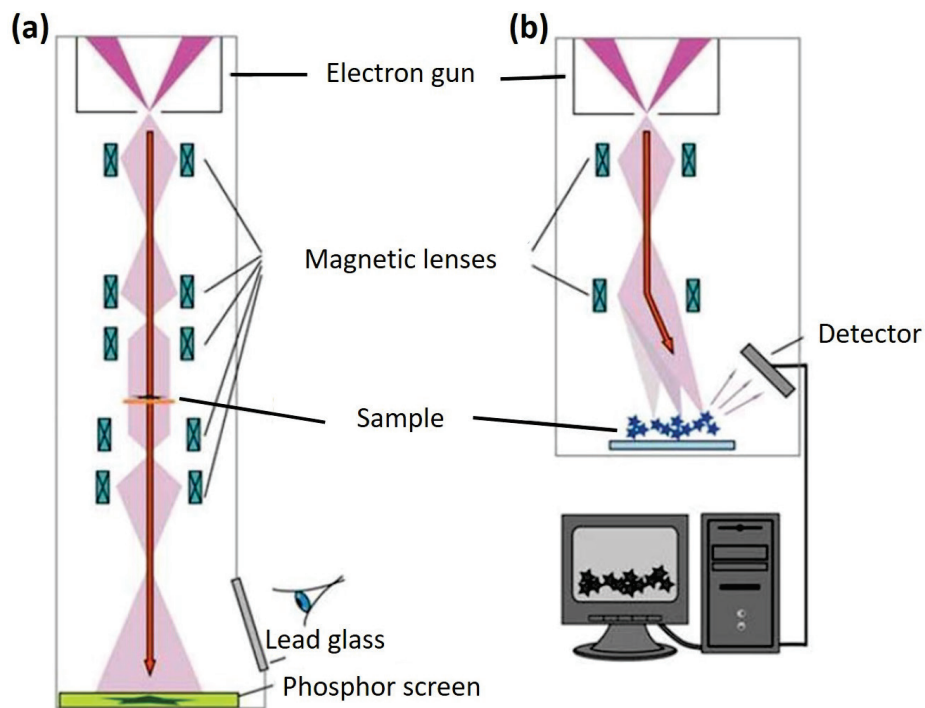


Figure 3.7: Schematic diagrams of (a) TEM and (b) SEM [11].

Comparing with any standard optical microscope, an SEM has a much higher resolution and can create top-down, angular and cross-sectional images by tilting a motorised sample stage. However, there are some drawbacks for SEM measurements. SEM measurements have

to be performed under a high vacuum in order to minimize electron scattering, typically 5×10^{-5} mBar. The sample measured should be conductive, otherwise the electrons will be easily charged on the sample surface, leading to severe degradation in the quality of images. In this study, a Philips FEGSEM XL30 SEM system is used, which can be operated at accelerating voltage from 0.2 to 30 kV and has a resolution down to 2 nm.

Apart from the secondary electrons, back scattered electrons and X-rays can be used to perform energy dispersive X-ray measurements which can investigate the chemical composition of a sample.

3.4 Transmission Electron Microscope

Similar to the SEM, the transmission electron microscope (TEM) is a microscopy technique which also utilizes an energetic electron beam to characterize the microstructure of sample. As shown in Figure 3.7 (a), in the TEM system, an electron beam generated from electron gun is focused by magnetic lenses and is then transmitted through an ultra-thin sample. The electron beam interacts with sample to generate an image. Finally, the formed image is focused and magnified on a fluorescent screen or a charge-coupled device (CCD) camera. With the benefit of the short wavelength of electrons, a TEM has an extremely high resolution. In this study, a Philips EM 430 TEM system is used, which operates from 50 to 300 kV. It can magnify sample up to 750,000 times and has a point resolution down to 0.23 nm. Consequently, TEM allows us to investigate the microstructure of a sample, such as crystal orientations, crystal defects, etc. In order to prepare an ultra-thin sample suitable for TEM measurements, a standard procedure is to use combined mechanical lapping and then an ion milling process, which can reduce the thickness of a sample down to 100 nm.

3.5 High Resolution X-ray Diffraction

A high resolution X-ray diffraction (HR-XRD) system is a powerful system to non-destructively investigate the crystal structure, the crystal quality and the chemical composition of a sample. The basic principle of XRD measurements is due to Bragg's law [12]:

$$2 \cdot d \cdot \sin\theta = n \cdot \lambda \quad (4.1)$$

where d is the inter-planar atom distance, θ is the incident angle, λ is the X-ray wavelength and n is an integer. As a result of the periodic structure of a crystal which looks like a grating, X-ray beams are incident on the surface of the crystal and are then scattered by the crystal as schematically illustrated in Figure 3.8, generating a constructive interference at a number of certain incident angles which need to meet Bragg's law.

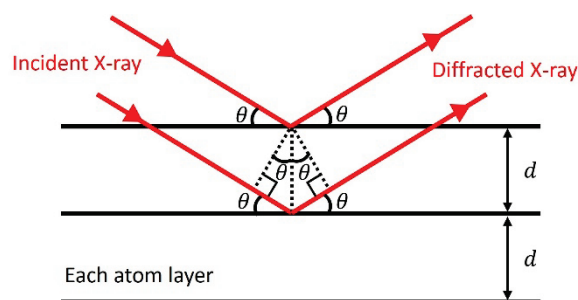


Figure 3.8: Schematics of X-ray diffraction.

In this study, a BRUKER D8 DISCOVER HR-XRD system is used, which consists of a X-ray tube, an incident X-ray optics unit, a sample stage, a secondary optics unit and a X-ray diffraction detector. X-ray beams are generated by the X-ray tube, where a focused electron beam is accelerated by applying a high voltage field to bombard a target material. The target material used in our HR-XRD is Cu and the corresponding X-ray wavelength is 1.5418 Å. Before the x-ray beam is incident on a sample, the X-ray beam passes through the X-ray optics unit consisting of a Göbel mirror, a monochromator and a divergence slit. The Göbel mirror is used to collimate the X-ray beam; and the monochromator is made of a channel-cut Ge crystal to enhance the spectral resolution; and the divergence slit is used to limit the divergence of the X-ray beams. The diffracted X-ray beam passes through the secondary optics unit and is detected by the detector. The secondary optics unit contains similar components to the incident X-ray optics unit. Depending on the resolution required, the secondary optics unit with different components can be chosen, which gives an angular resolution down to 0.01°. As shown in Figure 3.9, an incident angle is denoted by ω and a diffraction angle is labelled as 2θ . The motorized sample stage also can be rotated and tilted as angle ϕ and χ respectively.

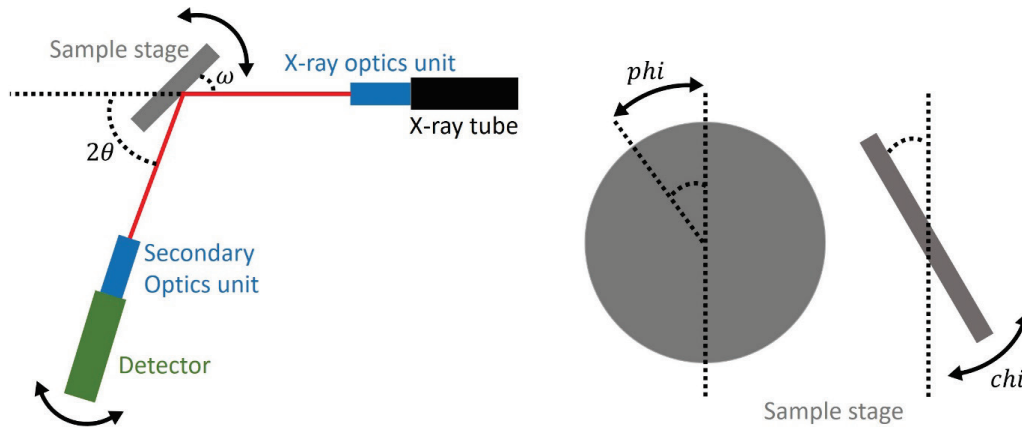


Figure 3.9: XRD basic configuration and sample stage movement.

For XRD measurements on III-nitride semiconductors, the Bragg angles of III-nitrides can be easily calculated based on Bragg's law. The measurements of XRD rocking curves are generally used to evaluate the crystal quality of a semiconductor [12]. By moving both the sample stage and the detector simultaneously, the incident and diffraction angles of a semiconductor are set to its corresponding Bragg angles. XRD rocking curve measurements can be performed by measuring the diffraction intensity as a function of ω angle. A narrow full width half maximum (FWHM) of a rocking curve means a high crystal quality. The XRD measurements performed in a $\omega - 2\theta$ mode is used to provide the information about the chemical composition and the crystal orientation of a crystal.

3.6 Photoluminescence

Photoluminescence (PL) spectroscopy has been widely used to investigate optical properties of semiconductors. When a laser as an excitation source is incident on a semiconductor sample, the laser is absorbed by the semiconductor assuming that the photon energy of the laser is higher than that of the bandgap of the semiconductor. The electrons in the valence band are then excited to the conduction band, leaving the holes in the valence band. These excited electrons in the conduction band, which are unstable, will fall back to the valence band and then recombine with the holes, releasing photons. If a semiconductor contains a number of defects such as dislocations which may serve as non-radiative recombination centers, these defects significantly affect the optical properties of the semiconductors, which can be investigated by PL. By measuring the PL spectrum of a sample, the band gap, the alloy

composition, the crystal defects, the QCSE and the strain of the sample can be investigated.

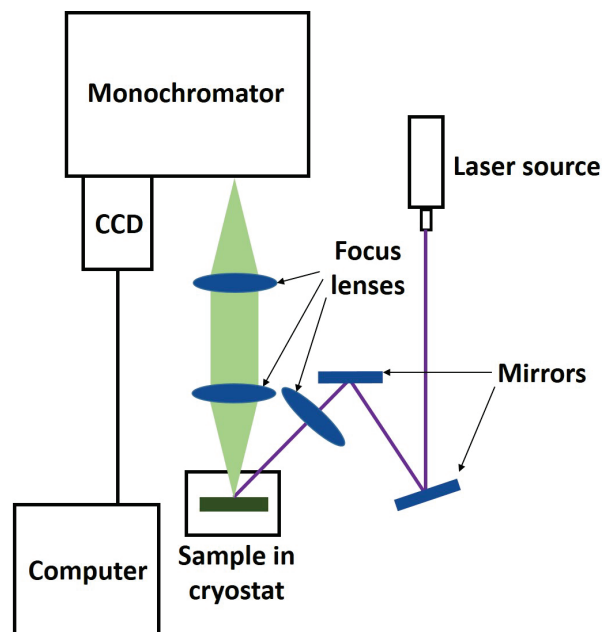


Figure 3.10: Schematic diagram of a PL system.

Figure 3.10 shows schematics of a PL system. In the system which the project uses, either a 405nm continuous wave (CW) diode laser is used as an excitation source for InGaN samples or a 325 nm He-Cd laser as an excitation source for measuring GaN. The laser beam is reflected by an Aluminium mirror with >99% reflectivity and then focused using a lens on a sample. The laser beam can go down to approximate 200 μm diameter. The luminescence from the sample is collected and collimated by a pair of 2 inch lenses, and is then introduced to an entrance slit of a 0.75 m Jobin Yvon SPEX monochromator. The luminescence is then dispersed by the monochromator and detected by a thermoelectrically cooled CCD detector. For low temperature or temperature dependent PL measurements, samples are held in a helium closed-cycle cryostat, where the temperature of the samples can be controlled from 10 to 300 K. For excitation power dependent PL measurements, the laser power can be continuously tuned through a variable attenuator located in front of the laser.

References

1. G. S. Solomon, D. J. Miller, M. Ramsteiner, A. Trampert, O. Brandt, and K. H. Ploog, *Appl. Phys. Lett.* **87**, 181912 (2005)
2. C. Ma, A. M. Haider, and F. Shadman, *Transactions on Semiconductor Manufacturing* **6**(4),361-366 (1993)
3. <http://www.airproducts.com/~media/downloads/a/ammonia-nh3/data-sheets/en-led-ammonia-white-datasheet.pdf?productType=Gases&productLevel1=Specialty-Gases&productLevel2=Silicon-Semiconductors&productLevel3=Ammonia-NH3>
4. R. Odedra, A. J. Kingsley, T. Leese, A. Purdie, K. M. Coward, L. M. Smith, S. A. Rushworth, G. Williams, and R. K. Kanjolia, *16th International Conference on Indium Phosphide and Related Materials* (2004)
5. https://www.akzonobel.com/hpmpo/system/images/AkzoNobel_TMGa%20SSG_hpmpo_glo_eng_pds_tcm36-18136.pdf
6. https://www.akzonobel.com/hpmpo/system/images/AkzoNobel_TMAI%20SSG_hpmpo_glo_eng_pds_tcm36-18134.pdf
7. https://www.akzonobel.com/hpmpo/system/images/AkzoNobel_TMIn%20SSG_hpmpo_glo_eng_pds_tcm36-18135.pdf
8. https://www.akzonobel.com/hpmpo/system/images/AkzoNobel_Cp2Mg%20SSG_hpmpo_glo_eng_pds_tcm36-18205.pdf
9. Thomoas Swan CCS-MOCVD Reactor System Manual by Thomoas Swan Scientific Equipment LTD (2007)
10. J. S. Hartman, R. L. Gordon, and D. L. Lessor, *Applied optics* **19**, 2998 (1980)
11. S. A. Aseyev, P. M. Weber, and A. A. Ischenko, *Analytical Sciences, Methods and Instrumentation* **3**, 30 (2013)
12. M. A. Moram, and M. E. Vickers, *Rep. Prog. Phys.* **72**, 036502 (2009)

Chapter 4

Fabrication of Patterned Si Substrates

4.1 Introduction

This chapter introduces two kinds of patterned Si substrate fabrication technologies for subsequent semi-polar (11-22) and (20-21) GaN growths. Firstly, Si substrates with different orientations are analysed in order to select suitable Si substrates for the pattern fabrication. Next, the two Si substrate patterning processes are described in Chapter 4.3 and Chapter 4.4, separately.

The first approach to patterned Si fabrication is to create inverted-pyramid patterns for semi-polar (11-22) GaN growth. Comparing with the stripe patterns used by other groups (introduced in Chapter 2.3.3), this method can address one of the most challenging issues for the growth of semi-polar GaN on silicon substrates, namely melt-back etching [1-4]. Moreover, as the selective growth area is small and non-continuous, the thermal stress between GaN and Si is reduced [5], leading to an almost crack-free surface of a GaN layer with a thickness of ~ 3 μm . Furthermore, the lateral growth along the $\langle 1-100 \rangle$ direction also results in a further reduction in dislocation density. All of these advantages are discussed in detail in Chapter 5.

The second approach to patterned Si fabrication is to produce stripe patterns for the semi-polar (20-21) GaN growth. Comparing with any other stripe patterning approaches (introduced in Chapter 2.3.3), our novel approach with an extra feature gives (20-21) GaN with much better crystal quality, especially a great reduction in BSF density. In addition, the resultant GaN stripe structure using our approach exhibits a semi-polar (10-11) top surface and excellent parallel sidewalls which could be used as an optical cavity. This would be advantageous for LD device realization. In order to eliminate the melt-back etching issue, our stripe patterns have been further optimised by introducing a number of extra gaps to truncate the stripe patterns, which allow NH_3 to fully cover all exposed Silicon areas in order to effectively prevent the melt-back etching. The GaN growth on such stripe patterned Si substrates is discussed in Chapter 6.

4.2 Selection of Si Substrate Orientation

Since it is extremely difficult to directly grow semi-polar (11-22) or (20-21) GaN on any planar Si substrate, GaN has to be grown on an inclined Si facet, leading to a semi-polar orientation along the vertical direction. As discussed in Chapter 2.3.1, the (111) Si plane matches the hexagonal six-fold symmetry of GaN, facilitating growth of a GaN film with a single orientation. As a result, in order to achieve semi-polar GaN with either (11-22) or (20-21) orientation upward, GaN has to be grown on an inclined {111} Si facet along the c-direction. However, the inclination angle between any of the {111} Si facets and the Si substrate surface should be equal to the inclination angle between the semi-polar plane and the c-plane of GaN (shown in Table 2.3). The angles between different silicon {111} planes and the surface of differently orientated silicon substrates for common Si substrates are provided in Table 4.1. It has been found that the (113) Si substrate is suitable for semi-polar (11-22) and (20-21) GaN growth, as the angles between some {111} Si planes and the (113) silicon substrate surface are close to the proper inclination angles for the growth of semi-polar (11-22) GaN and (20-21) GaN (highlighted in red colour in Table 4.1). In order to achieve semi-polar (11-22) GaN, GaN needs to be grown on either the (-111) or the (1-11) Si facet of a (113) Si substrate, and the resultant GaN with a vertical direction which is 58.52° inclined to c-direction. Compared with Table 4.1, an offset angle is negligibly small:

$$58.52^\circ - 58.41^\circ = 0.11^\circ$$

However, for semi-polar (20-21) GaN, GaN is grown on (-1-11) Si facet of a (113) Si substrate along the c direction. The inclination angle of the resultant semi-polar (20-21) GaN grown on this facet is 79.98° . Based on Table 4.1, an offset angle is:

$$79.98^\circ - 75.09^\circ = 4.89^\circ$$

In order to achieve true semi-polar (20-21) GaN, a (113) Si substrate with a small miscut angle needs to be used to compensate this offset angle.

{111} Si planes			Angles between Si {111} planes and Si substrate surface with different orientation			
h	k	l	(100)	(110)	(112)	(113)
1	1	1	54.74°	35.26°	19.47°	29.50°
-1	1	1	125.26°	90.00°	61.87°	58.52°
1	-1	1	54.74°	90.00°	61.87°	58.52°
1	1	-1	54.74°	35.26°	90.00°	100.02°
-1	-1	1	125.26°	144.74°	90.00°	79.98°
1	-1	-1	54.74°	90.00°	118.13°	121.48°
-1	1	-1	125.26°	90.00°	118.13°	121.48°
-1	-1	-1	125.26°	144.74°	160.53°	150.50°

Table 4.1: Angles between {111} Si planes and Si substrate surface.

4.3 (113) Si Substrates with Inverted-pyramid patterns

4.3.1 Methodology

Our whole patterning process is schematically illustrated in Figure 4.1. A SiO₂ layer is initially deposited on a (113) Si substrate by using a standard plasma enhanced chemical vapour deposition (PECVD) technique and is then etched into periodic holes by combining a standard photolithography and a reactive-ion etching (RIE) technique. Subsequently, the (113) Si substrate undergoes an anisotropic and selective wet etching process using a KOH solution, where the areas without any SiO₂ masks are etched away. The wet etching will automatically stop once {111} facets are formed, as it is intrinsically difficult to etch (111) silicon by a KOH solution. Finally, all the residual SiO₂ masks are removed by a buffered HF solution. Figure 4.1(e) presents a top-view SEM image of the patterned (113) Si substrate, where a number of regularly arrayed holes with an inverted-pyramid shape can be clearly observed. The facets in each inverted-pyramid pattern are planes of (111), (1-11), (-1-11) and (-111), labelled as A, B, C and D in Figure 4.1(e), respectively. The angles of facets A, B, C and D with respect to the

(113) surface are 29.50° , 58.52° , 79.98° and 58.52° , among which B and D facets are close to the angle (58.41°) which we require in order to grow (11-22) semi-polar GaN based on Table 4.1. It is therefore conceivable that semi-polar (11-22) GaN would be obtained, if growth initiates from facet B or D.

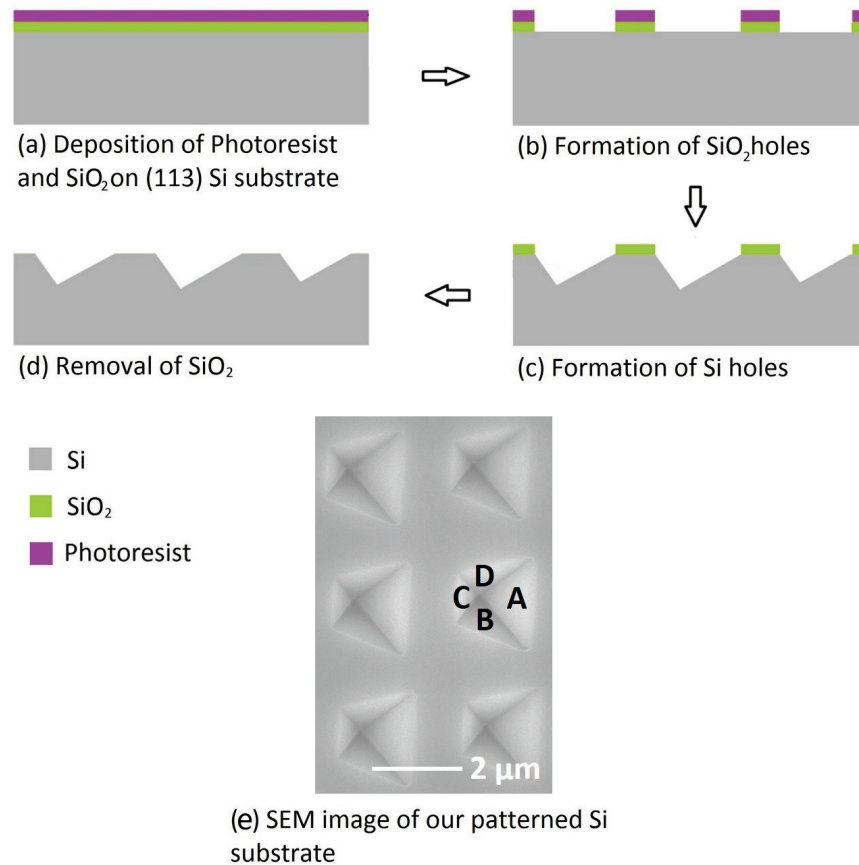


Figure 4.1: (a)-(d) Schematics of the fabrication procedure of patterned (113) Si, (e) top view SEM image of the patterned (113) Si.

4.3.2 Formation of Inverted-pyramid Patterns

This section introduces the details of our Si substrate fabrication procedure to create inverted-pyramid patterns. Initially, a 2-inch (113) Si substrate is cleaned by n-butyl acetate, acetone and IPA consecutively in an ultrasonic bath for 3 min. A 70 nm-thick SiO₂ layer is then deposited by PECVD, followed by a standard photolithography process using a mask consisting of a number of regularly arrayed squares with a size of 2 μm and a gap of 1 μm between squares as shown in Figure 4.2 (a). Figure 4.2 (b) shows the surface of the (113) Si

substrate after the standard photolithography process, where the square array patterns have been transferred onto photoresist spin-coated on the SiO₂ layer on the Si substrate.

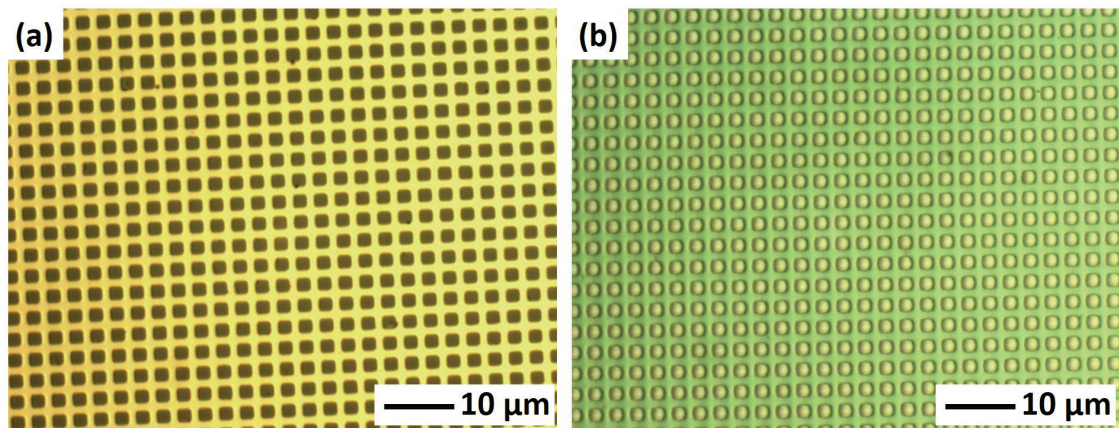


Figure 4.2: Optical microscopy images of (a) the photolithography mask used and (b) photoresist patterns on the SiO₂ on a Si substrate.

The SiO₂ layer is subsequently etched by RIE with a RF power of 90 W and a CHF₃ flow rate of 35 sccm. Finally, the patterned SiO₂ layer on Si substrate has been obtained as shown in Figure 4.3.

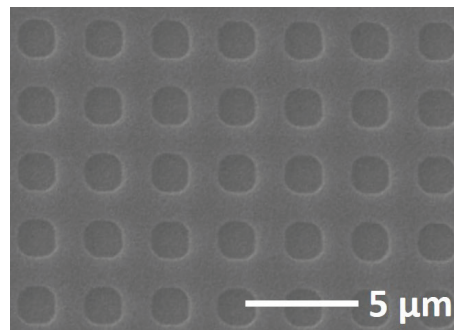


Figure 4.3: Top view SEM image of SiO₂ patterns on a Si substrate.

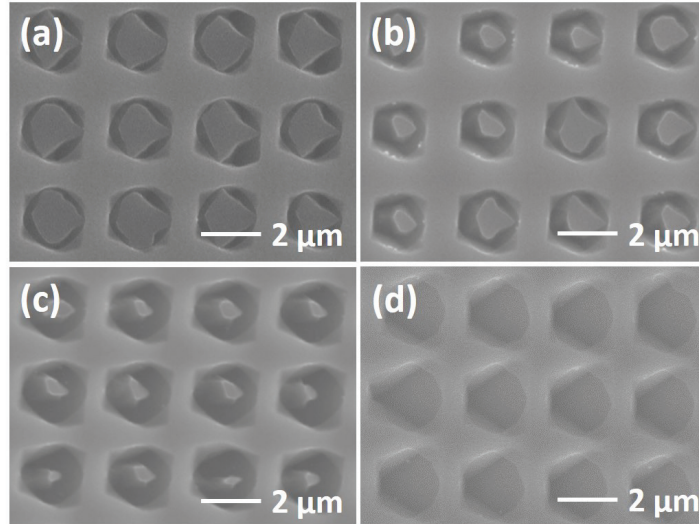
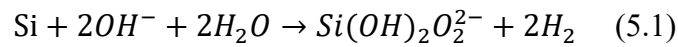


Figure 4.4: Top view SEM images of the substrate after a KOH etching process for (a) 8 min (b) 12 min, (c) 15 min, and (d) 18 min.

The patterned Si substrate further undergoes another wet etching process using a KOH solution (25wt%) at 30°C, following a chemical reaction between Si and KOH as shown below [6].



Si etching in a KOH solution shows anisotropic features, as the bonding energy of Si atoms are different, depending on crystal planes. As $\{111\}$ Si planes are inert to KOH, the wet etching process in a KOH solution will automatically stop once touching the $\{111\}$ Si planes, thus forming inverted-pyramid holes each with four $\{111\}$ Si facets as shown in Figure 4.4. After 18 min KOH etching (our optimised conditions), the regularly arrayed holes each with a perfect inverted-pyramid shape are formed.

After the KOH etching process, the patterned Si substrate is immersed in 10% buffered HF for 10min to remove all the residual SiO_2 masks. As shown in Figure 4.5(a), all the sidewalls of the Si inverted-pyramid patterns are very smooth. Figure 4.5 (b) shows that the formed (1-11) Si facet is 17° offset with respect to the primary flat of the Si substrate (used as our reference line). The wafer primary flat of a (113) Si wafer is typically perpendicular to Si [1-10].

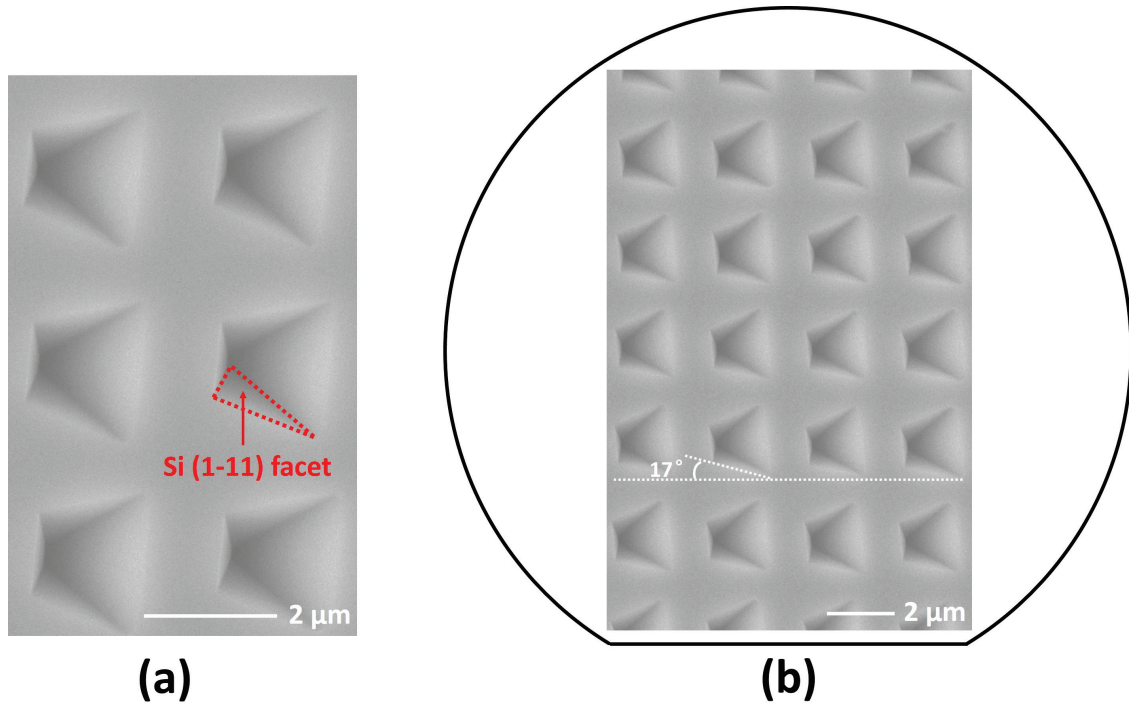


Figure 4.5: Top view SEM images of the patterned Si substrate after HF.

4.3.3 Selective Deposition of SiO₂ Mask

In order to grow GaN only on the (1-11) Si facet on Si substrate, other Si facets of the inverted pyramids and other area of the Si substrate have to be covered by SiO₂. Therefore, a 20 nm SiO₂ layer is selectively deposited on facets A, C, D, leaving only the B facet ((1-11) Si facet) exposed, as shown in Figure 4.1 (e). This can be achieved by simply tilting the patterned Si substrate with a certain angle by using an electron-beam evaporation technique as schematically illustrated in Figure 4.6. The SiO₂ source is loaded in the crucible and bombarded by a focused electron beam.

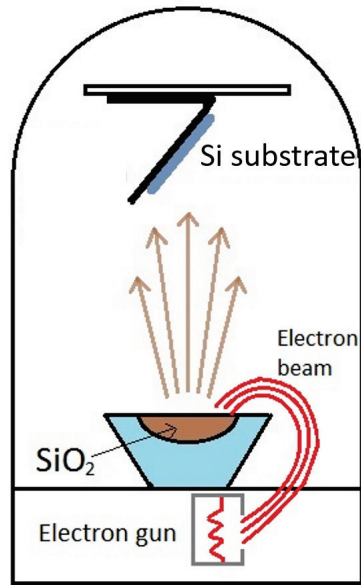


Figure 4.6: Schematic of SiO₂ masks selectively deposited in an electron-beam deposition chamber.

By carefully tuning the oblique angle for the electron-beam deposition, a uniform selective SiO₂ mask is achieved shown in Figure 4.7. The optimised oblique angle is 60°. Only the (1-11) Si facet of the patterned Si substrate is exposed while the other Si facets and the other Si substrate surface areas are covered by SiO₂. Figure 4.8 shows SEM images of the finally patterned silicon substrate across the 2-inch wafer, demonstrating a good uniformity cross the whole wafer in terms of size and shape.

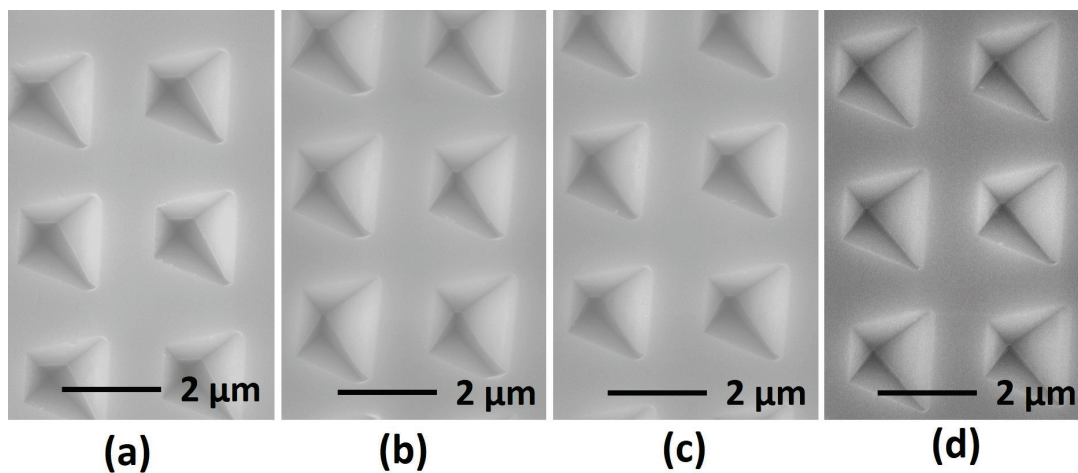


Figure 4.7: Top view SEM images of SiO₂ masks selectively deposited on the patterned Si substrate by (a) 75°, (b) 70°, (c) 65° and (d) 60° oblique angles.

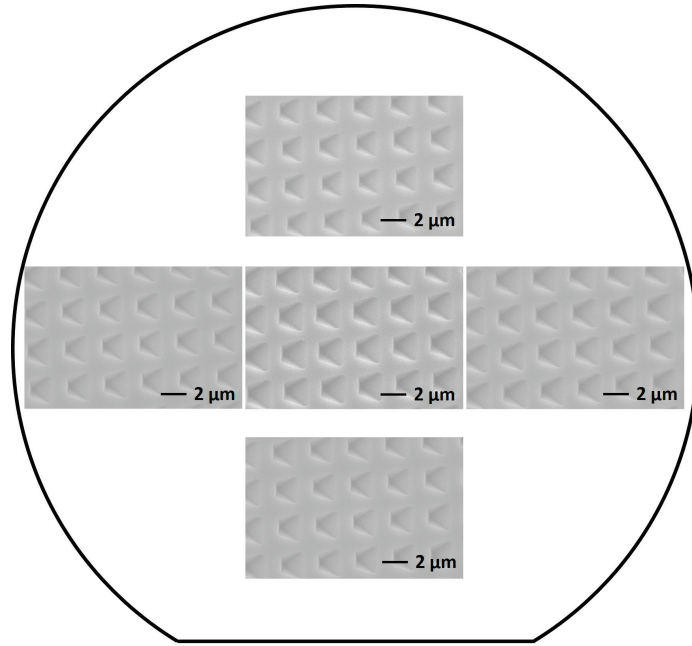


Figure 4.8: Top view SEM images of the patterned Si substrates across a two inch wafer.

4.4 (113) Si Substrates with Stripe Patterns

4.4.1 Methodology

In order to grow semi-polar (20-21) GaN on Si, (-1-11) Si plane in a (113) Si substrate has to be used for the GaN growth. Consequently, we have developed a different patterning process in order to obtain stripe patterns with (-1-11) Si facets.

Figure 4.9 describes the patterning procedure. First, a SiO₂ layer is deposited on a (113) Si substrate by PECVD. Second, a standard photolithography process is performed to form photoresist stripes on SiO₂. Next, a Ni layer is deposited using a thermal evaporator. After a lift-off process, Ni stripes are formed, and then the Si substrate is etched into stripes by RIE and inductive coupled plasma (ICP) using the Ni stripes as etching masks. Finally, the Ni is removed and the Si substrate is anisotropically etched in a KOH solution, creating the Si facets for subsequent GaN growth. Figure 4.9(g) shows the cross sectional SEM image of the final (113) Si substrate with stripe patterns, where the facets in the Si stripe are Si (-1-11), (11-1) and (111) planes, labelled as A, B and C, respectively. The angles of facets A, B and C with respect to the surface are 79.98°, 100.02° and 29.50°, respectively. Therefore, semi-polar (20-21) GaN with a 4.89° offset angle can be obtained when subsequent GaN growth takes place on facet A.

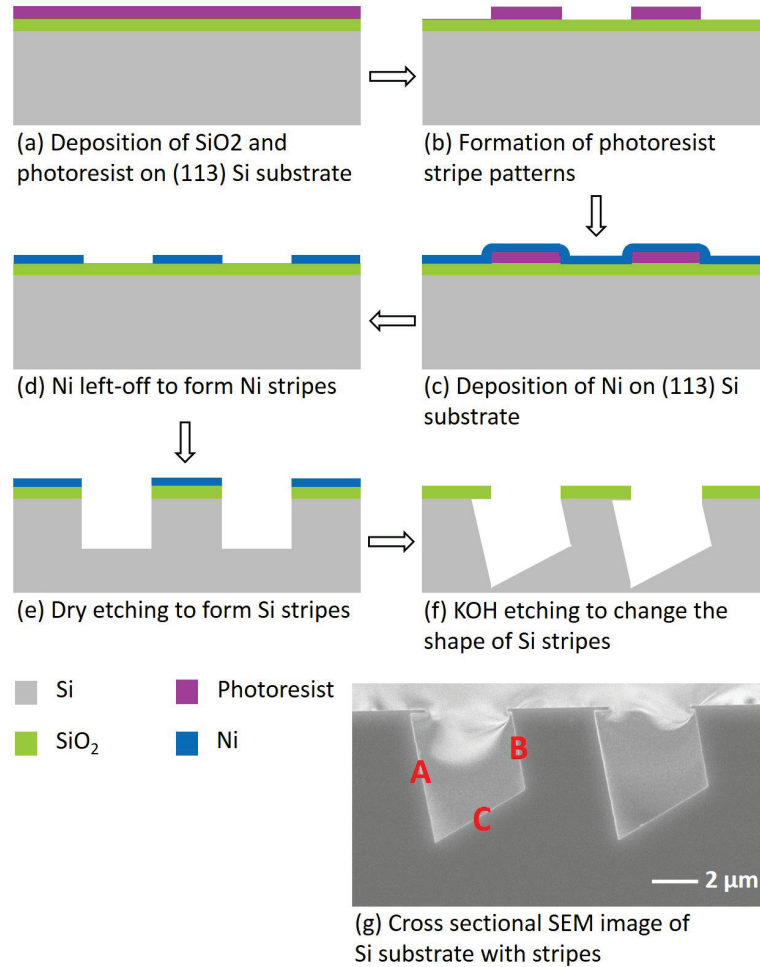


Figure 4.9: (a)-(f) Schematics of the fabrication procedure of the stripe patterned (113) Si, (g) cross sectional SEM image of the stripe-patterned (113) Si.

4.4.2 Formation of Stripe Patterns

After an initial cleaning process as detailed in section 4.3.2, a 120 nm thick SiO₂ layer is deposited on a (113) Si substrate by PECVD. Next, a standard photolithography process is performed. A photolithography mask with stripe patterns is shown in Figure 4.10 (a), where a 4 μm stripe with a 4 μm gap between stripes is used. Figure 4.10 (b) shows the surface of the (113) Si substrate after the photolithography process, where the stripe patterns have been transferred to the photoresist deposited on the SiO₂ layer.

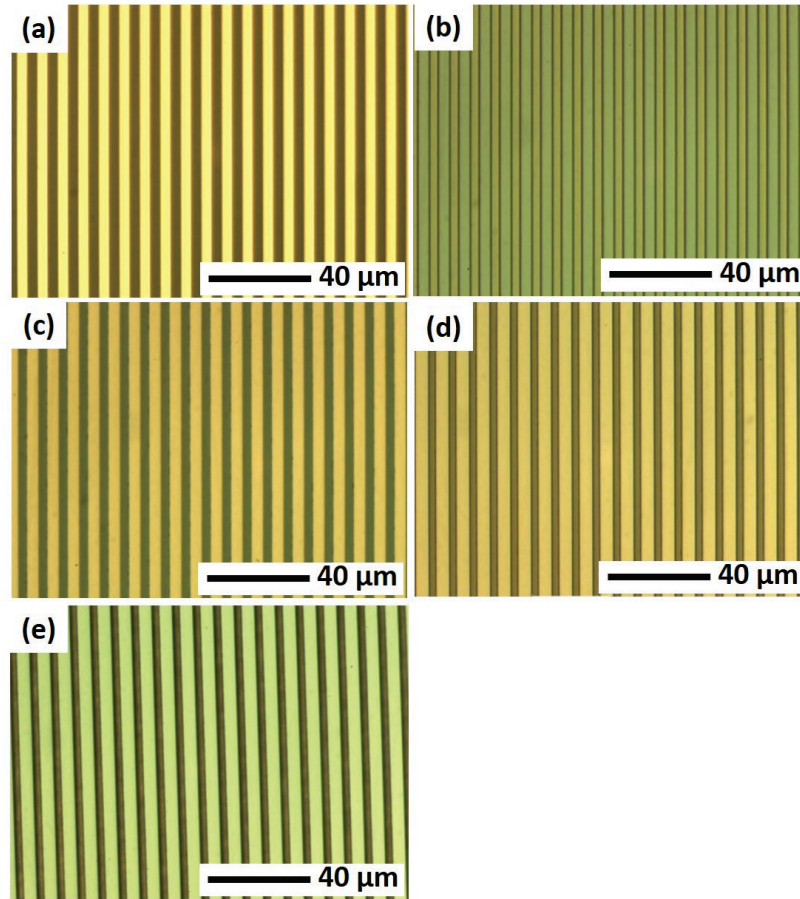


Figure 4.10: Optical microscopy images of the photolithography mask used (a); Optical images of the (113) Si substrate (b) after the photolithography process, (c) after the Ni lift-off process, (d) after the RIE etching process and (e) after the ICP etching process.

Since the photoresist stripes as masks cannot stand for long time during a subsequent Si dry etching process, a metal mask on the top of SiO₂ is further needed, which can be achieved by a standard photolithography technique. Figure 4.10 (c) shows that the Ni stripes are on the SiO₂. Subsequently, using the Ni stripes as masks, the SiO₂ layer is etched by RIE with the condition of a RF power of 90 W and a CHF₃ flow rate of 35 sccm, as shown in Figure 4.10(d). Further using an ICP dry-etching technique, the Si stripes have been formed (Figure 4.10(e)). For the ICP etching, 40 sccm SF₆, 2sccm Ar₂ and 10sccm O₂ are used with an ICP power of 750 W. The Ni is finally removed by nitric acid. Figure 4.10 (e) shows the stripe patterns finally fabricated, demonstrating a good shape and uniformity.

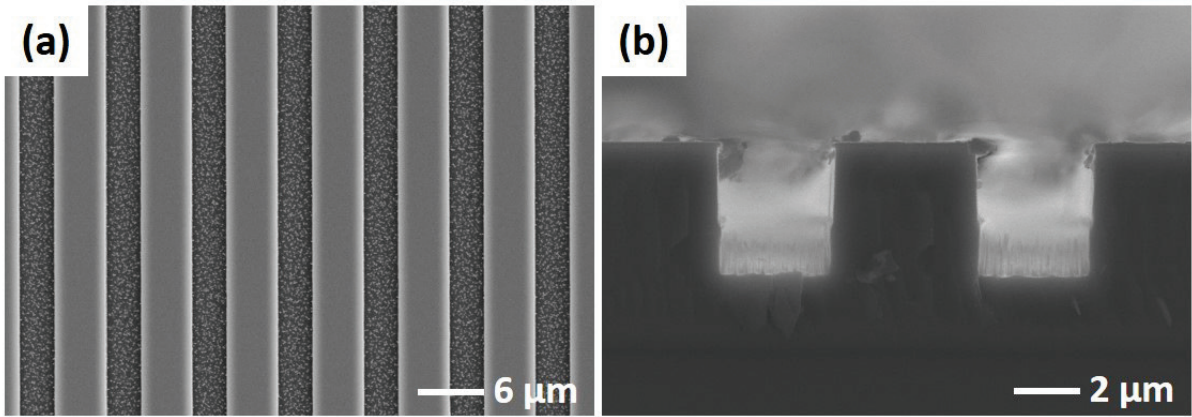


Figure 4.11: (a) Top view and (b) cross-sectional SEM images of the patterned Si substrate after removing Ni mask.

Figures 4.11 (a) and (b) show the plan-view and cross-sectional SEM images of the final silicon stripes, respectively.

Similarly, the (113) Si substrate undergoes an anisotropic etching process by a KOH solution as detailed in section 4.3.2. Figure 4.12 show the SEM images of the patterned silicon as a function of KOH etching time of up to 20 mins, demonstrating the Si stripes with three smooth Si facets formed, namely (-1-11), (11-1) and (111) Si planes.

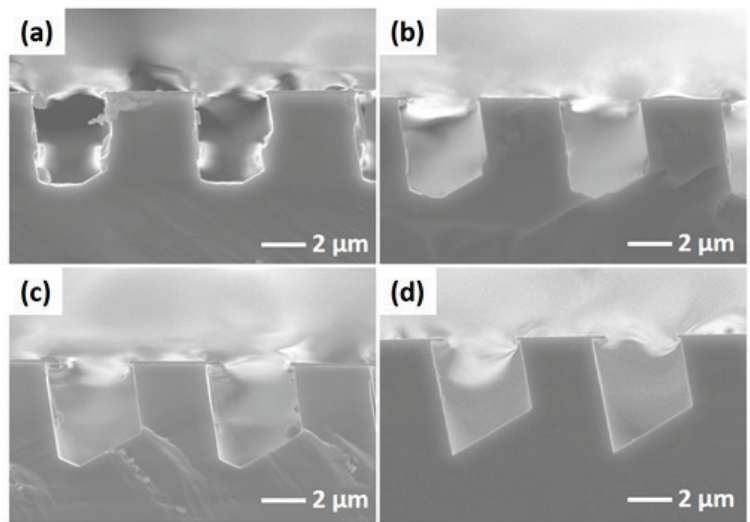


Figure 4.12: Cross sectional SEM images of a Si substrate after a KOH etching process for (a) 8 min (b) 12 min, (c) 16 min, and (d) 20 min.

4.5 Summary

In summary, two kinds of patterned Si substrates have been successfully fabricated based on a combination of a UV photolithography technique, dry etching processes, an anisotropic wet etching and a selective SiO₂ deposition process. After optimisation of the fabrication procedure, (113) Si substrates with good uniformity of inverted-pyramid patterns and stripe patterns have been achieved, which have been confirmed by detailed SEM measurements, respectively.

References

1. J. Bai, X. Yu, Y. Gong, Y. N. Hou, Y. Zhang, and T. Wang, *Semicond. Sci. Technol.* **30**, 065012 (2015)
2. X. Yu, Y. N. Hou, S. H. Shen, J. Bai, Y. Gong, Y. Zhang, and T. Wang, *Phys. Stat. Sol. (c)* **13**, 190 (2016)
3. N. Suzuki, T. Uchida, T. Tanikawa, T. Hikosaka, Y. Honda, M. Yamaguchi, and N. Sawaki, *J. Cryst. Growth* **311**, 2875 (2009)
4. T. Tanikawa, N. Suzuki, Y. Honda, M. Yamaguchi and N. Sawaki, *Phys. Stat. Sol. (c)* **7**, 1760 (2010)
5. H. H. Liu, H. Y. Lin, C. Z. Liao, and J. I. Chyi, *ECS J. Solid State Sci. Technol.* **2**, N3001 (2013)
6. R. A. Wind, and M. A. Hines, *Surface Science* **460**, 21 (2000)

Chapter 5

Semi-polar (11-22) GaN Grown on Inverted-pyramid Patterned (113) Si

5.1 Growth of GaN on Inverted-pyramid Patterned Si

Semi-polar (11-22) GaN growth was carried out by MOCVD on the (113) Si substrates with inverted-pyramid patterns obtained in Chapter 4. Figure 5.1 (a) shows the cross sectional SEM image of the GaN grown on patterned Si, cleaved along the (10-10) plane. The GaN growth starts on the (1-11) Si facet (i.e., B facet as shown in Figure 5.1(b)) which has a 58.5° tilt with respect to the vertical direction. As shown in Figure 5.1 (a), the interface between the GaN film and the (1-11) Si facet is free of voids. Instead, voids are observed above the patterned Si surface. It implies that the growth nucleates on the (1-11) Si facet and advances along the c-axis [1]. When GaN growth is above the surface of the patterned Si, the growth extends laterally until the film coalesces. The whole GaN growth process is schematically shown in Figure 5.1 (c).

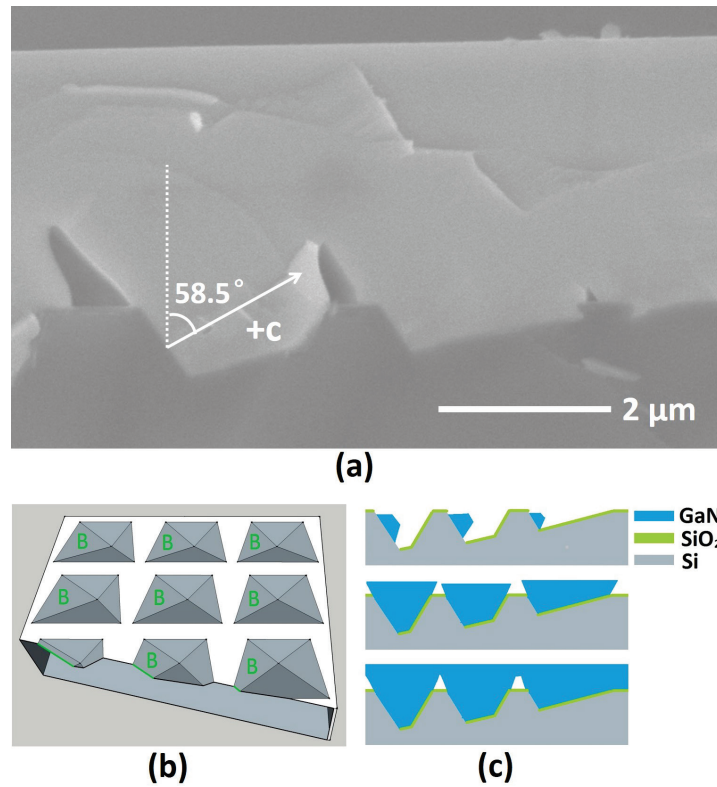


Figure 5.1: (a) Cross sectional SEM image of the GaN on the patterned Si; schematics of (b) (113) patterned, (c) semi-polar GaN growth process on the patterned Si.

The influence of GaN growth conditions on the GaN surface morphology has been studied. A standard MOVPE growth recipe of GaN on silicon is used. Firstly, the patterned (113) Si substrate is thermally annealed at 1110 °C in H₂ ambient for 5 min to remove any natural oxides of the silicon substrate [2]. Subsequently, a 100 nm AlN buffer layer is grown at 1180 °C with a NH₃ flow rate of 90 sccm and a flow rate of TMA of 120 sccm TMA under 65 torr, our optimized conditions for the GaN growth on planar (111) Si. The AlN layer also separates any subsequently grown GaN from the Si substrate in order to avoid any melt-back etching issue [3]. Table 5.1 provides a number of growth parameters for the GaN growth used for optimisation. The GaN growth time for all the samples is fixed to be 5000 sec, and the GaN layer thickness is around 3 μm.

Condition	P (Torr)	T (°C)	NH ₃ /TMG (sccm)	V/III ratio
I	225	1125	5840/65	1720
II	300	1125	5840/65	1720
III	300	1125	2920/65	860
IV	300	1125	2400/65	707
V	300	1125	1900/65	560
VI	300	1125	1600/65	471
VII	300	1110	2400/65	707

Table 5.1: Growth conditions of semi-polar (11-22) GaN.

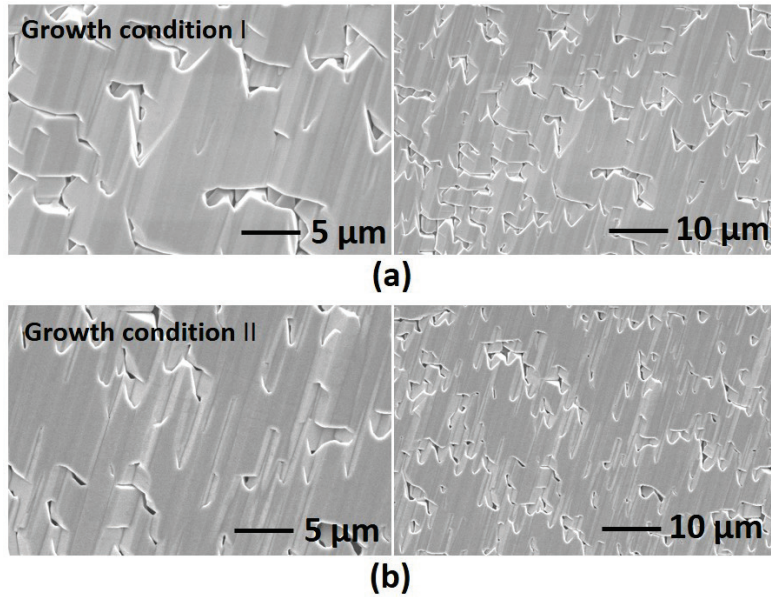


Figure 5.2: Top view SEM images of the (11-22) GaN film grown under growth condition (a) I and (b) II.

The influence of growth pressure on surface morphology has been investigated by detailed SEM measurements, as shown in Figure 5.2. Clearly, a better coalescence can be observed at a relatively higher pressure (300 Torr vs. 225 Torr) in spite of the ‘V’-shape gaps formed due to a limited lateral growth rate particularly along [10-10] direction [4].

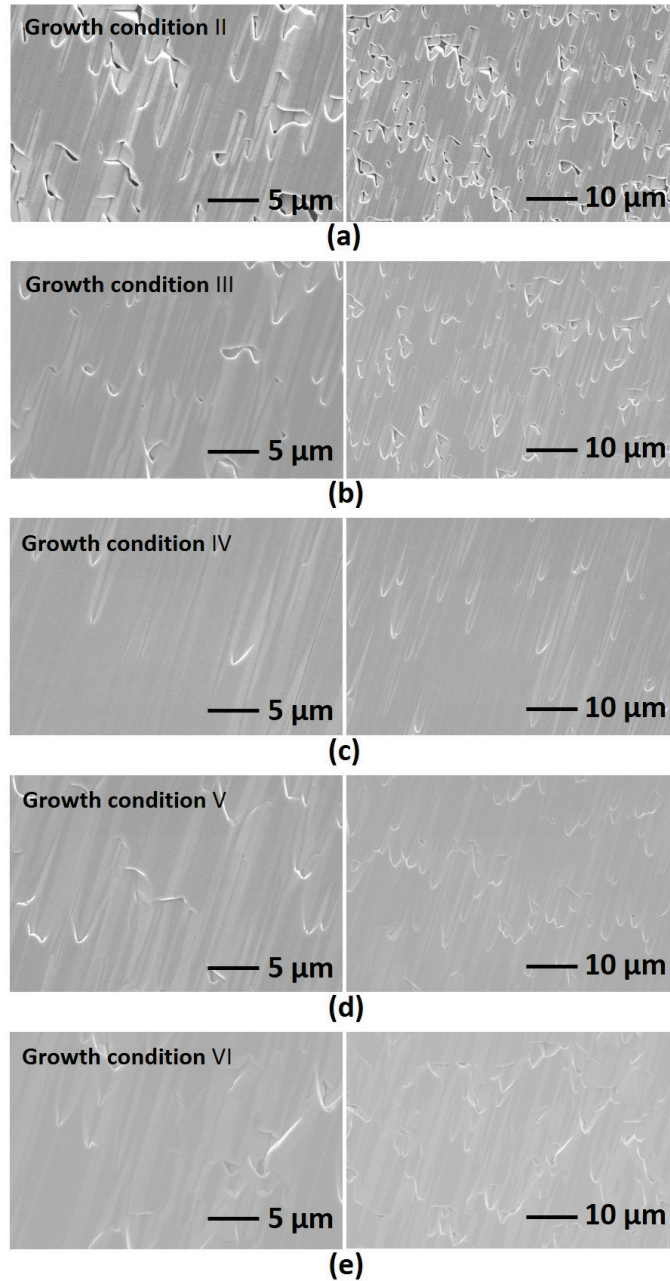


Figure 5.3: Top view SEM images of the (11-22) GaN grown under growth condition (a) II, (b) III, (c) IV, (d) V, and (e) VI.

In order to enhance the lateral growth rate to achieve a full coalescence, the influence of V/III ratio on surface morphology has also been investigated. Figure 5.3 exhibits the sample surface grown under different V/III ratios ranging from 1730 down to 470 (conditions II-VI in Table 5.1). It is found that the ‘V’-shape gaps disappear with a reduced V/III ratio of 707, but reproduces if it is too low, which is likely to introduce a strong anisotropic Ga adatoms diffusion length [5-7]. The best GaN surface has been obtained under the growth condition IV

described in Table 5.1, where the optimised V/III ratio is 707. Furthermore, the influence of growth temperature on the surface morphology has also been investigated, confirmed by the SEM images as shown in Figure 5.4. The optimised growth temperature is between 1125 °C and 1110 °C.

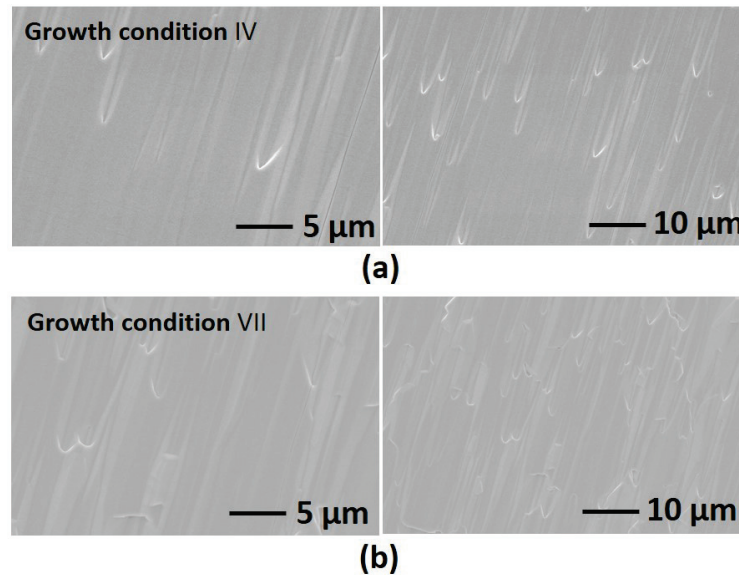


Figure 5.4: Top view SEM images of the (11-22) GaN film grown under growth condition (a) IV and (b) VII.

Compared with semi-polar GaN on a stripe patterned Si substrate reported by other groups [8], our sample is almost crack-free across a 2-inch GaN wafer even though the GaN thickness is ~ 3 μm . With the inverted-pyramid patterns on the Si substrate, the thermal stress between GaN and Si can be effectively relaxed as a result of the small and non-continuous GaN selective growth area and the formation of voids during the GaN [9].

5.2 Structural and Optical Characterizations

In order to confirm the (112-2) crystal orientation of our semi-polar GaN grown on the special patterned substrates, HD-XRD measurements have been carried out. Figure 5.5 shows XRD data obtained in a 2θ - ω scan mode. Only sharp diffraction peaks from the (11-22) GaN and (113) Si can be observed, indicating that a single phase semi-polar (11-22) GaN has been obtained.

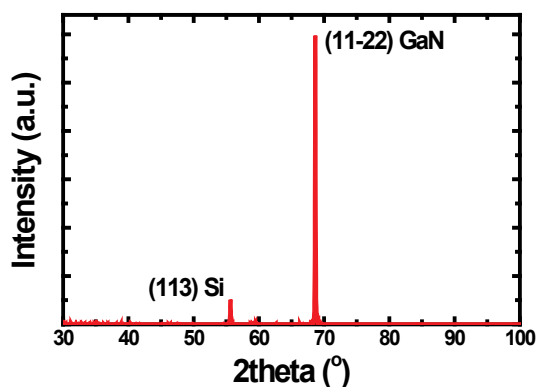


Figure 5.5: XRD 2θ - ω scan profile of the symmetric (11-22) GaN plane on our patterned Si.

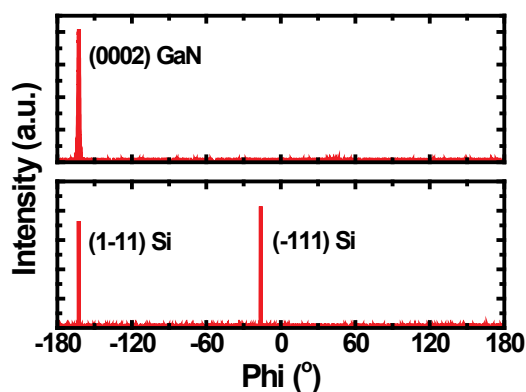


Figure 5.6: XRD phi-scan profiles of the asymmetric (0002) GaN plane and the (1-11)/(-111) Si planes.

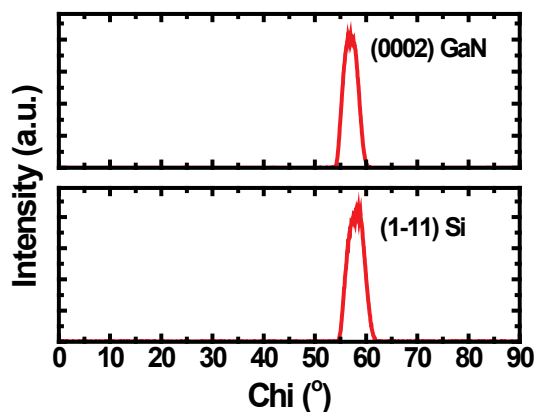


Figure 5.7: XRD chi-scan profiles of the asymmetric (0002) GaN plane and the (1-11) Si plane.

Further investigation of the GaN in-plane crystal orientation has been performed by a phi-scan measurement and a chi-scan measurement of an asymmetric GaN (0002) plane on our semi-polar (11-22) GaN. As shown in Figure 5.6, only a single (0002) GaN peak is observed at a phi angle of -163° agreeing with the phi position of (1-11) Si. It means that the GaN growth along an inclined c-direction with respect to the substrate starts only on the (1-11) Si facet. At

the phi angle of -163° , a chi-scan measurement shown in Figure 5.7 indicates that the (0002) GaN plane is inclined by 58° to the sample surface, which is the same angle as the inclination angle of the (1-11) Si facet with respect to the surface. This further confirms that the GaN growth starts only on the (1-11) Si facets as expected.

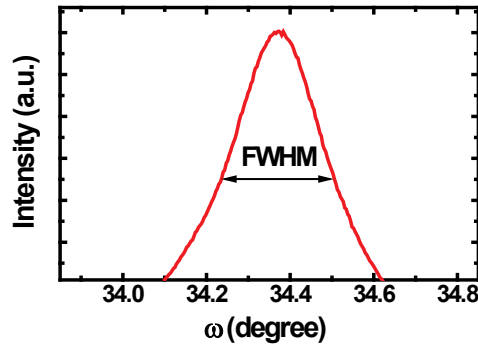


Figure 5.8: XRD ω -rocking curve of the (11-22) GaN.

The crystal quality of the (11-22) GaN has been investigated by XRD rocking curve measurements. Figure 5.8 shows the XRD rocking curves measured along the on-axis (11-22), showing a FWHM of 0.2708° , where the incident X-ray beam is parallel to GaN [10-10]. Figure 5.9 shows the FWHMs of the XRD rocking curves as a function of an azimuth angle (i.e., phi angle). At the 17° azimuth angle, the incident x-ray is along GaN [10-10], while the x-ray is along GaN [11-23] at the 107° azimuth angle. For comparison, Figure 5.9 shows the FWHM of the XRD rocking curves of a typical (11-22) GaN directly grown on m-plane sapphire [10-12]. The FWHMs of the XRD rocking curves of the (11-22) GaN grown on m-plane sapphire are generally larger than those of the (11-22) GaN grown on our special patterned Si, indicating that the GaN on our patterned Si has a better crystal quality.

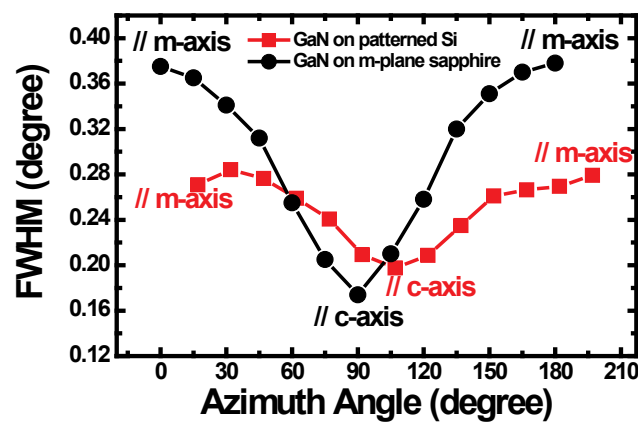


Figure 5.9: FWHMs of the on-axis XRD rocking curve of (11-22) GaN as a function of an azimuth angle.

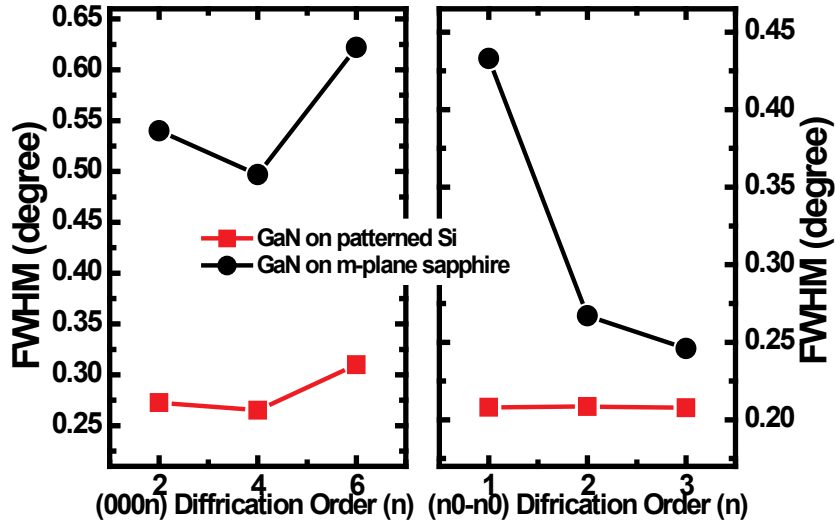


Figure 5.10: FWHMs of the off-axis XRD rocking curves of (000n) and (n0-n0) planes.

XRD rocking curve measurements performed along (000n) and (n0-n0) off-axis have also been carried out to further prove the good crystal quality of the GaN on our patterned Si, as shown in Figure 5.10. Generally speaking, the broadening of a XRD rocking curve measured along an off-axis (000n) plane is mainly due to dislocations with a Burgers vector which has a c-axis component, while a XRD rocking curve measured along an off-axis (n0-n0) plane is broadened due to BSFs [7, 13]. Figure 5.10 shows that the FWHM of the XRD rocking curve measured from both the off-axis (000n) and (n0-n0) planes are narrower for the GaN grown on our patterned Si than those for a standard GaN layer directly grown on m-plane sapphire, further conforming the better crystal quality of the (11-22) GaN grown on our patterned Si.

The optical properties of the GaN have been characterized by PL measurements using a 325 nm He-Cd laser as an excitation source. Figure 5.11 shows its PL spectrum measured at 10K. For comparison, Figure 5.11 also shows the spectra of a standard (11-22) GaN layer directly grown on m-plane sapphire and a standard GaN layer on (0001) sapphire, which were grown under normal conditions with a GaN thickness of 1.4 and 1.1 μm , respectively. The (11-22) GaN on our patterned Si shows very strong band-edge emission at 357nm. A very weak emission peak at 365nm is ascribed to the luminescence of excitons bound to BSFs [14, 15]. For the standard (11-22) GaN grown on sapphire, the spectrum is dominated by BSF-related emission at 363 nm, and another one around 376 nm which arises from prismatic SFs (PSF) and partial dislocations [14-18]. The BSF density can be roughly assessed from PL spectra by evaluating the intensity ratio between the band edge and BSF emission. The intensity ratio is 20

for the semi-polar GaN on patterned Si substrates, confirming that the BSF density has been significantly reduced [16-18]. It is worth noting that the intensity of the band-edge emission in semi-polar GaN on Si is comparable to that of c-plane GaN on sapphire. The red shift in the band edge emission for (11-22) GaN on Si compared to GaN on sapphire may be ascribed to the tensile strain induced by the large differences of lattice constant and thermal expansion coefficient between GaN and Si [19].

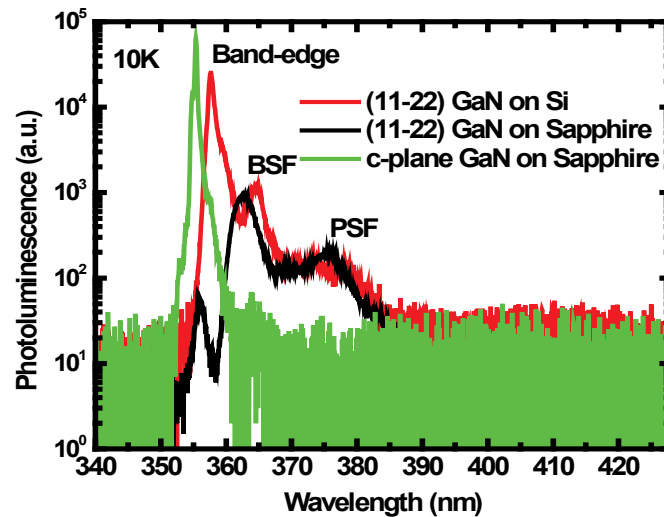


Figure 5.11: PL spectra of the (11-22) semi-polar GaN grown on our patterned (113) Si, a standard (11-22) semi-polar GaN on m-plane sapphire and a standard GaN on c-plane sapphire, all measured at 10 K.

Figure 5.12 shows the PL spectra measured at room temperature (300K). The (11-22) GaN on our patterned Si shows a very strong band-edge emission; whereas the band-edge emission from the standard (11-22) GaN on m-plane sapphire nearly disappears. For the PL spectra of the (11-22) GaN on patterned Si, a fitting using multiple Lorentzian curves was performed. The intensity ratio between the band-edge and BSF-related emissions is around 5. This further proves the much better crystal quality of the (11-22) GaN grown on our patterned Si.

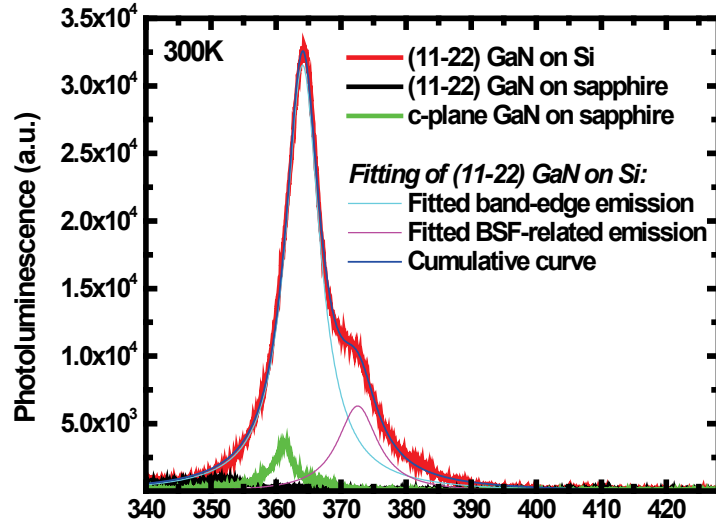


Figure 5.12: PL spectra of the (11-22) semi-polar GaN grown on our patterned (113) Si, a standard (11-22) semi-polar GaN on *m*-plane sapphire and a standards GaN on *c*-plane sapphire, all measured at room temperature.

Moreover, the temperature-dependent PL measurements have been performed as shown in Figure 5.13. The peak energies as a function of temperature are plotted in Figure 5.14. When temperature increases, the band-edge emission red-shifts due to temperature induced band-gap shrinkage [20]. In contrast, BSF-related emission exhibits a non-monotonic dependence on temperature, with a red-shift first, then a blue-shift, and a final red-shift above 100K. Such an S-shape behaviour is typical for the emission arising from localized carriers. As the BSF in GaN is a very thin zinc-blende (ZB) layer embedded in the wurtzite (W) matrix, the large conduction band offset at ZB/W interfaces implies that BSFs can be regarded as quantum-well-like regions [21]. Therefore, the S-shape behaviour of BSF-related emission is ascribed to the exciton deeply localized in this region. It is found that the PL spectrum for (11-22) GaN on Si is dominated by the band-edge emission across the temperature range.

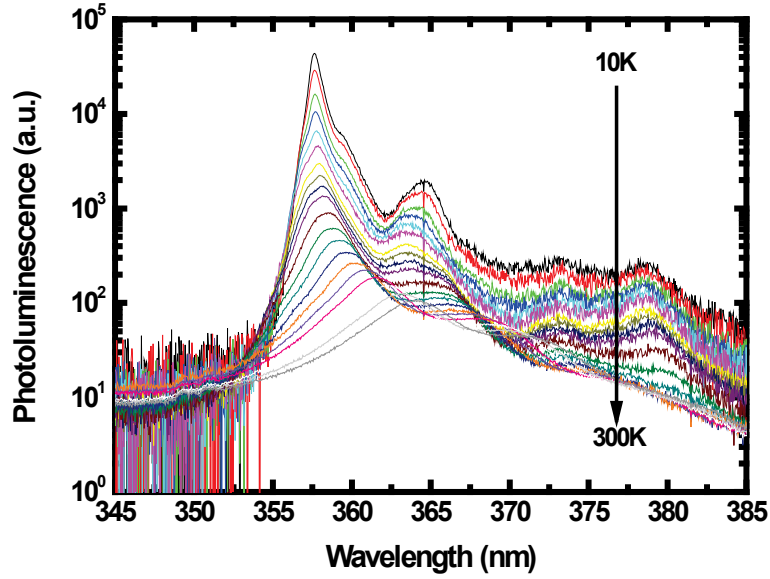


Figure 5.13: PL spectra of the (11-22) GaN grown on our patterned (113) Si, measured at a temperature ranging from 10 to 300K.

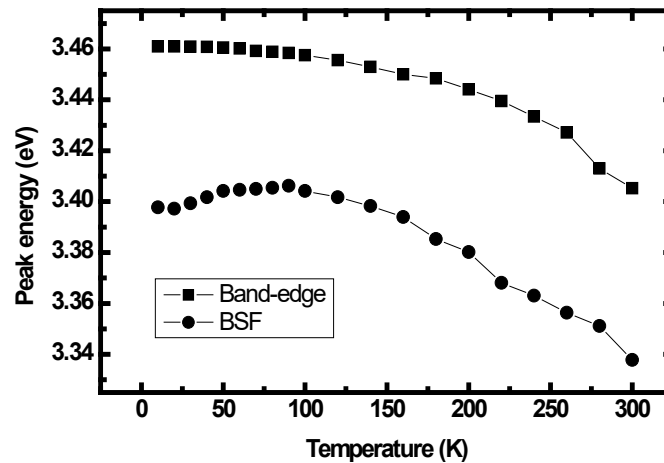


Figure 5.14: Emission peak energies as a function of temperature.

5.3 Mechanism of Defect Reduction in GaN

Detailed TEM measurements have been performed to study the microstructure of the (11-22) GaN grown on our patterned silicon, in particular, the mechanism of defect reduction. Figure 5.15 shows a cross-sectional TEM image of the semi-polar GaN with $\mathbf{g}=11\bar{2}2$, where nearly all the dislocations in GaN can be observed [22]. Four consecutive cross sections of Si inverted-pyramid patterns can be seen clearly but with different profiles, which has been visualized by schematics in Figure 5.1. For the Si inverted-pyramid patterns 1 and 4 in Figure

5.15, the intersection positions between the cleavage face and Si patterns are further from the pattern centres than those for patterns 2 and 3. One set of (1-11) Si facets with an inclined angle of 58° can be seen on the left side of each pattern (labelled 'B'). The defects in the lower GaN layer mainly aggregate close to the Si facet 'B', where GaN starts to grow.

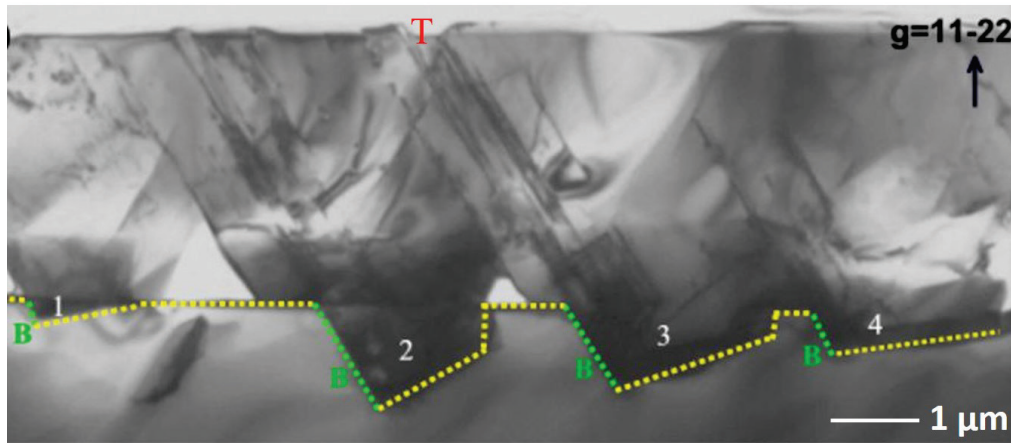


Figure 5.15: Cross sectional TEM image of the semi-polar GaN on our patterned Si taken around $[1-100]$ zone-axis with $g=11-22$.

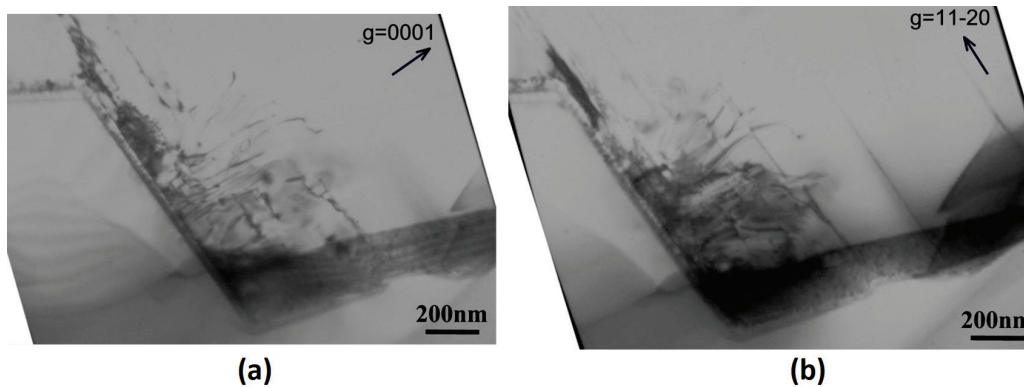


Figure 5.16: Cross sectional TEM images of the semi-polar GaN on our patterned Si, taken around $[1-100]$ zone-axis with (a) $g=0002$ and (b) $g=11-20$.

Figure 5.16 shows the cross-sectional TEM images with $g=0002$ and $g=11-20$ at a higher magnification to investigate the defect structure in the Si pattern in detail. Near the interface within the distance $h < 100$ nm along GaN c-direction, a high disorder of defects nucleated from the interface due to the large lattice mismatch between AlN and Si, mostly composed of dislocations and stacking faults. For a middle range from the interface ($100\text{nm} < h < 0.5 \mu\text{m}$), there is a strong interaction between the defects in this region, leading to a significantly reduced defect density. With increasing film thickness, the dislocations further decrease most likely due

5.18 (a), the dislocations in the upper GaN are mostly lying on c-planes, and many disappear halfway during propagating, very likely due to line bending within c-planes. Based on our group's previous studies on non-polar GaN, the dislocation bending is observed only in the [0001]-axis cross sectional view but never in the [1-100]-axis cross-sectional view [11]. It has also been reported [25] that the GaN overgrown from $\langle 0001 \rangle$ -oriented stripes has a lower dislocation density compared to those on other direction-oriented stripes. This implies that the dislocations change their line direction easily within basal planes. Similarly in this case, the dislocation bending has been observed only within c-planes in Figure 5.18 (b), viewed perpendicular to the [1-100] direction. Many dislocations redirect from the original growth direction to propagate towards the void. This can be ascribed to that, when the isolated GaN islands above the windows started to extend laterally and coalesce with each other, the interaction between the dislocations and the GaN facets causes the dislocations to bend. As a result, the dislocation density is further reduced during GaN islands extending along the $\langle 1-100 \rangle$ direction.

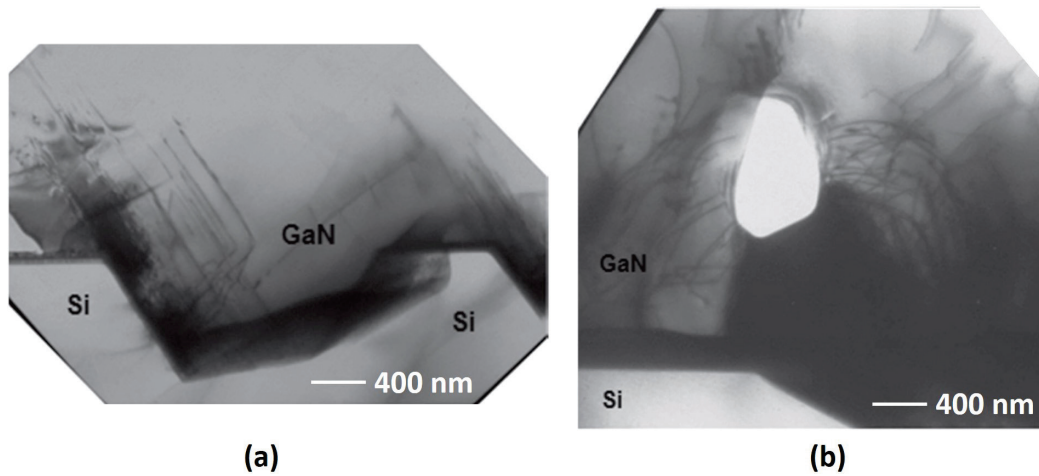


Figure 5.18: Cross sectional TEM images of the semi-polar GaN on our patterned Si: (a) taken along [1-100] zone-axis; (b) taken perpendicular to [1-100] zone-axis.

To clearly display the distribution of SFs and dislocations in the semi-polar GaN surface, plan-view TEM measurements were performed, shown in Figure 5.19. Within an area of $3.5 \times 4.5 \mu\text{m}^2$, BSFs exist in the form of two bunches with a density of $1 \times 10^4 \text{ cm}^{-1}$. The two bunches of BSFs are spaced with a mask period of $\sim 3 \mu\text{m}$, which are generated from the interface in one side of each Si pattern and are impeded by the +c direction growth at the early stage. On the other hand, the dislocations mainly aggregate in a region around one side of BSFs,

corresponding to the region with ‘T’ in Figure 5.15. In Figure 5.19, few dislocations are observed far from the dislocation-rich region. It agrees with the demonstration in Figure 5.15 that dislocations in the upper layer above patterns 1 and 4 are indeed fewer than those above patterns 2 and 3. The intersection positions between the TEM specimen cleavage and patterns for patterns 1 and 4 are further from the pattern centres compared with patterns 2 and 3. This has been ascribed to the dislocation bending and annihilation along both the $[0001]$ and $\langle 1-100 \rangle$ directions. It is worth mentioning that the $\{1-100\}$ facets of GaN islands causing the dislocation bending at the later stage are not available in the case of growth on the $\langle 1-100 \rangle$ -oriented striped substrates.

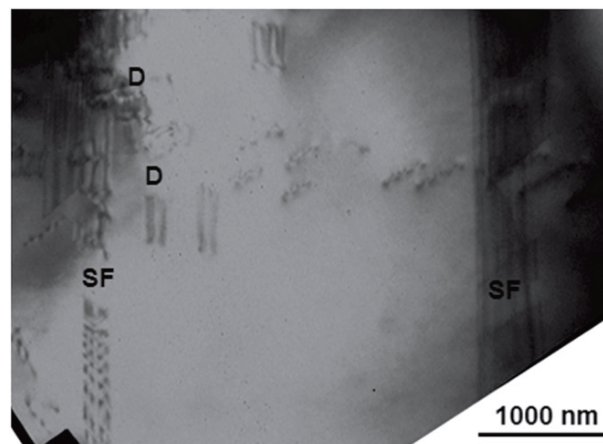


Figure 5.19: Plan view TEM image of the semi-polar GaN on our patterned Si. ‘SF’ and ‘D’ represent stacking faults and dislocations, respectively.

5.4 Conclusion

In summary, semi-polar (11-22) GaN films have been successfully grown on specially designed (113) Si substrates featured with inverted-pyramid patterns. Unlike any other (113) Si mask patterning approaches which lead to grooves with undercut geometry, this specially designed patterning approach produces patterned Si substrates with an ‘open’ configuration, which enables a selective deposition of SiO_2 prior to GaN growth. Therefore, the ‘Ga-melting back’ issue has been suppressed. A smooth GaN surface has been obtained after investigating the influence of GaN growth conditions. With the inverted-pyramid patterns on the Si substrate, the thermal stress between GaN and Si has been effectively relaxed as a result of the small and non-continuous GaN selective growth area and the formation of voids during the GaN growth.

Compared with semi-polar GaN on a stripe patterned Si substrate, our sample is almost crack-free across a 2-inch GaN wafer even though the layer is as thick as 3 μm . The GaN film demonstrates a high quality single crystal with a low density of dislocations and a low density of BSFs confirmed by XRD and PL characterisations. The FWHMs of the XRD rocking curves measured along the on-axis (11-22) GaN are between 0.284° and 0.198° , and the FWHMs of the XRD rocking curves measured along the off-axis (000n) and (n0-n0) plane are all below 0.31° . These FWHMs of the XRD rocking curves are much smaller than those of the (11-22) GaN grown on m-plane sapphire, indicating that the GaN on our patterned Si has a good crystal quality. The low temperature PL spectrum show that the intensity ratio of the band edge emission to and the BSF related emission is as high as 20, indicating a significantly reduced BSF density. The mechanisms of both BSF and dislocation reduction have been discussed based on TEM measurements.

References

1. X. Yu, Y. N. Hou, S. H. Shen, J. Bai, Y. Gong, Y. Zhang, and T. Wang, *Phys. Stat. Sol. (c)* **13**, 190 (2016)
2. C. Mo, W. Fang, Y. Pu, H. Liu, and F. Jiang, *J. Cryst. Growth* **285**, 312 (2005)
3. R. Ravash, A. Dadgar, F. Bertram, A. Dempewolf, S. Metzner, T. Hempel, J. Christen, and A. Krost, *J. Cryst. Growth* **370**, 288 (2013)
4. B. Leung, Q. Sun, C. D. Yerino, J. Han, and M. E. Coltrin, *Semicond. Sci. Technol.* **27**, 024005 (2012)
5. D. S. Oh, J. J. Jang, O. Nam, K. M. Song, and S. N. Lee, *J. Cryst. Growth* **326**, 33 (2011)
6. S. Ploch, T. Wernicke, D. V. Dinh, M. Pristovsek, and M. Kneissl, *J. Appl. Phys* **111**, 033526 (2012)
7. J. Jeong, J. Jang, J. Hwang, C. Jung, J. Kim, K. Lee, H. Lim, and O. Nam, *J. Cryst. Growth* **370**, 114 (2013)
8. H. H. Liu, H. Y. Lin, C. Z. Liao, and J. I. Chyi, *ECS J. Solid State Sci. Technol.* **2**, N3001 (2013)
9. J. Liang, S.-K. Hong, N. Kouklin, R. Beresford, and J. M. Xu, *Appl. Phys. Lett.* **83**, 1752 (2003)
10. J. Bai, Y. Gong, K. Xing, X. Yu, and T. Wang, *Appl. Phys. Lett.* **102**, 101906 (2013)
11. T. J. Baker, B. A. Haskell, F. Wu, J. S. Speck, and S. Nakamura, *Jpn. J. Appl. Phys.* **45**, L154 (2006)
12. M. A. Moram, C. F. Johnston, M. J. Kappers, and C. J. Humphreys, *J. Cryst. Growth* **311**, 3239 (2009)
13. Q. Sun, B. Leung, C. D. Yerino, Y. Zhang, and J. Han, *Appl. Phys. Lett.* **95**, 231904 (2009)
14. R. Liu, A. Bell, F. A. Ponce, C. Q. Chen, J. W. Yang, and M. A. Khan, *Appl. Phys. Lett.* **86**, 021908 (2005)
15. P. P. Paskov, R. Schifano, B. Monemar, T. Paskova, S. Figge, and D. Hommel, *J. Appl. Phys.* **98**, 093519 (2005)
16. T. Wernicke, C. Netzel, M. Weyers, and M. Kneissl, *Phys. Stat. Sol. (c)* **6**, 1815 (2008)
17. J. Jang, K. Lee, J. Hwang, J. Jung, S. Lee, K. Lee, B. Kong, H. Cho, and O. Nam, *J. Cryst. Growth* **361**, 166 (2012)

18. N. Okada, and K. Tadatomo, *Semicond. Sci. Technol.* **27**, 024003 (2012)
19. L. Lee, K. F. Chien, W. C. Chou, C. H. Ko, C. H. Wu, Y. R. Lin, C. T. Wan, C. H. Wann, C. W. Hsu, Y. F. Chen, and Y. K. Su, *Cryst. Eng. Comm.* **14**, 4486 (2012)
20. J. Bai, X. Yu, Y. Gong, Y. N. Hou, Y. Zhang, and T. Wang, *Semicond. Sci. Technol.* **30**, 065012 (2015)
21. P. P. Paskov, R. Schifano, B. Monemar, T. Paskova, S. Figge, and D. Hommel, *J. Appl. Phys.* **98**, 093519 (2005)
22. Y. A. R. Dasilva, M. P. Chauvat, P. Ruterana, L. Lahourcade, E. Monroy, and G. Nataf, *J. Phys. Condens. Matter* **22**, 355802 (2010)
23. T. Zhu, T. Ding, F. Tang, Y. Han, M. Ali, T. Badcock, M. J. Kappers, A. J. Shields, S. K. Smoukov, and R. A. Oliver, *Cryst. Growth Des.* **16**, 1010 (2016)
24. N. Izyumskaya, F. Zhang, S. Okur, T. Selden, V. Avrutin, Ü. Özgür, S. Metzner, C. Karbaum, F. Bertram, J. Christen, and H. Morkoç, *J. Appl. Phys.* **114**, 113502 (2013)
25. I. Kidoguchi, A. Ishibashi, G. Sugahara, and Y. Ban, *Appl. Phys. Lett.* **76**, 3768 (2000)

Chapter 6

Semi-polar (20-21) GaN Grown on Stripe Patterned (113) Si

6.1 Growth of GaN on Stripe Patterned Si

As discussed in Chapter 4, semi-polar (20-21) GaN can be obtained by means of growth on our specially designed (113) Si substrate featured with stripe patterns. Figure 4.9(g) in Chapter 4 shows that there are three facets, namely (-1-11), (11-1) and (111) plane, on which GaN can be grown. The inclination angles of the (-1-11), (11-1) and (111) facets with respect to the Si (113) surface plane are 79.98° , 100.02° and 29.50° , respectively, where the inclination angle of 79.98° between the (-1-11) facet and the surface is closest to the requirements for obtaining (20-21) semi-polar GaN. Figure 6.1 presents a schematic illustration of two kinds of growth modes in order to achieve (20-21) semi-polar GaN grown on the (-1-11) Si facets of the Si stripes, where the semi-polar (20-21) GaN with an offset angle of 4.89° to the horizontal plane can be obtained. If a (113) Si substrate with a 4.89° miscut angle is adopted for growth to compensate the offset angle, a precise semi-polar (20-21) GaN layer can be achieved.

Figure 6.1 shows that GaN may be grown on both sidewalls of (-1-11) and (11-1) Si facets and also the bottom (111) facet. Since the (11-1) and (-1-11) Si facets are parallel to each other, the GaN grown on (11-1) Si facets has the same crystal orientation as the GaN grown on (-1-11) Si facets, i.e., one growth front is along the c-direction, while another one is along the minus c-direction. This growth process is sketched in Figure 6.1(b). After the GaN arms grown from the two opposite sidewalls coalesce and continue to grow above the Si surface, GaN stripes with an 'M' shaped surface with smooth and parallel sidewalls are then formed. It is worth mentioning that below each M-shape GaN stripe is an air-channel formed as a result of the coalescence process. Such a channel plays an important role in producing a melt-back etching issue, which will be discussed later. The self-formed sidewalls can be used as a good cavity for a LD structure. This is very important for the fabrication of a semi-polar GaN based LD, as it is a great challenge to cleave semi-polar GaN [1].

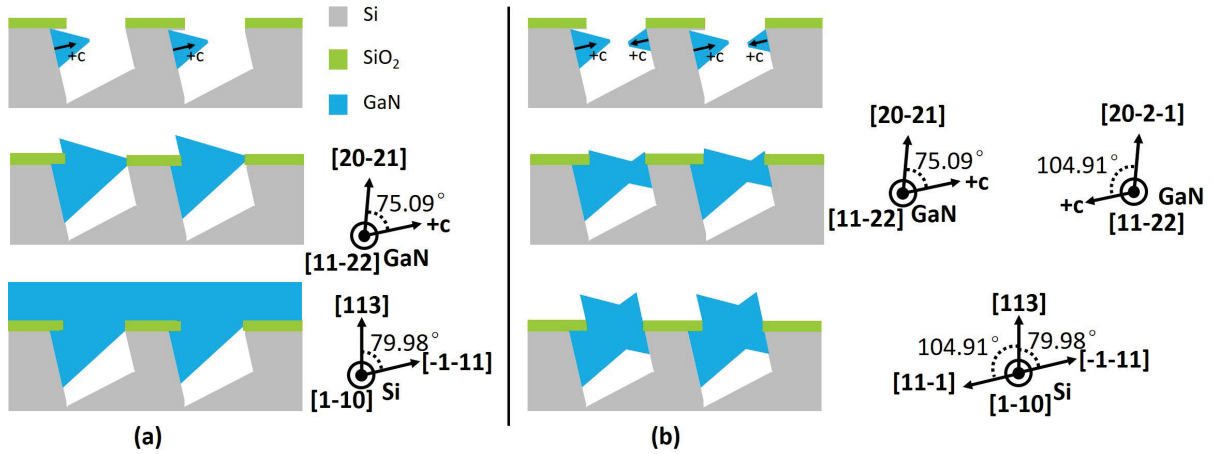


Figure 6.1: Schematics of our semi-polar (20-21) GaN growth process on the stripe patterned (113) Si with (a) one sidewall growth or (b) two sidewalls growth.

GaN could also be grown on the (111) Si facets on the bottom of the trenches, which is eventually stopped once the coalescence of the GaN growth from the two sidewalls occurs. Such growth can be neglected. Finally, (20-21) semi-polar GaN is grown on the stripe-patterned (113) Si substrate. After a standard H₂ annealing process, an AlN buffer layer is grown under the same condition as discussed in Chapter 5.1. The growth conditions are listed in Table 6.1 in order to investigate the influence of growth conditions on crystal quality.

Condition	AlN thickness (nm)	T (°C)	Pressure (Torr)	TMG (sccm)	GaN Growth time (sec)
I	100	1125	300	65	4000
II	100	1075	300	65	4000
III	100	1025	300	65	4000
IV	400	1125	300	65	4000
V	100	1125	600	45	6000

Table 6.1: Growth conditions of GaN on stripe patterned (113) Si.

Figure 6.2 show the top-view SEM images of all the samples grown using the conditions listed in Table 6.1. The growth condition labelled I in the above Table is the same as the optimised condition for the (11-22) GaN growth as discussed in Chapter 5.1. However, strong Ga melt-back etching occurs as shown in Figure 6.2(a). This is attributed to the undercut

configuration of such a Si stripe pattern, since AlN cannot be deposited on the (11-1) Si facet very well as a result of shadow effects. When the growth temperature is reduced down to 1025 °C, the melt-back etching issue can be prevented [2] but GaN starts to be deposited on the SiO₂ layer masks (Figure 6.2 (c)), where a kind of amorphous or poly-crystal GaN is formed. This phenomenon has also been observed when the growth temperature is 1075 °C (Figure 6.2 (b)). These can be understood as: a relatively low growth temperature leads to parasitic growth of GaN on SiO₂ [3]. An increase in growth temperature facilitates Ga atomic diffusion, thus preventing GaN growth on SiO₂. However, it also facilitates GaN decomposition [4], leading to the melt-back etching issue. Therefore, a high temperature (>1075 °) is required in order to avoid the GaN parasitic growth on SiO₂, while the Ga melt-back etching issue needs to be resolved simultaneously.

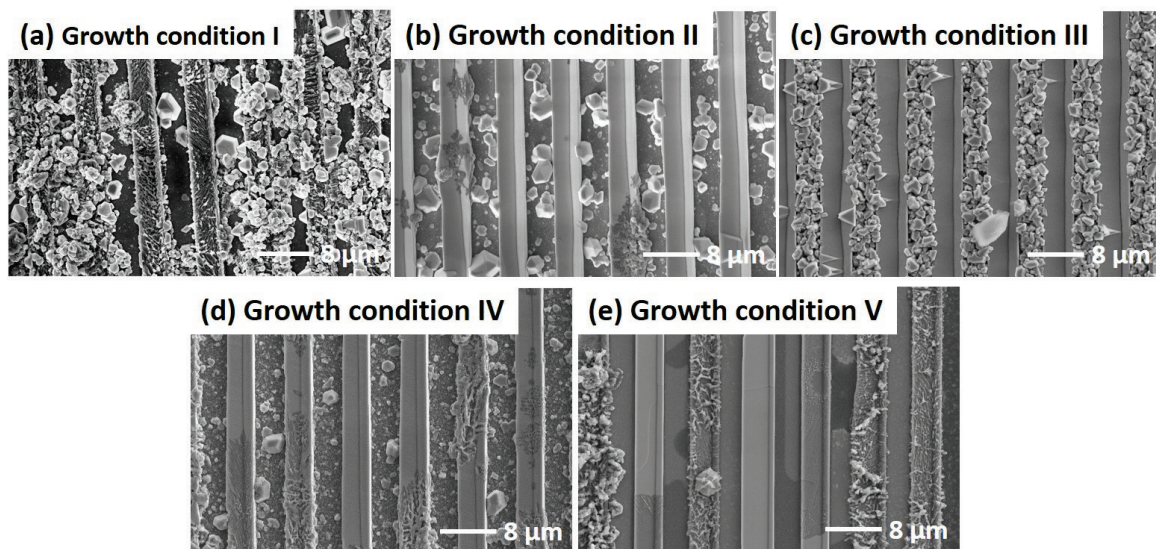


Figure 6.2: (a)-(e) Top view SEM images of GaN grown on the stripe patterned (113) Si substrate under the growth conditions described in Table 6.1

In order to avoid the melt-back etching during GaN growth, the thickness of AlN is increased from 100 to 400 nm in order to minimise the shadow effect. As shown in figure 6.2 (d), the melt-backing etching issue weakens but still occurs. Simultaneously, the parasitic growth of GaN on SiO₂ can also be observed. This can be understood as: AlN can be also deposited on SiO₂ due to the high sticking coefficient of Al [5], which serves as a nucleation layer for further GaN growth on top. A thicker AlN layer on SiO₂ enhances the probability for GaN to nucleate on AlN/SiO₂ layers and thus the parasitic growth of GaN on SiO₂. The influences of growth pressure and TMG flow rate on the surface morphology of the resultant

GaN have also been studied. As shown in Figure 6.2 (e), an improved surface morphology has been achieved grown under growth condition V in Table 6.1. The melt-backing etching issue weakens but still occurs.

In principle, GaN which exhibits excellent chemical stability cannot react with silicon. However, if there exist some GaN decomposition at a high temperature, the Ga metal as a result of the GaN decomposition will react with silicon at high temperatures [6, 7]. Therefore, if we can manage to suppress GaN decomposition, in principle we will be able to eliminate the Ga melting back etching issue. GaN decomposition can easily take place at high temperatures if it is not exposed to NH_3 [8]. For example, the well-formed M shape GaN stripes (i.e., generally after the coalescence) stop NH_3 flowing through the channels formed underneath as a result of the coalescence process, where the GaN decomposition can happen.

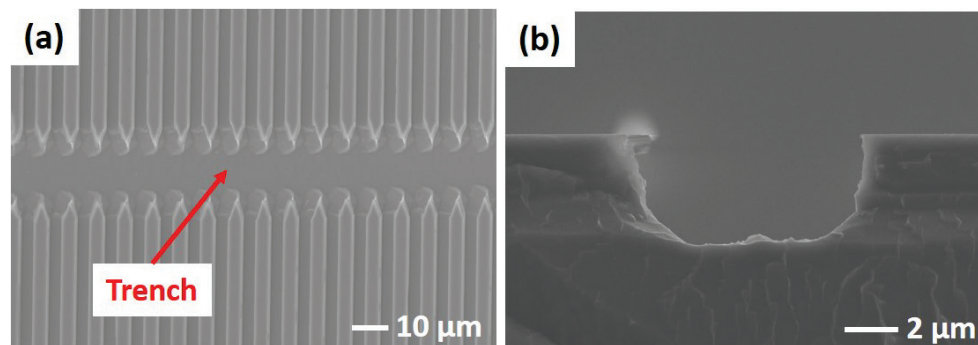


Figure 6.3: (a) Top view and (b) cross-sectional SEM images of the 10 μm trench introduced on original patterned Si substrate.

In order to address this issue, we design a new mask, where a number of extra wide trenches along a direction which is perpendicular to the stripe orientation are introduced, as shown in Figure 6.3. These wide trenches are used as tunnels to allow NH_3 to flow through the above mentioned channels. In our design, a number of 10 μm trenches with an interval of 5 mm across a whole wafer are introduced.

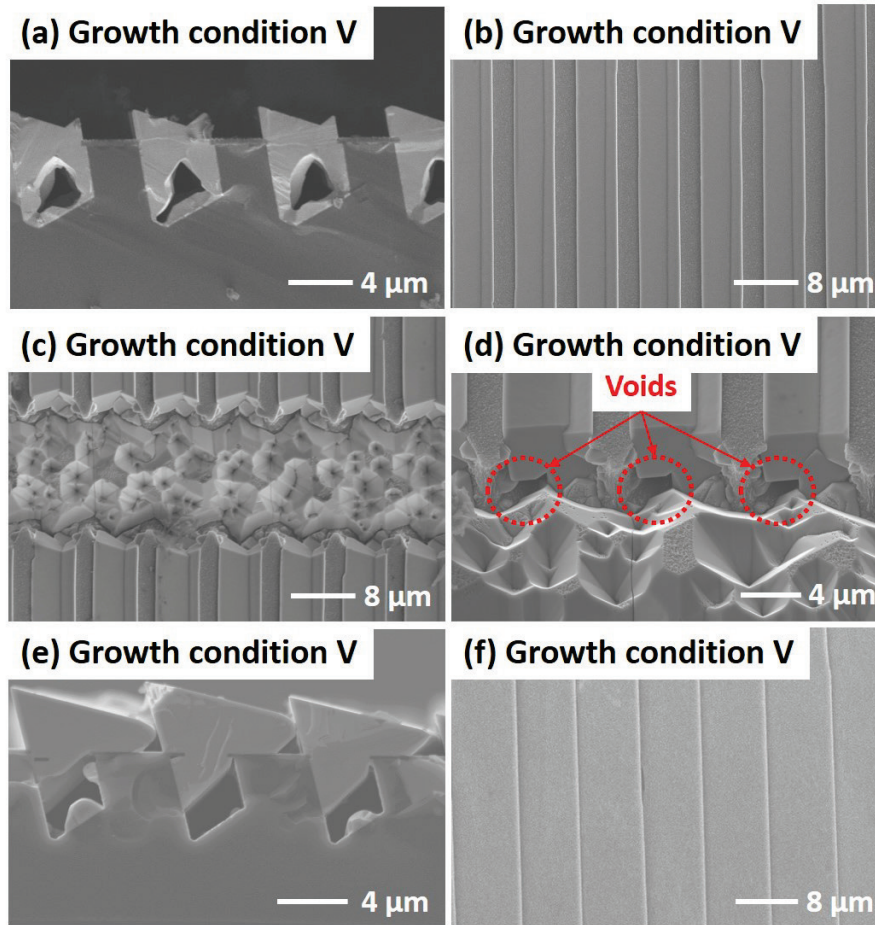


Figure 6.4: (a) Cross sectional SEM image, (b) and (c) top view SEM images, (d) SEM images taken with a 45° tilted angle of the GaN grown on the stripe patterned (113) Si without any miscut angle; (e) Cross sectional and (f) top view SEM images of the GaN grown on the stripe patterned (113) Si with a 4.89° miscut angle.

Based on the modified stripe patterned (113) Si substrate, GaN growth is carried out under the best growth condition achieved so far (i.e., 1125°C , 600 torr and 45 sccm TMG). As shown in Figures 6.4 (a) & (b), the melt-back etching has been successfully prevented. Although GaN can be grown in the trenches (a kind of poly-crystals with random orientations, and can be easily removed by a chemical solution) as shown in Figures 6.4 (c)-(d), the channels under the M-shape GaN stripes are not blocked so that NH_3 can flow through them. Therefore, the GaN decomposition can be effectively suppressed, preventing the melt-back etching issue.

In order to achieve precise semi-polar (20-21) GaN and also avoid the formation of the M-shape GaN for different application purposes, a (113) Si substrate with a 4.89° miscut angle is adopted. An identical patterning process is used. The best growth conditions are used (i.e.,

1125 °C, 600 torr and 45 sccm TMG) for GaN growth. Figures 6.4 (e) & (f) show the cross-sectional and plane-view SEM images of the sample, demonstrating that the M-shape surface has disappeared as a result of the growth occurring only on (-1-11) due to the increased inclination angle of the (11-1) facet, where the GaN growth on the (11-1) facet becomes difficult. In the meantime, the melt-backing etching issue has also been eliminated.

6.2 Structural and Optical Characterization

The crystal orientation of GaN grown on the stripe patterned (113) Si without and with any miscut angle obtained in section 6.1 have been characterized by HD-XRD measurements. Figure 6.5 shows the on-axis XRD measurements performed in a 2θ - ω symmetric mode. For the GaN grown on our patterned (113) Si without any miscut angle, namely, the sample with an offset angle of 4.89° , only a sharp diffraction peak of (113) Si is observed. In contrast, for the GaN grown on our patterned (113) Si with a miscut angle of 4.89° , only a sharp diffraction peak of GaN (20-21) is observed (Figure 6.5 (b)), indicating true (20-21) GaN has been obtained by growth on our patterned (113) Si with the miscut angle.

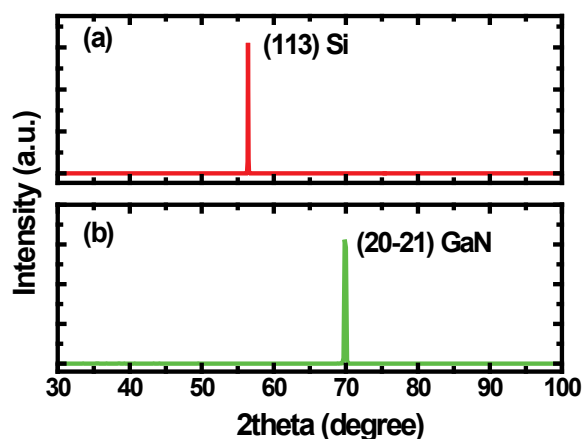


Figure 6.5: XRD 2θ - ω scan profile of the symmetric (20-21) GaN plane of the GaN grown on our stripe patterned (113) Si substrate (a) without and (b) with a 4.89° miscut angle.

The GaN in-plane crystal orientation has also been investigated by performing XRD measurements on the asymmetric GaN (0002) plane and the Si (-1-11) plane as a function of phi- and chi- angles, respectively, which are shown in Figures 6.6 and 7.7. For both samples, a single (0002) GaN peak is found at the same phi and chi positions of (-1-11) Si plane, meaning

that the [0001] direction for GaN is parallel to the [1-11] direction of the Si substrate. It is worth mentioning that for patterned (113) Si without any miscut angle GaN can be grown on both the sidewalls of the Si stripes, i.e., GaN can be grown on both the (-1-11) and the (11-1) Si facets. However, as (-1-11) and (11-1) Si facets are parallel to each other. Therefore, only a single GaN (0002) plane peak is observed. In addition, as shown in Figures 6.7(a) & (b), the chi positions of the GaN (0002) peak for the two samples are slightly different, which is due to the miscut angle of the Si substrate (one with a 4.89° miscut angle, and another one without it). The chi position shift is around 5°, which matches the miscut angle of 4.89° very well.

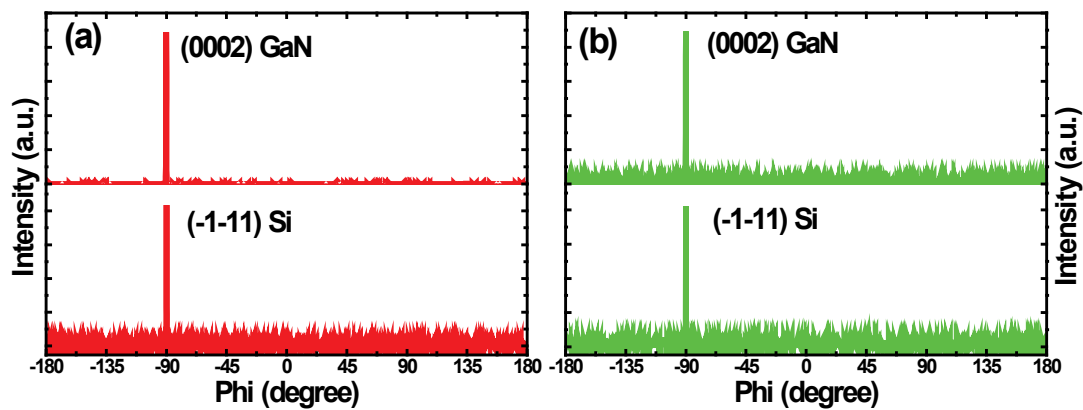


Figure 6.6: Phi dependent XRD spectra on the asymmetric (0002) GaN plane and the (1-11) Si plane of the GaN grown on our stripe patterned (113) Si substrates (a) without and (b) with a 4.89° miscut angle.

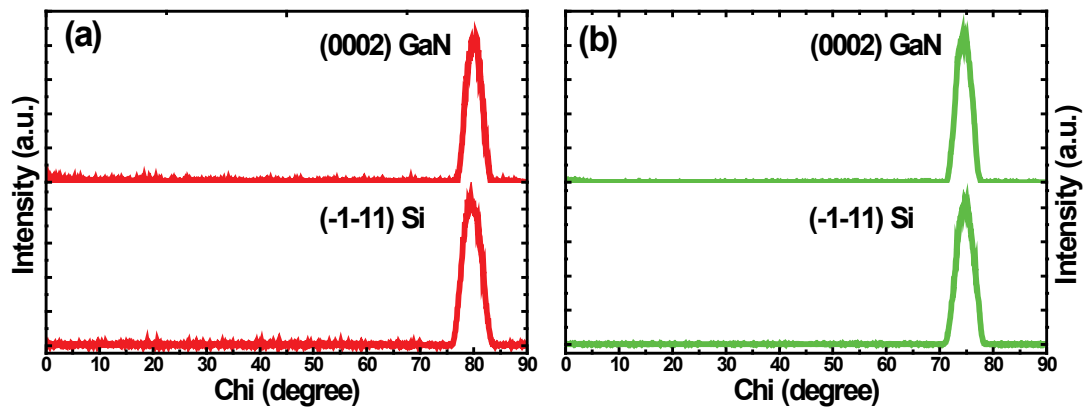


Figure 6.7: Chi dependent XRD spectra on the asymmetric (0002) GaN plane and the (1-11) Si plane of the GaN grown on our stripe patterned (113) Si substrates (a) without and (b) with a 4.89° miscut angle.

The top surface of the ‘M’ shape GaN stripe has also been investigated by both HD-XRD and SEM measurements. Figure 6.8 (a) shows that the angle between the top surface of the ‘M’ shape GaN stripes and the surface plane of Si (113) substrate is 18° (left red peak) and 38° (yellow peak), respectively, matching the angle measured through the chi dependent XRD measurement on asymmetric $\{10\text{-}11\}$ GaN planes as shown Figure 6.8(b). This indicates that two top surface planes of the GaN ‘M’ shape stripes are $\{10\text{-}11\}$ GaN planes, which are also the most stable plane due to its high thermal stability [9-13]. In addition, the right red peak at $\text{chi}=32.5^\circ$ in Figure 6.8(b) is also considered to arise from the $\{10\text{-}11\}$ GaN plane, corresponding to the GaN grown at the bottom plane of the trench.

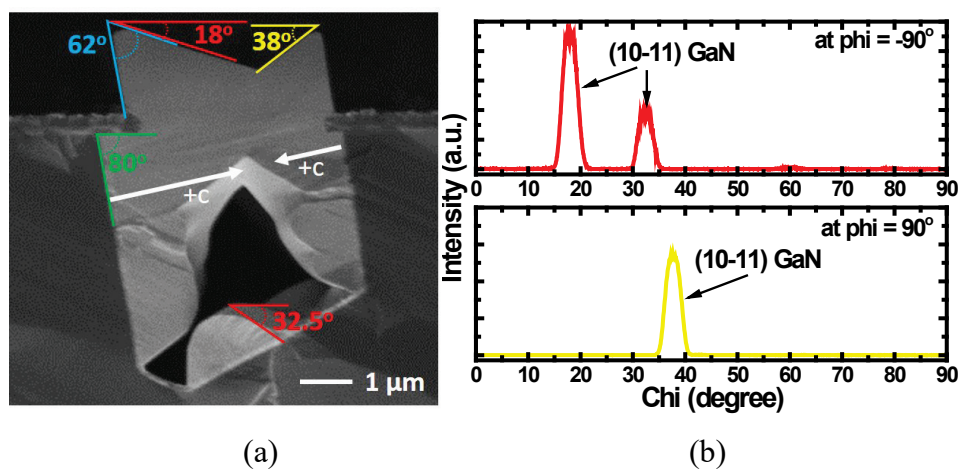


Figure 6.8: (a) Cross sectional SEM of the GaN grown on our stripe patterned (113) Si without any miscut angle, (b) XRD chi-scan profile of the asymmetric (10-11) GaN planes.

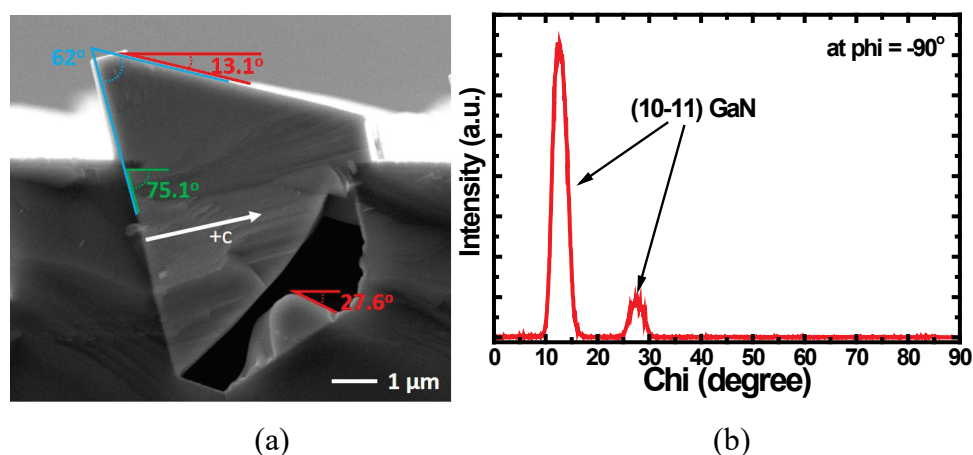


Figure 6.9: (a) Cross-sectional SEM of GaN grown on the stripe patterned (113) Si with a miscut angle of 4.89° (b) Chi dependent XRD spectra on the asymmetric (10-11) GaN planes.

For the GaN grown on our patterned (113) Si with a 4.89° miscut angle, the angle between the GaN top surface plane and the horizontal plane is 13.1° (Figure 6.9(a)), which is equal to the chi position of {10-11} plane of GaN, as revealed by the chi-dependent XRD measurements of the asymmetric (10-11) GaN planes (Figure 6.9(b)). This indicates the surface plane of the GaN grown on the patterned (113) Si with a 4.89° miscut angle is the {10-11} plane.

In a short summary, for the GaN grown on the patterned (113) Si without any miscut angle (Figure 6.8), the angle between the GaN top surface plane and the horizontal plane is 18° as shown in Figure 6.8(a), while it drops to 13° for the GaN grown on the patterned (113) Si with the miscut angle as shown in Figure 6.9(a). This difference of ~ 5 degree matches the miscut angle (4.89°) very well.

The crystal quality has been investigated by HD-XRD rocking curve measurements. Figure 6.10 shows XRD rocking curves of the (20-21) GaN on the patterned (113) Si substrate without any miscut angle, demonstrating FWHMs of 0.1422° and 0.1432° measured along GaN [0001] and GaN [10-10], respectively.

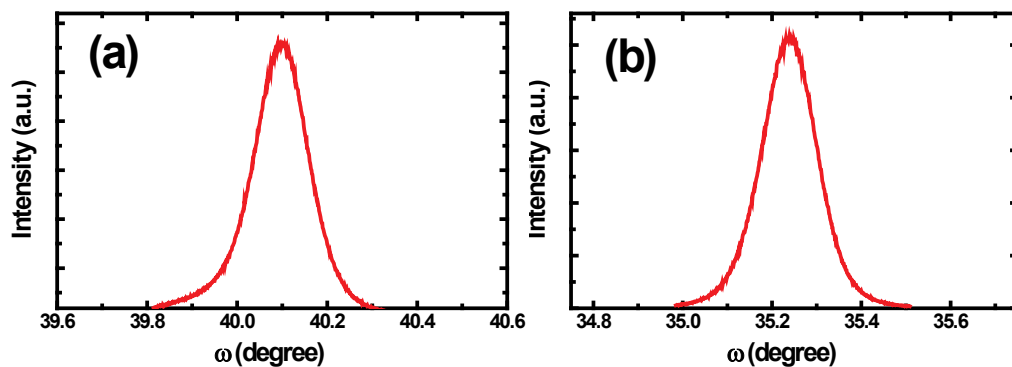


Figure 6.10: XRD rocking curves of the (20-21) GaN grown on the patterned (113) Si without any miscut angle, measured (a) along GaN [0001] and (b) along GaN [10-10].

Similarly, for the (20-21) GaN grown on the patterned (113) Si substrate with a miscut angle of 4.89° , Figure 6.11 shows on-axis XRD rocking curves of the (20-21) GaN, indicating FWHMs of 0.1486° and 0.1400° , measured along GaN [0001] and along GaN [10-10], respectively. Detailed azimuth angle dependent XRD rocking curve measurements have been carried out, and are shown in Figure 6.12. The FWHMs are between 0.1576° and 0.1400° , which are much narrower than any other reports on (20-21) GaN with a similar thickness

grown on either patterned Si ($0.169^\circ - 0.414^\circ$) or patterned sapphire ($0.188^\circ - 0.408^\circ$) [12, 13]. Off-axis XRD rocking curves measurements along (000n) and (n0-n0) directions have also been carried out. The FWHMs of the off-axis XRD rocking curves for (0002), (0004) and (0006) GaN plane along are 0.2534° , 0.2463° and 0.2666° , respectively. The FWHM of the off-axis XRD rocking curves for (10-10), (20-20) and (30-30) GaN plane are 0.1479° , 0.1548° and 0.1593° , respectively.

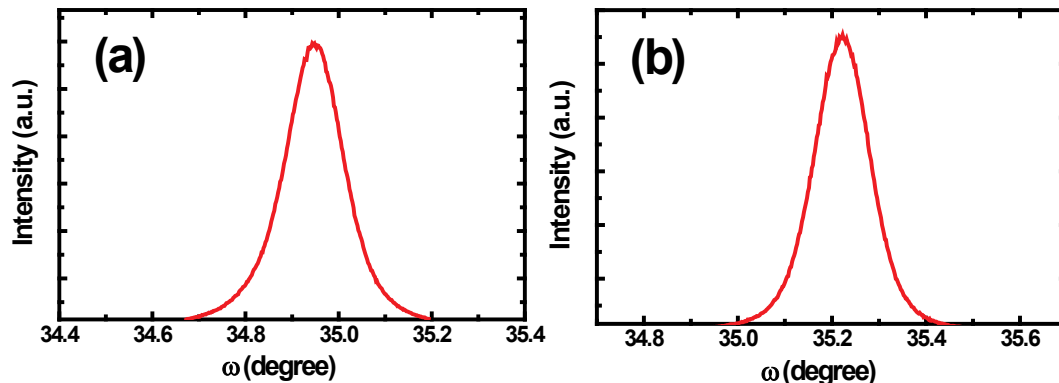


Figure 6.11: XRD rocking curve of the (20-21) GaN grown on the patterned (113) Si with a miscut angle of 4.89° , measured (a) along GaN [0001] or (b) along GaN [10-10].

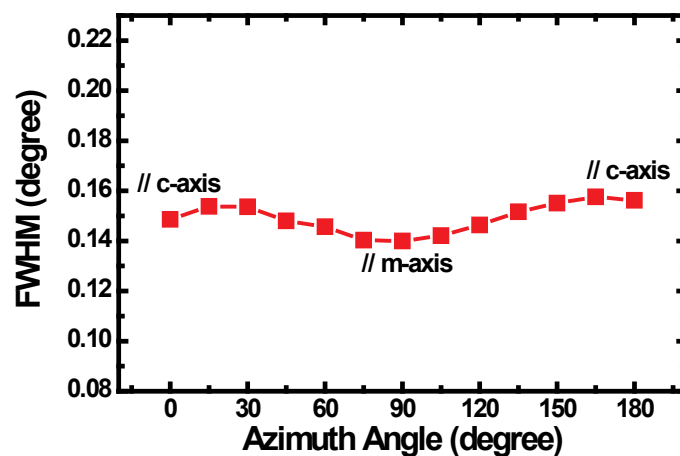


Figure 6.12: FWHM of XRD rocking curves as a function of an azimuth angle.

The microstructure has been further investigated by TEM measurements on the (20-21) GaN grown on the patterned Si without any miscut angle. Figures 6.13 (a) and (b) show the cross sectional TEM images taken with $g=0002$ and $g=11-20$, respectively. As can be seen, most dislocations could only be observed at the interface between GaN and the Si facet. With the GaN growth proceeding along the +c direction, the dislocation density decreases dramatically due to the defect interaction and the dislocation bending, leading very few

dislocations to penetrate to the surface of the GaN stripes.

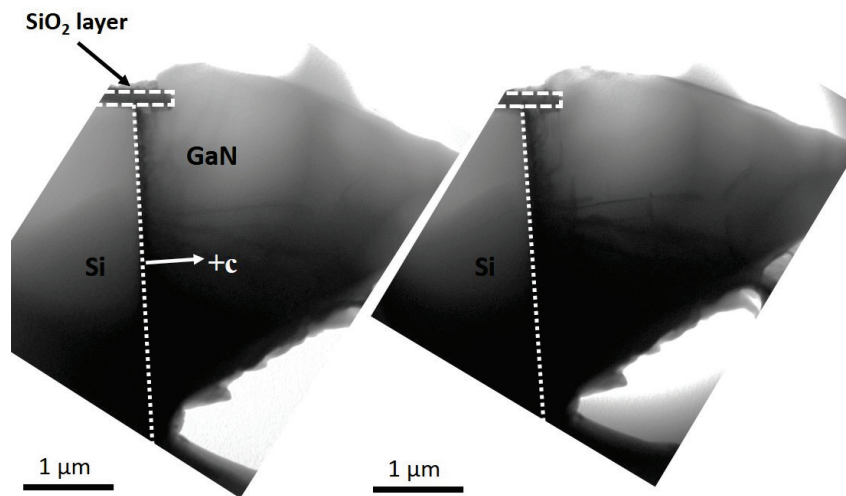


Figure 6.13: Cross sectional TEM images of the (20-21) semi-polar GaN grown on the patterned Si without any miscut angle, taken around $[1-100]$ zone-axis with (a) $\mathbf{g}=0002$ and (b) $\mathbf{g}=11-20$.

The reduction in BSFs has been studied by TEM measurements measured with $\mathbf{g}=10-10$ as shown in Figure 6.14. The BSFs initiate at the GaN/Si interface, lying on the c-planes. As the GaN growth along the +c direction, it is clearly observed that all BSFs are confined at the GaN/Si interface, which is the same as discussed in section 5.3. Apart from the interface area, there are very few BSFs generated during the GaN growth along +c-direction. The mechanism accounting for the BSF reduction is considered to be the same as that discussed in Chapter 5.3, namely, the BSF density of the GaN growth along the c-direction is inherently low. Moreover, most of the existing BSFs at the interface are blocked by the overhanging SiO₂ layer, which could prevent BSFs from propagating to the Si surface, leading to a further reduction in BSF density. For the (20-21) GaN grown on either patterned Si or sapphire by other groups [10,11], the BSFs are also impeded as a result of enhanced GaN growth along the [0001] direction, but the existing BSFs at the interface between GaN and silicon would extend to the surface without being blocked. This comparison demonstrates the major advantages of our approach in terms of reducing BSFs.

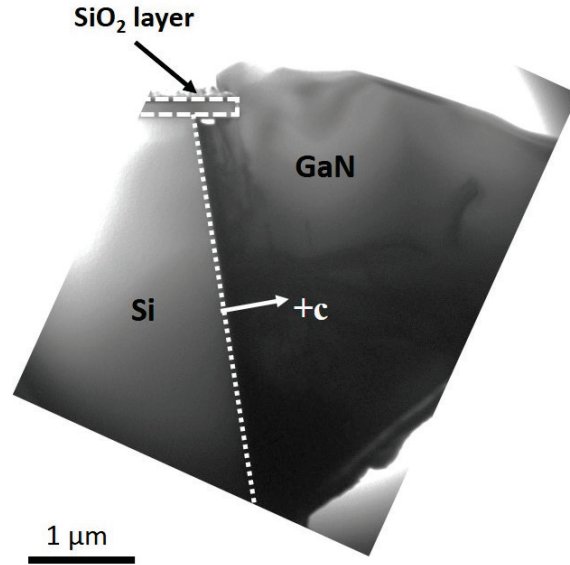


Figure 6.14: Cross sectional TEM image of the (20-21) semi-polar GaN grown on the patterned Si without any miscut angle, taken with a near $[1-210]$ zone-axis with $g=10-10$.

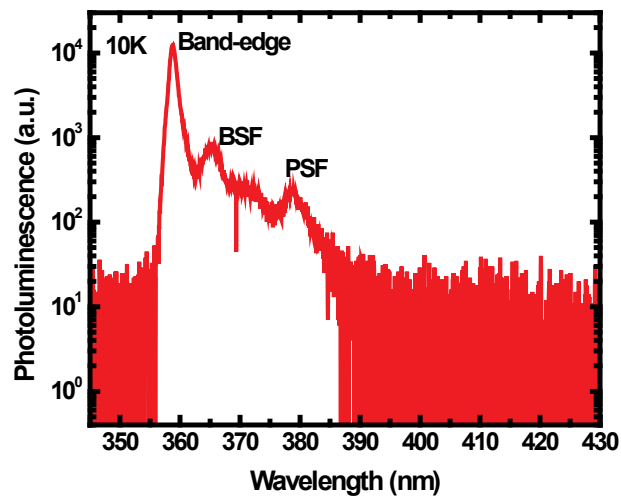


Figure 6.15: PL spectrum of the (20-21) GaN grown on the patterned (113) Si without any miscut angle, measured at 10 K

Further evidence of the significantly reduced BSF density of the (20-21) GaN include PL measurements performed at 10K. Figure 6.15 shows the PL spectrum of the (20-21) GaN on the stripe patterned (113) Si without any miscut angle, demonstrating that the PL is dominated by a very strong band-edge emission accompanied with very weak BSF and PSF related emissions located on the lower energy side. The PL intensity of the band-edge emission is more than one order magnitude higher than that of the BSF or PSF related emission.

6.3 InGaN MQWs grown on (20-21) GaN

InGaN MQW structures have been attempted to be grown on the top of the (20-21) GaN stripes with an M-shape in order to validate the crystal quality of our (20-21) GaN. As illustrated in Figure 6.16, sample A contains 5 pairs of InGaN/GaN MQWs with a well thickness of 2 nm and a barrier thickness of 12 nm, respectively, where the emission wavelength is at 460 nm. Sample B contains the same MQW structure but only with 3 pairs of InGaN/GaN MQWs, and the indium content in InGaN well is higher than that in sample A, leading to an emission wavelength at 490 nm.

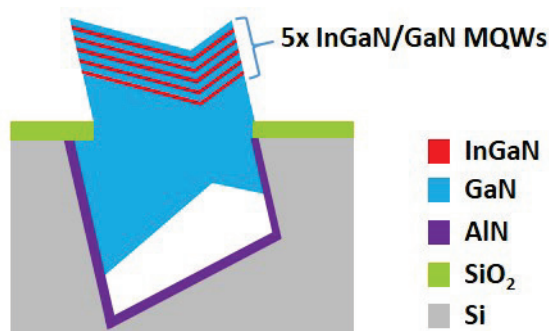


Figure 6.16: Schematic of the InGaN/GaN MQW structure of sample A

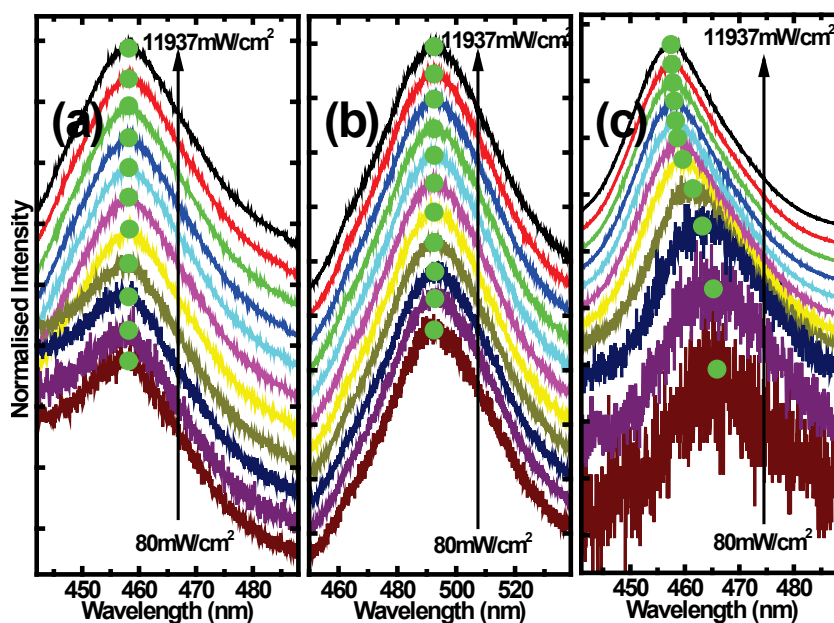


Figure 6.17: Excitation power dependent PL spectra of InGaN QWs grown on (a) & (b) ‘M’ shape GaN stripes and (c) c-plane GaN.

Excitation power dependent PL measurements have been measured on both samples in order to study any change in QCSE as shown Figure 6.17, demonstrating that there is no obvious blue shift for both samples when the excitation power increases from 80 to 11937 mW/cm². For comparison, standard InGaN/GaN MQWs with a similar emission wavelength grown on c-plane GaN has been measured, and the excitation power dependent PL spectra have been provided in Figure 6.17, showing a blue shift of 8.5 nm (or 50 meV) in emission wavelength as expected, measured under identical conditions. This is due to the screening effect of the QCSE as a result of optically generated electrons [14, 15]. This comparison has clearly confirmed that the QCSE has been significantly suppressed in the InGaN/GaN MQWs grown on the (20-21) GaN.

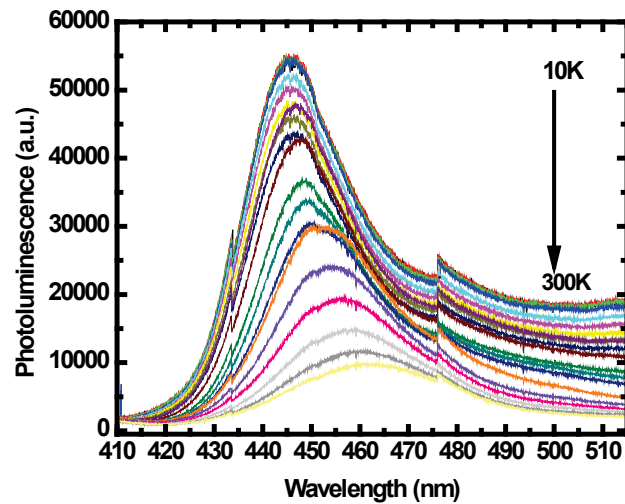


Figure 6.18: Temperature dependent PL spectra of sample A.

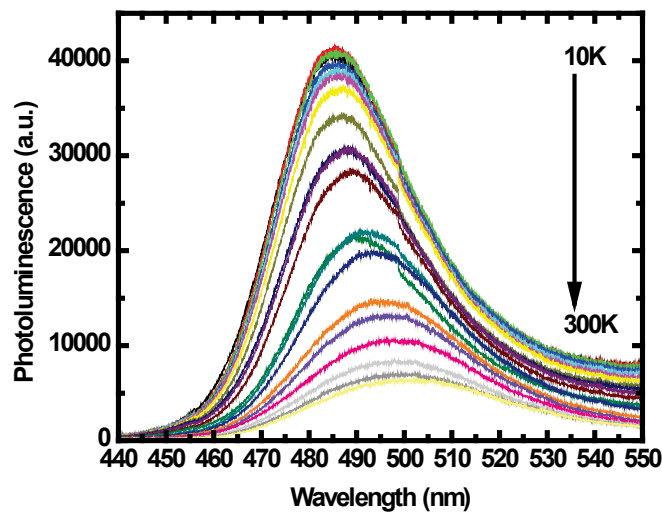


Figure 6.19: Temperature dependent PL spectra of sample B

The IQE of an InGaN/GaN MQW structure can be roughly estimated by performing temperature dependent PL measurements, as it can be simply assumed that non-radiative recombination centres are frozen at a low temperature, such as 10K. Based on this assumption, it has been generally accepted that electron-hole recombination at a low temperature is dominated by a radiative recombination process and the IQE at the low temperature can be assumed to be 100 %. The IQE at room temperature (300K) can be estimated by calculating the ratio of the integrated PL intensity at 300K to that at 10K [15, 16]. Of course, this method is not accurate, as it is affected by a number of other factors, such as excitation power, etc. Therefore, temperature dependent PL measurements will not allow us to obtain accurate IQE. However, it is useful to make a comparison of the IQE of different samples if the measurement conditions are identical. The temperature dependent PL measurements have been taken on both samples A and B, as shown in Figures 6.18 and 6.19, respectively. Figure 6.20 shows the integrated PL intensity as a function of temperature for sample A and B in term of an Arrhenius plot, which is obtained by plotting the inversion temperature versus the logarithm of normalized integrated PL intensity. The Arrhenius plot is generally used to study the effect of temperature on chemical reactions. For semiconductor PL characterisations, it can be used to extract information relating to the thermal activation energy and the localization depth. As shown in Figure 6.20, the ratio of the integrated PL intensity for sample A is 20.0%, which is slightly higher than that for sample B. Although the emission wavelength of sample B is more than 30 nm longer than that for sample A, the IQE does not drop so much, which is very different from their counterparts grown on c-plane GaN whose IQE normally significantly decreases with increasing emission wavelength, in particular when the wavelength approaches the green spectral region. This clearly demonstrates the major advantages of semi-polar GaN for the growth of longer wavelength emitters.

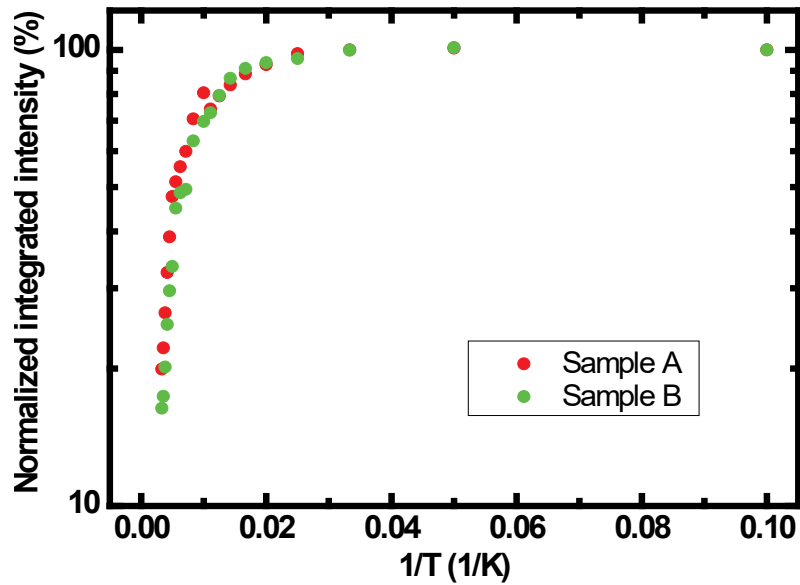


Figure 6.20: Normalized PL integrated intensity as a function of temperature in an Arrhenius plot.

Furthermore, high spatial-resolution confocal PL measurements have been performed on sample A and sample B. The typical spatial resolution is 160 nm. The confocal PL mapping measurements have been carried out at room temperature. The corresponding confocal PL integrated intensity mapping and the PL spectrum measured on the InGaN/GaN MQWs on the (20-21) GaN stripe have been provided in Figures 6.21 and 7.22 for samples A and B, respectively.

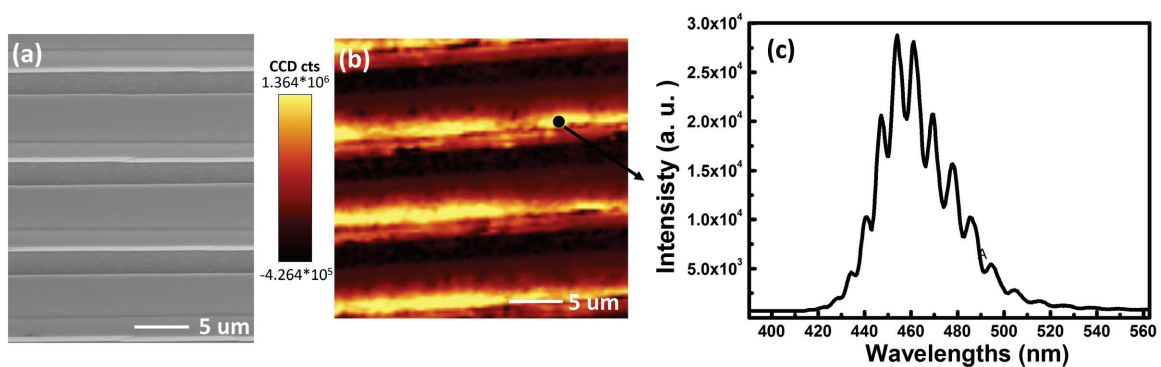


Figure 6.21: (a) Top view SEM of sample A; (b) confocal PL intensity mapping and (c) PL spectrum measured at one random point specified in Figure b.

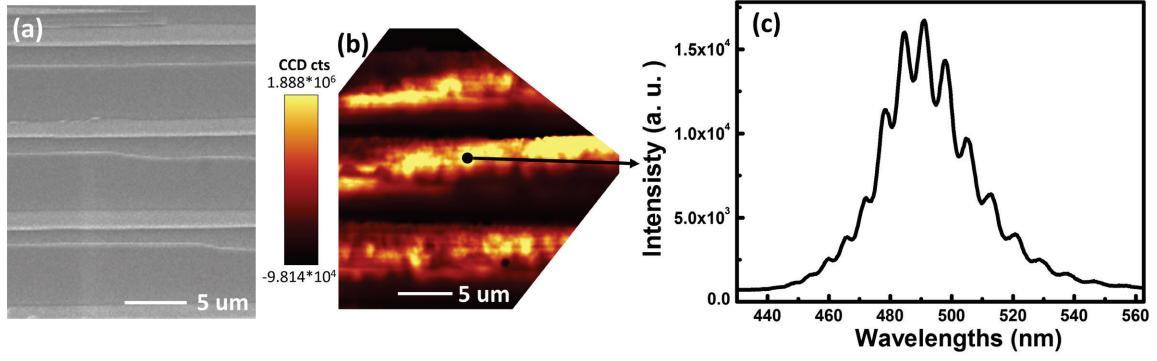


Figure 6.22: (a) Top view SEM of sample B; (b) confocal PL intensity mapping and (c) PL spectrum measured at one random point specified in Figure b.

As shown in both Figures 6.21(c) and 7.22(c), the spectrum in each case shows multiple peaks, which could be ascribed to the optical interference from the parallel sidewalls of the ‘M’ shape GaN stripes. The confocal system has a high spatial resolution and the sidewalls of GaN stripe are smooth, forming Fabry-Perot modes [17]. For the Fabry-Perot mode, the following equation has to be satisfied:

$$m\lambda = 2nL \quad (7.1)$$

where m is an integer, λ is the wavelength, n is the medium refractive index of cavity ($n_{\text{GaN}} \approx 2.48$ or 2.45 at wavelength of 460 and 490nm , respectively) [18], and L is the cavity length. The relationship between mode separation ($\Delta\lambda$) and cavity length is described by:

$$\Delta\lambda = \frac{\lambda^2}{2nL} \quad (7.2)$$

Figures 6.21(c) and 7.22(c) show the spectral separation between multiple peaks is around 7.0 nm and 6.8 nm for sample A and B, respectively. Based on question 7.2, the cavity lengths for the sample A and B are around $6\text{-}7$ μm , respectively. This matches the GaN stripe width for these two samples as shown in their cross-sectional SEM images.

Cathodoluminescence (CL) measurements have also been performed on sample A at room temperature. In comparison with PL, CL is also designed to analyse the luminescence emitted from a sample. But instead of laser, CL uses an electron beam as excitation power, which can be focused into a nanoscale probe and gives a spatial resolution down to 20 nm. As shown in Figure 6.23, the results obtained are similar to those measured by our confocal measurements,

namely, clear optical modes have been observed.

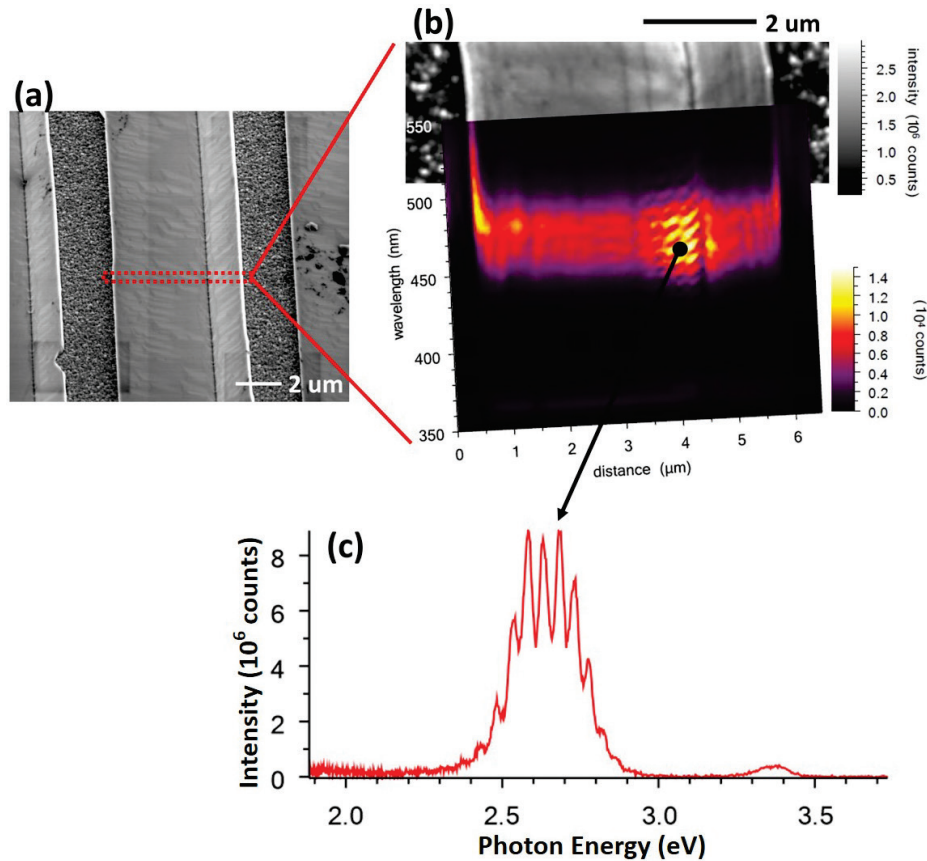


Figure 6.23: (a) Top view SEM image of sample A; (b) CL intensity mapping and (c) CL spectrum measured on the MQWs in the centre position of the (20-21) GaN stripe.

6.4 Conclusion

Semi-polar (20-21) GaN has been successfully achieved by means of growth on our specially designed patterned (113) Si substrates. The influence of both GaN growth conditions and the Si substrate miscut angle has been investigated. When (113) Si substrates without any miscut angle are adopted, semi-polar (20-21) GaN with a 4.89° offset angle can be obtained, forming ‘M’ shape GaN stripes. When (113) Si substrates with a 4.89° miscut angle are adopted for growth, an almost coalesced film of semi-polar (20-21) GaN with a 0° offset angle has been obtained. Like all other reported GaN growth on patterned Si substrates with undercut geometry grooves, the risk of melt-back etching issue is always high due to a large number of unavoidable residual voids during GaN growth, leaving the grown GaN to have the high possibility of contacting unprotected undercut Si facets. In this study, by introducing 10 μm

gaps on the Si stripe patterns, the melt-back etching issue has been successfully prevented. The obtained semi-polar (20-21) GaN demonstrates excellent crystal and optical qualities, confirmed by HD-XRD, PL and TEM measurements. The FWHMs of the XRD on-axis rocking curves of our (20-21) GaN are between 0.158° and 0.140° , which is the best result so far. For another two reported approaches of (20-21) GaN growth, which utilise patterned Si substrates or patterned sapphire substrates [12, 13], the FWHMs of the XRD on-axis rocking curves are $0.169^\circ - 0.414^\circ$ or $0.188^\circ - 0.408^\circ$, respectively. Low temperature PL measurements show a high ratio of the near band edge emission intensity to the BSF related emission intensity, indicating a quite low BSF density. Based on TEM measurements, the mechanism of the defect reduction has been investigated. Furthermore, InGaN MQWs have been attempted to be grown on the (20-21) GaN, and detailed optical measurements have been carried out. These have validated the excellent quality of the (20-21) GaN.

References

1. M. T. Hardy, D. F. Feezell, S. P. DenBaars, and S. Nakamura, *J. Electrochem. Soc.* **158**, 408 (2011)
2. N. Suzuki, T. Uchida, T. Tanikawa, T. Hikosaka, Y. Honda, M. Yamaguchi, and N. Sawaki, *J. Cryst. Growth* **311**, 2875 (2009)
3. T. Meisch, M. Alimoradi - Jazi, M. Klein, and F. Scholz, *Phys. Stat. Sol. (c)* **11**, 537 (2014)
4. A. Rebey, T. Boufaden, and B. El Jani, *J. Cryst. Growth* **203**, 12 (1999)
5. V. Laneuville, F. Demangeot, R. Péchou, P. Salles, A. Ponchet, G. Jacopin, L. Rigutti, A. de Luna Bugallo, M. Tchernycheva, F. H. Julien, and K. March, *Phys. Rev. B* **83**, 115417 (2011)
6. D. D. Koleske, A. E. Wickenden, R. L. Henry, M. E. Twigg, J. C. Culbertson, and R. J. Gorman, *Appl. Phys. Lett.* **73**, 2018 (1998)
7. K. Takemoto, H. Murakami, T. Iwamoto, Y. Matsuo, Y. Kangawa, Y. Kumagai, and A. Koukitu, *Jpn. J. Appl. Phys.* **45**, L478 (2006)
8. M. Mayumi, F. Satoh, Y. Kumagai, K. Takemoto, and A. Koukitu, *Jpn. J. Appl. Phys.* **39**, L707 (2000)
9. T. Wunderer, P. Brückner, J. Hertkorn, F. Scholz, G. J. Beirne, M. Jetter, P. Michler, M. Feneberg, and K. Thonke, *Appl. Phys. Lett.* **90**, 171123 (2007)
10. T. Wunderer, F. Lipski, J. Hertkorn, P. Brückner, F. Scholz, M. Feneberg, M. Schirra, K. Thonke, A. Chuvilin, and U. Kaiser, *phys. stat. sol. (c)* **5**, 2059 (2008)
11. T. Liu, J. Zhang, X. Su, J. Huang, J. Wang, and K. Xu, *Scientific reports* **6**, 26040 (2016)
12. T. Meisch, M. Alimoradi - Jazi, M. Klein, and F. Scholz, *Phys. Status Solidi C* **11**, 537 (2014)
13. M. Khoury, M. Leroux, M. Nemoz, G. Feuillet, J. Zúñiga-Pérez, and P. Vennéguès, *J. Cryst. Growth* **419**, 88 (2015)
14. H. Yu, L. K. Lee, T. Jung, and P.C. Ku, *Appl. Phys. Lett.* **90**, 141906 (2007)
15. K. Xing, Y. Gong, J. Bai, and T. Wang, *Appl. Phys. Lett.* **99**, 181907 (2011)
16. Y.-L. Li, Y.-R. Huang, and Y.-H. Lai, *Appl. Phys. Lett.* **91**, 181113 (2007)
17. Y. C. Chang, Y.-L. Li, D. B. Thomson, and R. F. Davis, *Appl. Phys. Lett.* **91**, 051119 (2007)

18. M. E. Lin, B. N. Sverdlov, S. Strite, H. Morkov, and A. E. Drakin, *Electronics Letters* **29**, 1759 (1993)

Chapter 7

Self-induced GaN Nanowires Grown on (111) Si Substrates

7.1 Nanowire Growth with TMA Pre-flowing

The growth of GaN NW was performed by MOCVD on 2-inch planar (111) Si substrates. First, the Si substrate is subject to a thermal annealing process in a H₂ ambient as usual. TMA pre-flowing is then performed by depositing a small amount of TMA on the Si substrate at a high temperature. Following that, the GaN NW growth is carried out. The TMA pre-flowing and GaN growth are carried out under various conditions, as illustrated in Tables 7.1 & 7.2. The pressure used during the TMA pre-flowing and the GaN NW growth period is 65 and 300 Torr, respectively.

TMA pre-flowing condition	T (°C)	Flow rate (sccm)	Time (sec)
TMA pre-flowing I	1145	120	6
TMA pre-flowing II	1145	120	10
TMA pre-flowing III	866	120	6
TMA pre-flowing IV	1145	30	24
TMA pre-flowing V	1145	10	72
TMA pre-flowing VI	1145	6	120

Table 7.1: Different growth conditions of TMA pre-flowing.

The initial stage of the growth is a key step, which determines the formation of NWs. First of all, the effect of the TMA pre-flowing on initialization of the NW growth has been investigated. Two samples are grown under identical GaN growth conditions (i.e., condition I listed in Table 7.2), but one is grown with TMA pre-flowing (pre-flowing I in Table 7.1) and another without. The surface morphologies of two samples are investigated by SEM measurements as shown in Figures 7.1 (a) & (d). It has been found that the TMA pre-flowing is

crucial to the initialisation of NWs. For the sample without TMA pre-flowing, only GaN clusters with both random orientations and diameters are observed. In contrast, GaN NWs with regular orientations has been obtained for the sample with TMA pre-flowing. The key role of the pre-flowing TMA on the Si substrate is that it would generate Al-Si alloyed nanodots serving as nucleation sites for NW growth. This is completely different from catalyst VLS growth of GaN NWs, where metal nano-droplets are utilized to activate the NW growth [1-4]. To verify this, only the TMA pre-flowing process has been performed on a (111) Si substrate without any GaN growth, where there are many nanodots observed as shown in Figure 7.1(b). In order to confirm whether these dot are Al dots or not, the sample is immersed in nitric acid (69% w/w) for 20 minutes treatment. However, the morphology remains unchanged as shown in Figure 7.1(c), indicating that the nanodots are composed of acid-resistant Al-Si alloys instead of Al. The morphology also remains unchanged after a phosphoric or hydrochloric acid treatment.

Next, the influence of TMA pre-flowing on the GaN NW growth morphology is studied through modifying growth temperature and the flow rate of TMAI. Figures 7.1(d)-(i) show the bird's-eye view SEM images of six samples grown using the conditions listed in Table 7.1, whereas the subsequent GaN growth conditions for these samples are kept the same. It has been found that the GaN NWs are typically grown on the top such Al-Si alloys as aforementioned. The morphology displayed in Figures 7.1(d)-(i) suggests that the TMA pre-flowing significantly affects the subsequent GaN NW growth. With a large amount of TMA precursor, only GaN islands instead of NWs are obtained, and their diameters are up to micrometres, as illustrated in Figure 7.1(e). This is attributed to the dense Al-Si nanodots, which form large flakes serving as the nucleation area for the subsequent GaN growth. On the other hand, a high growth temperature of 1145°C is also found to play a critical role in the formation of Al-Si alloys. In the case of the TMA pre-flowing performed at a much lower temperature at 866 °C, Figure 7.1(f) shows that only micrometer-sized GaN islands can be observed due to the lack of Al-Si alloy which is generally formed at a high temperature above 1100°C.

Furthermore, the influence of the TMA flow rate has been systematically studied. The flow rate is varied from 120 to 6 sccm, while the total amount of the TMA precursor is fixed by increasing the pre-flowing time (I, IV-VI in Table 7.1). Figures 7.1(d), (g) and (h) indicate that

the NW density increases when the flow rate is reduced to 10 sccm. Further decreasing the flow rate to 6 sccm, the morphology turns back to micrometer-sized islands again, shown in Figure 7.1(i). This is ascribed to the difficulty in formation of Al-Si alloys at a very low flow-rate, due to the dominance of desorption of Al atoms.

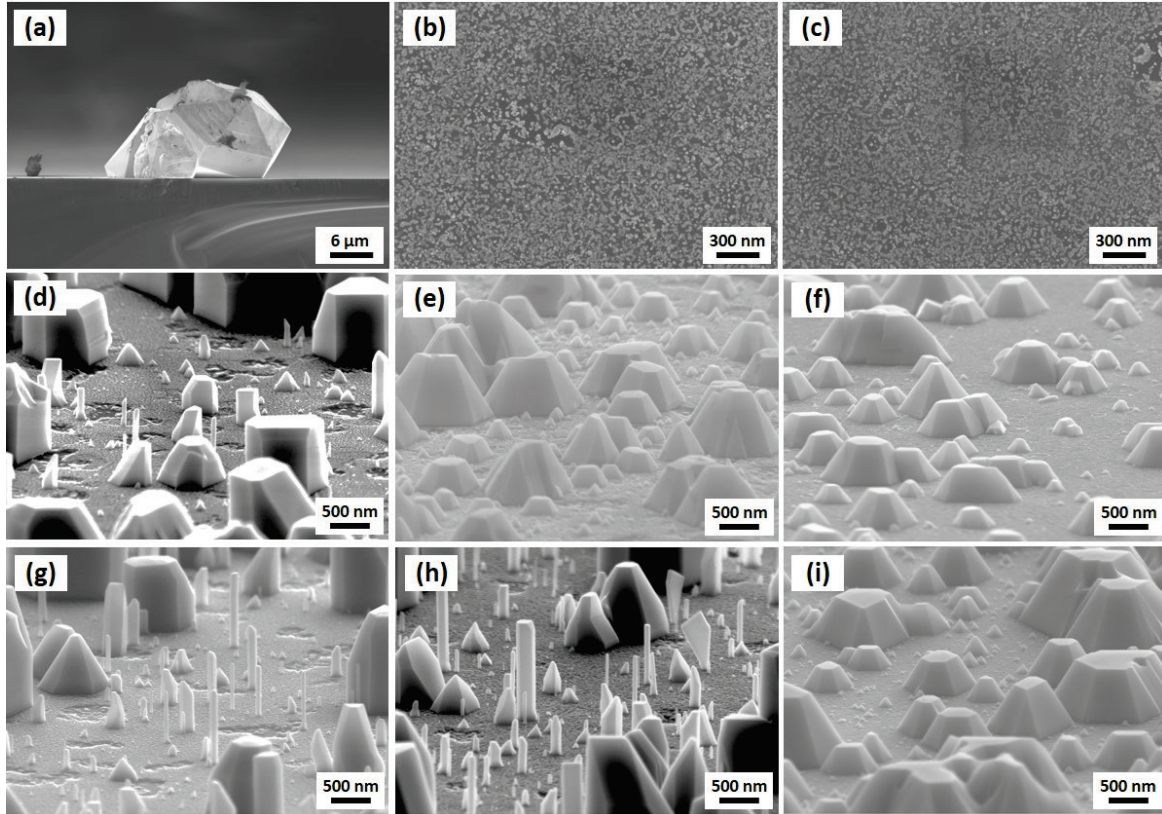


Figure 7.1: (a) Cross sectional SEM image of GaN directly grown on Si without the TMA pre-flowing; (b)&(c) top view SEM images of Si surface with the TMA pre-flowing before and after acid treatment; (d)-(i) bird's-eye view SEM images of GaN NWs grown under TMA pre-flowing conditions of 'I-VI' listed in Table 7.1, respectively.

7.2 Effects of GaN Growth Condition

In addition to the TMA pre-flowing conditions, the GaN NW growth also needs to be optimised by varying the growth conditions (Table 7.2). For all the samples, the TMA pre-flowing is kept the same (TMA pre-flowing V in Table 7.1), and the GaN growth time is varied when the flow rate of TMG is changed, in order to keep total deposited material (Ga source) the same. Firstly, at the same growth temperature (800 °C), the flow rates of NH₃ and TMG are changed (GaN condition I-IV in Table 7.2). As shown in Figures 7.2 (a) and (c), by

reducing a NH_3 flow rate, more GaN NWs are grown with a smaller size. The morphology analysis of GaN NWs is illustrated in Figure 7.3, where the minimum NW diameter is around 50 nm. Comparing with Figures 7.3 (a) and (c), a low NH_3 flow rate facilitates the formation of NWs with a small diameter and a long height, indicating that a high NH_3 flow rate suppresses the nucleation of GaN NW growth [5]. Then, with a NH_3 flow rate of 450 sccm, the flow rate of TMG is modified from 2 to 5 sccm. The SEM images and the NW morphology analyses of the samples are shown in Figures 7.2 (b), (c), (d) and Figures 7.3 (b), (c), (d). By increasing TMG flow rate from 2 to 2.5 sccm, more GaN NWs appear, especially for the small NWs. But with further increasing the TMG flow rate from 2.5 to 5sccm, GaN NWs start to coalesce to form large NWs, leading to more large NWs and a reduction in NW density. The optimised flow rates of NH_3 and TMG are 450 sccm and 2.5 sccm (GaN condition III), respectively.

GaN Growth Condition	T (°C)	NH_3 (sccm)	TMG (sccm)	Growth time (sec)
GaN condition I	800	1100	2.5	3840
GaN condition II	800	450	2	4800
GaN condition III	800	450	2.5	3840
GaN condition IV	800	450	5	1920
GaN condition V	866	450	2.5	3840
GaN condition VI	820	450	2.5	3840
GaN condition VII	775	450	2.5	3840

Table 7.2: Different growth conditions of GaN NW growth.

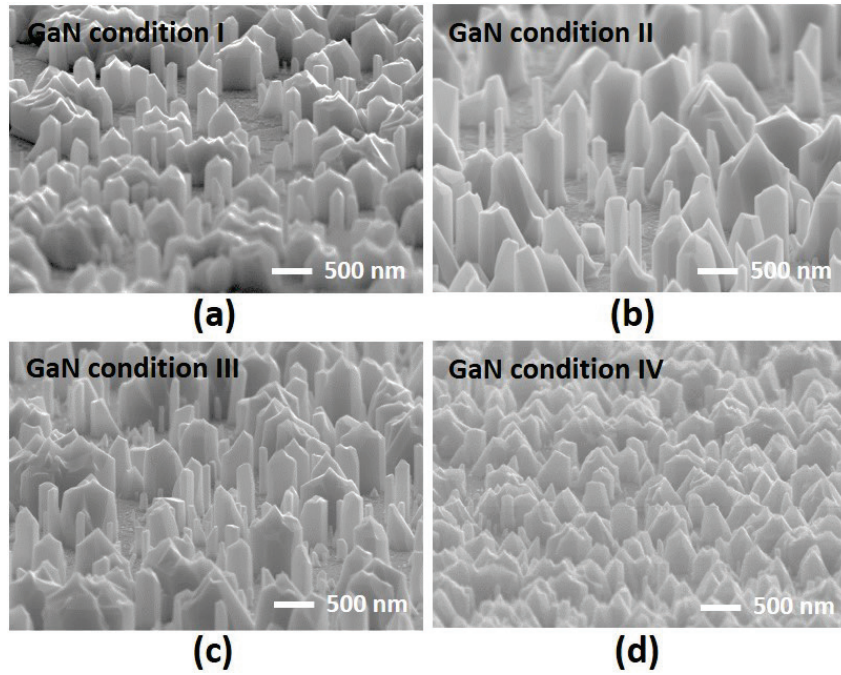


Figure 7.2: Bird's-eye view SEM of GaN NW growth with GaN condition I to IV.

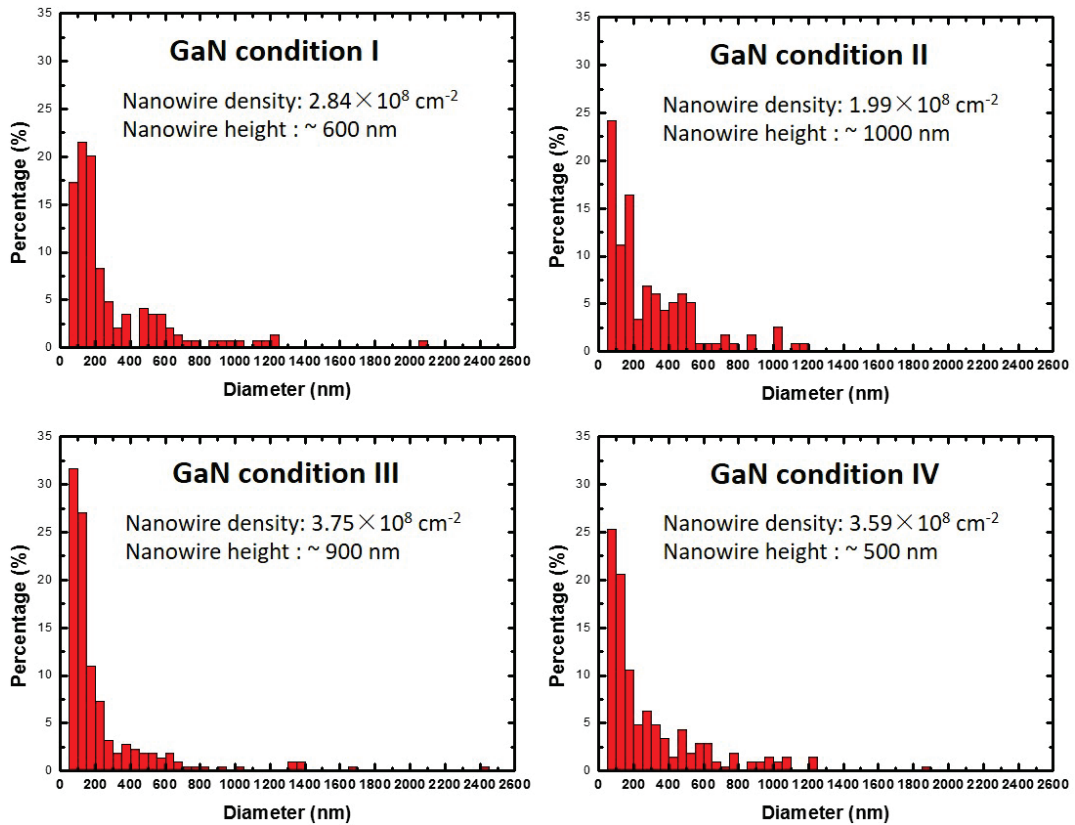


Figure 7.3: Diameter distribution, density and height of GaN NWs grown with GaN condition I to IV.

The influence of GaN growth temperature has been investigated, shown in Figures 7.4 and

7.5. The flow rate of NH_3 and TMG are kept as 450 and 2.5 sccm, respectively. It is found that the growth at a high temperature leads to long NWs with a low density. In comparison, the NWs grown at low temperatures tend to coalesce, eventually resulting in NWs with a large diameter. This phenomenon can be explained by the enhanced diffusion length of Ga adatoms at a high temperature, suppressing the nucleation of GaN in the region between the NWs [5-7]. The influence of GaN growth condition is summarized in Table 7.3. With different growth conditions, straight GaN NWs can be grown with density up to $3 \times 10^8 \text{ cm}^{-2}$, height up to $1 \mu\text{m}$ and diameter down to 50 nm. As discussed in Chapter 2.3.3, for the self-induced GaN NW growth on Si by MOCVD, currently, only two groups demonstrate some results as shown in Figures 2.15 (c)&(d), where either an in-situ SiN mask or VLS growth with TMG pre-flowing are used, respectively. For the in-situ SiN mask method, the uniformity of the GaN NWs formed is not good and many NWs are inclined. The density of NW is only around $2 \times 10^2 \text{ mm}^{-2}$ and the diameters of NWs are all larger than $1 \mu\text{m}$. For the TMG pre-flowing method, the density of GaN NW is $2.44 \times 10^6 \text{ cm}^{-2}$ and the minimum diameter of NWs is about 350 nm.

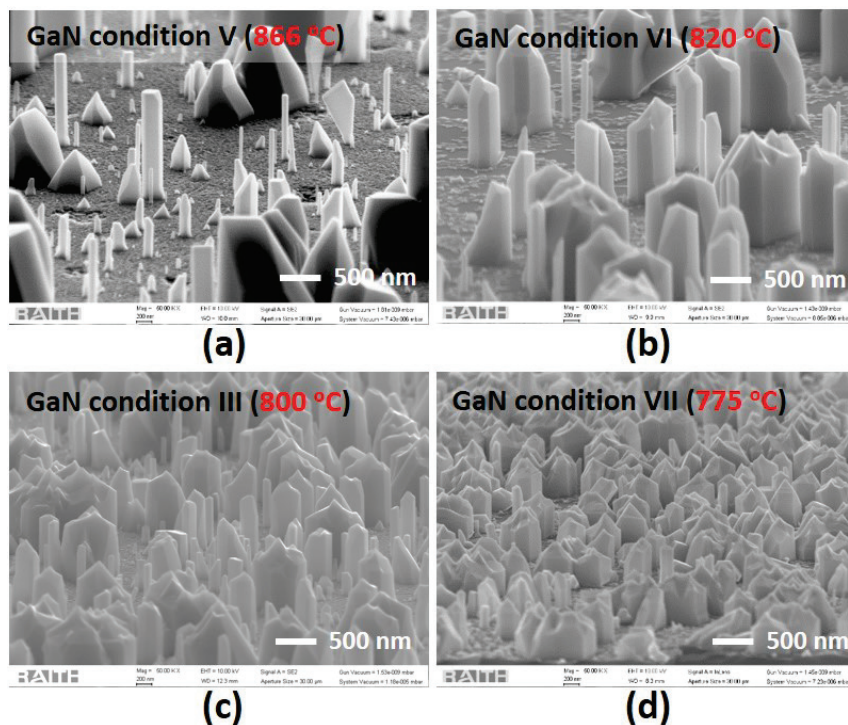


Figure 7.4: Bird's-eye view SEM images of GaN NW growth with GaN condition III and V to VII.

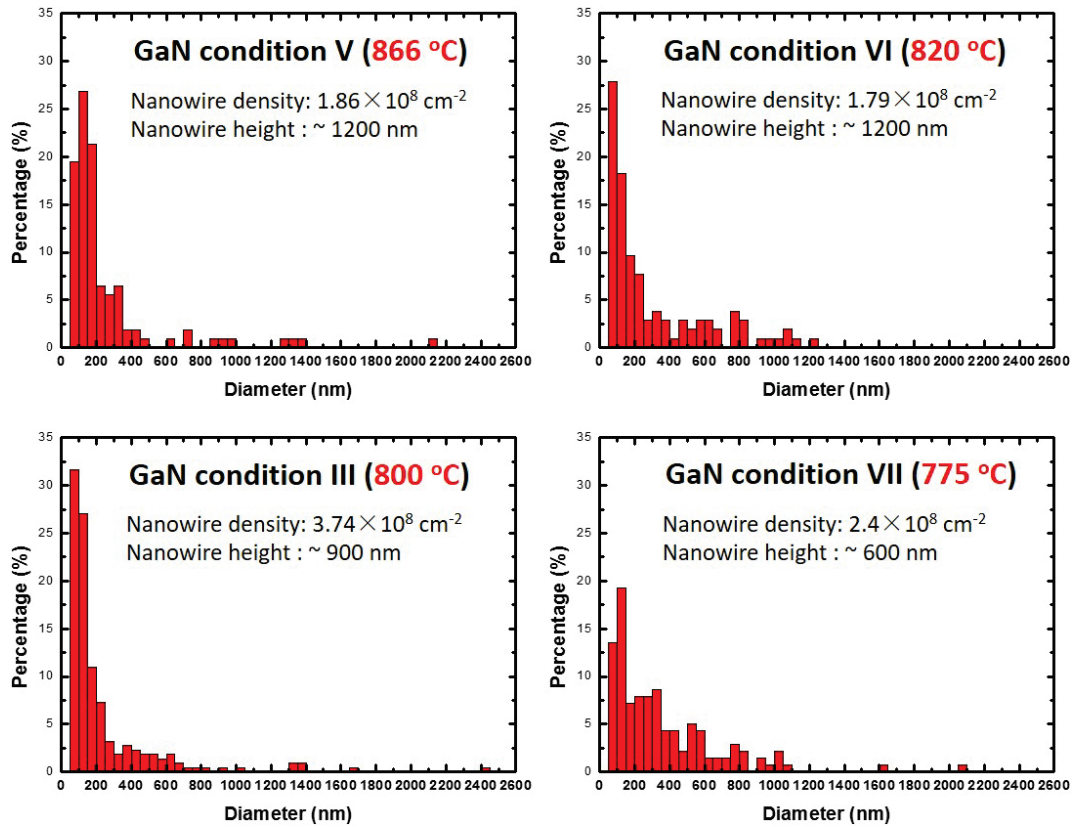


Figure 7.5: Diameter distribution, density and height of GaN NWs grown with GaN condition III and V to VII.

GaN NWs \ GaN growth condition	With increasing NH ₃ flow rate	With increasing TMG flow rate	With increasing Temperature
Diameter	↑	↓, then ↑	↓
Density	↓	↑, then ↓	↓
Height	↓	↓	↑

Table 7.3: A summary of the influences of GaN growth condition on GaN NW morphology. '↑' means an increase, and '↓' means a decrease.

7.3 Structural and Optical Characterization

To determine the crystal orientations of GaN NWs, HR-XRD measurements have been performed. Figure 7.6 demonstrates XRD measurement in a 2θ - ω mode. Only sharp diffraction peaks of (0002) GaN and (111) Si can be observed, indicating single crystal GaN has been obtained.

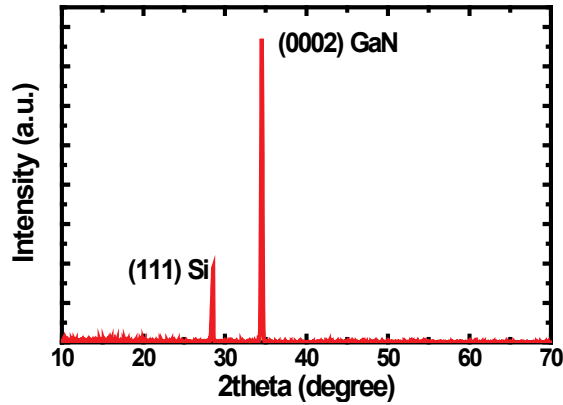


Figure 7.6: XRD 2θ - ω scan profile of the symmetric plane of the GaN NWs grown on (111) Si substrate.

Moreover, the GaN NW in-plane crystal orientation is also investigated by performing XRD measurements in a phi-scan mode on asymmetric GaN (10-12) plane, shown in Figure 7.7. For comparison, the GaN NWs grown by MBE shown in Figure 2.15(e) is also measured. For the GaN NWs grown by MOCVD, six peaks with a 60 degree spacing are clearly seen, which is attributed to the GaN hexagonal symmetric structure [8]. But for the GaN NWs grown by MBE, there is no clear peak, indicating that the in-plane crystal orientations of different GaN NWs are fairly random. This means that there is not any epitaxial crystal relationship between GaN NWs and the (111) Si substrate used. Based on these two XRD data, it can be concluded that all the GaN NWs of our sample align along the c-direction and have the same in-plane crystal orientation.

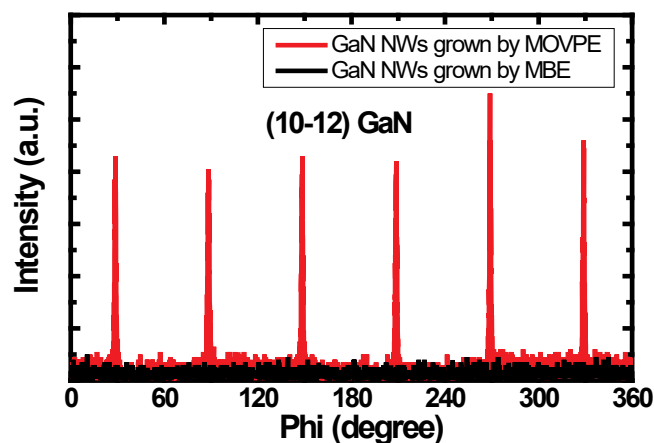


Figure 7.7: XRD phi-scan spectra on the asymmetric (10-12) GaN plane of the GaN NWs grown by MOCVD and MBE, respectively.

The GaN NW crystal quality is investigated by XRD rocking curve scan of (0002) GaN plane, as shown in Figure 7.8. Comparing with GaN NWs grown by MBE, the FWHM of the XRD rocking curve of the NWs grown by MOCVD is much smaller, indicating a good crystal quality. This is also much better than that of the GaN NWs grown on Si by means of in-situ SiN masks, where the FWHM of the XRD rocking curve is 1.37° [9].

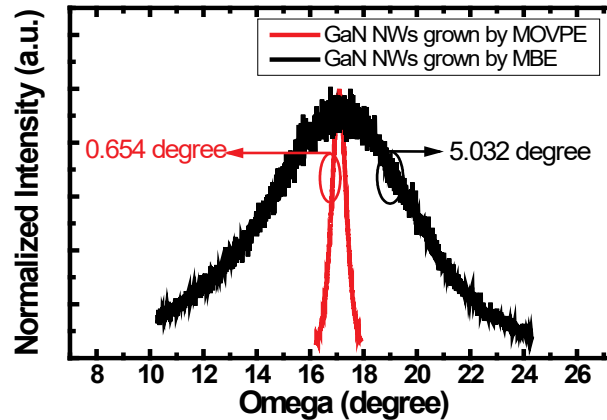


Figure 7.8: XRD ω -rocking curves of GaN (0002) plane of GaN NWs grown by MOCVD and MBE.

Optical properties have been investigated with PL measurements at both room temperature and low temperature (10 K) using a 325 nm He-Cd laser. For a reference, the spectrum of a standard planar 1.2 μm thick c-plane GaN-on-Si by MOCVD is also presented. As shown in Figure 7.9, room temperature PL intensity of NWs is 44 times higher than that of the reference sample, possibly due to a low density of defects. In the spectra at low temperature as shown in Figure 7.10, a blue shift in emission wavelength has been observed compared with that of the planar GaN on Si, suggesting a strain relaxation in the NWs [10].

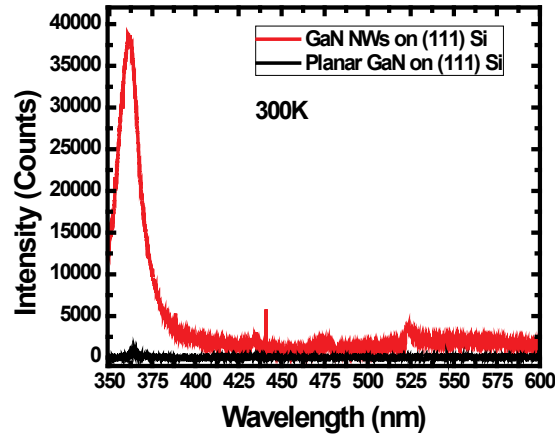


Figure 7.9: PL spectra of the GaN NWs and the planar GaN on (111) Si grown by MOCVD, measured at room temperature.

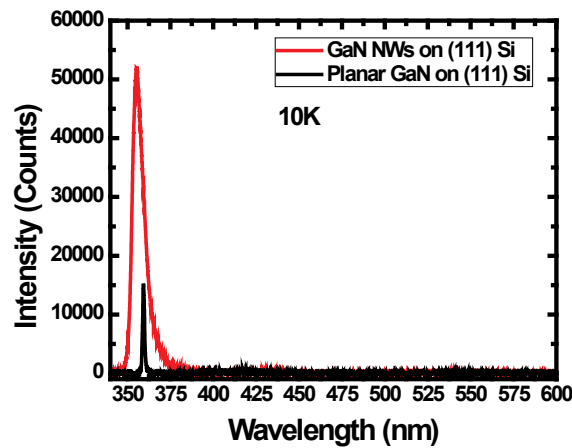


Figure 7.10: PL spectra of the GaN NWs and the planar GaN on (111) Si grown by MOCVD, measured at 10 K.

TEM measurements have been carried out to study the NW crystal structure. Figures 7.11(a) and (b) exhibit typical cross-sectional TEM images of the GaN NWs, taken around [1-100] zone-axis with diffraction vectors of $\mathbf{g}=0002$ and $\mathbf{g}=11-20$, respectively. The gaps between NWs are filled with SiO_2 for sample preparation; while the shadows in some NWs are caused by strain contrast. No dislocations are observed in the upper part of our NWs due to an elastic strain relaxation during growth [11]. This good crystal quality is a good base for future growth of quantum wells/quantum dots. Figure 7.11(c) is a cross sectional TEM image taken with $\mathbf{g}=1-100$ used for the observation of any possible BSFs. No BSFs are observed in the upper part of NWs, agreeing well with the low temperature PL results.

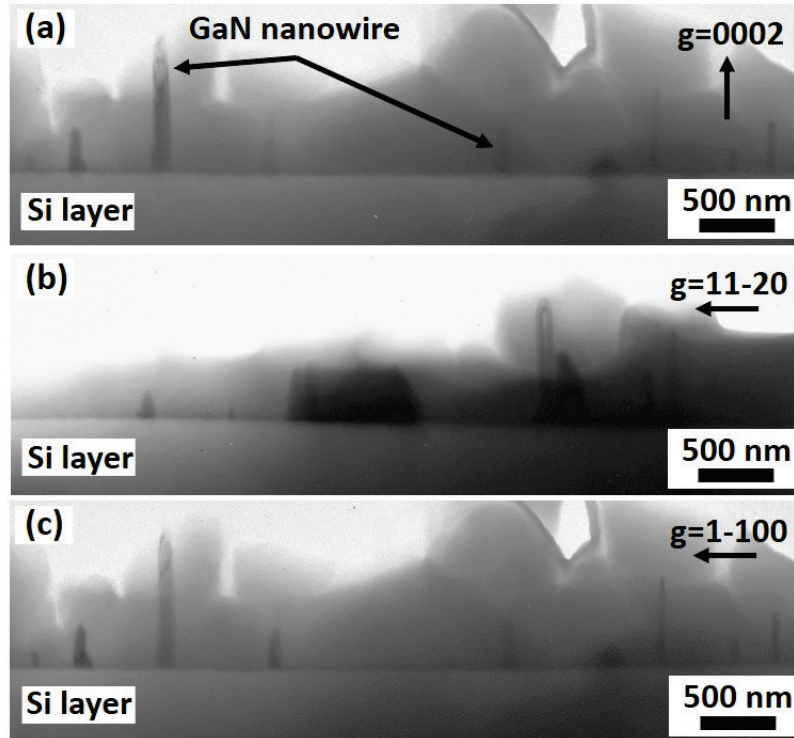


Figure 7.11: Cross sectional TEM images of GaN NWs taken around $[1-100]$ zone-axis with (a) $g = 0002$ and (b) $g = 11-20$, and (c) taken close to $[1-210]$ zone-axis with $g = 10-10$.

7.4 Conclusion

In summary, self-induced GaN NW growth on (111) silicon has been successfully realized by a two-step approach: TMA pre-flowing and then NW growth. It has been revealed that the Al-Si alloys formed by the TMA pre-flowing step is crucial and act as the nucleation sites for the subsequent GaN NW growth. The conditions for the TMA pre-flowing and the GaN NW growth have been optimized by systematically adjusting the temperature and the precursor flow rate, which has been found to have strong influence on the morphology of NWs. Straight NWs grown along the c -direction have been obtained with a density of $1\sim 3 \times 10^8 \text{ cm}^{-2}$. The diameters of NWs are down to 50 nm and the heights of NWs are up to 1.2 μm . In comparison with other reported self-induced GaN NWs on Si by MOCVD, our growth results exhibit straight NWs with a much higher density and smaller diameter. Based on the HD-XRD and TEM characterisations, GaN NWs demonstrate a high crystal quality with a low density of defects. The FWHM of the XRD rocking curve of the NWs are 0.654° , which is much smaller than that of GaN NWs grown by means of in-situ SiN masks (1.37°). The PL spectrum

measured at both a low temperature and room temperature demonstrate excellent optical properties with only a strong band edge emission, further confirming the crystal quality.

References

1. J. Ristić, E. Calleja, M.A. Sánchez-García, J. M. Ulloa, J. Sánchez-Páramo, J. M. Calleja, U. Jahn, A. Trampert, K. H. Ploog, *Phys. Rev. B* **68**, 125305 (2003)
2. C. Chèze, L. Geelhaar, O. Brandt, W. M. Weber, H. Riechert, S. Münch, R. Rothemund, S. Reitzenstein, A. Forchel, T. Kehagias, P. Komninou, *Nano Research* **3**, 528 (2010)
3. R. Navamathavan, Y. H. Ra, K. Y. Song, D. W. Kim, and C. R. Lee, *Curr. Appl. Phys.* **11**, 77 (2011)
4. Y.H. Ra, R. Navamathavan, and C. R. Lee, *CrystEngComm* **14**,8208 (2012)
5. Y. T. Lin, T. W. Yeh, and P. D. Dapkus, *Nanotechnology*, 23, 465601 (2012)
6. X. Wang, S. Li, S. Fündling, H. H. Wehmann, M. Strassburg, H. J. Lugauer, U. Steegmüller, and A. Waag, *J. Phys. D: Appl. Phys.* **46**, 205101 (2013)
7. S. Chae, K. Lee, J. Jang, D. Min, J. Kim, and O. Nam, *J. Cryst. Growth* **409**, 65 (2015)
8. J. Kim, C. Bayram, H. Park, C. W. Cheng, C. Dimitrakopoulos, J. A. Ott, K. B. Reuter, S. W. Bedell, and D. K. Sadana, *Nature communications* **5**, 4836 (2014)
9. D. Salomon, A. Dussaigne, M. Lafossas, C. Durand, C. Bougerol, P. Ferret, J. Eymery, *Nanoscale Res. Lett.* **8**, 61 (2013)
10. L. Lee, K. F. Chien, W. C. Chou, C. H. Ko, C. H. Wu, Y. R. Lin, C. T. Wan, C. H. Wann, C. W. Hsu, Y. F. Chen, and Y. K. Su, *Cryst. Eng. Comm.* 14, 4486 (2012)
11. J. Ristić, E. Calleja, M. A. Sánchez-García, J. M. Ulloa, J. Sánchez-Páramo, J. M. Calleja, U. Jahn, A. Trampert, and K. H. Ploog, *Phys. Rev. B* 68, 125305 (2003)

Chapter 8

Summary and Future Work

8.1 Summary

The research objectives in this thesis are to grow high quality semi-polar GaN and GaN NWs on Si substrates.

In order to realise semi-polar GaN growth on Si, two simple but cost-effective approaches have been developed for Si substrate patterning. By employing standard photolithography, dry etching, anisotropic wet etching and selective deposition, 2-inch patterned Si substrates with either inverted-pyramids or stripes have been achieved. Both patterned Si substrates demonstrate good uniformity and high reproducibility.

Semi-polar (11-22) GaN growth has been performed on the patterned Si substrates with inverted-pyramids. By optimising growth conditions, semi-polar (11-22) GaN film (with 3 μm thickness) with a smooth surface has been achieved. The melt-back etching, one of the great issues for GaN grown on Si, has been successfully prevented by a selective deposition of SiO_2 before growth. Moreover, surface cracking, another great challenge for GaN growth on silicon, has also been resolved. The obtained (11-22) GaN shows excellent crystal quality with a single crystal orientation, as revealed from HD-XRD and TEM measurements. Based on TEM results, a clear reduction in both dislocation density and BSF density has been observed and the corresponding mechanisms have been studied. In addition, good optical properties have also been demonstrated by PL measurements. Low temperature PL measurement show a significant high ratio of the intensity of the near band emission to the BSF related emission, which further confirms a significantly reduced BSF density.

Based on the patterned Si substrates with stripes, semi-polar (20-21) GaN growth has been realised. By varying growth conditions and patterned Si substrate parameters, GaN has been grown on either single or both sidewalls of Si stripe, leading to almost coalesced film or 'M' shape GaN stripes, respectively. The melt-back etching issue has been resolved by introducing a big gap truncating Si stripes. The GaN obtained on both patterned Si substrates show good

crystal quality, as demonstrated by HD-XRD scans and further confirmed by PL measurement. The FWHM of the XRD on-axis rocking curve of the GaN (20-21) obtained is down to 0.14° , which is much better than any other reports with a similar growth thickness. Low temperature PL measurement show a significant high ratio of the intensity of the near band emission to the BSF related emission, indicating a quite low BSF density. The crystal defect reductions have been observed and studied by TEM measurements. Moreover, InGaN QWs have been grown on the top of the (20-21) GaN stripes. Comparing with the MQWs grown on c-plane GaN, a significant reduction in QCSE has been achieved, as revealed by power dependent PL measurements.

Finally, GaN NWs have been successfully achieved on Si without any alien metal catalyst or patterned mask, by employing the TMA pre-flowing. The influences of TMA pre-flowing and GaN growth conditions have been systematically investigated, resulting in GaN NWs with a density of $1\sim 3\times 10^8\text{ cm}^{-2}$, a 50~1000 nm diameter and a height of up to 1 μm . Neither dislocations or BSFs have been observed on the top of NWs in TEM measurements. Based on XRD and PL, it has been demonstrated that the GaN NWs exhibit a single crystal orientation and high crystal quality.

8.2 Future Work

Based on the semi-polar (11-22) GaN film on patterned Si, LED structures, especially with green and yellow emission, may be grown, taking advantages of semi-polar orientations.

The stripe patterned Si substrate may be optimized for the growth of fully coalesced semi-polar (20-21) GaN, which is advantageous for homogeneous InGaN MQWs with high In incorporation. A green or yellow LD structure on the top of semi-polar (20-21) GaN is also planned. For the 'M' shape GaN stripes, by employing very smooth sidewalls as the good cavities, LD structures are also planned. The LD fabrication will benefit from the easy cleavage of Si substrates.

For the GaN NW growth on Si, due to low density crystal defects and relaxed strain for the top of NWs, MQWs or quantum dots can be further grown on the top of GaN NWs, aiming to achieve nano-devices with excellent optical properties and significantly reduced QCSE.

Abbreviations

AFM	atomic force microscope	NH₃	ammonia
AlN	aluminium nitride	NW	nanowire
BSF	basal plane stacking fault	PECVD	plasma enhanced chemical vapour deposition
CP₂Mg	bis(cyclopentadienyl)magnesium	PL	photoluminescence
ELOG	epitaxial lateral overgrowth	PSF	prismatic stacking fault
EQE	external quantum efficiency	QCSE	quantum confine stark effect
FWHM	full width half maximum	MQW	multiple quantum well
GaN	gallium nitride	RIE	reactive-ion etching
H₂	hydrogen	Sccm	standard cubic millimetres per minute
HD-XRD	high resolution X-ray diffraction	SEM	scanning electron microscopy
HVPE	hydride vapour phase epitaxy	SF	stacking fault
ICP	inductively coupled plasma	Si	silicon
InN	indium nitride	Si₂H₆	disilene
IPA	isopropyl alcohol	SiC	silicon carbide
IQE	internal quantum efficiency	TEM	transmission electron microscope
LD	laser diode	TMA	trimethylaluminium
LED	light-emitting diode	TMG	trimethylgallium
LT	low temperature	TMI	trimethylindium
MBE	molecular beam epitaxy	UV	ultra-violet
Mg	Magnesium	VLS	vapor-liquid–solid
MOCVD	metal organic chemical vapour deposition		